

FINAL REPORT ADDENDUM

Perchlorate Destruction and Potable Water Production
Using Membrane Biofilm Reduction
and Membrane Filtration

ESTCP Project ER-200541

September 2013

Patrick Evans
Jennifer Smith
Clyde Arucan
Daniel Berokoff
CDM Smith

David Friese
Ryan Overstreet
Renato Vigo
APTwater

Bruce Rittman
Aura Ontiveros-Valencia
He-Ping Zhao
Youneng Tang
Bi-O Kim
Steven Van Ginkel
Rosa Krajmalnik-Brown
Arizona State University

This document has been cleared for public release



REPORT DOCUMENTATION PAGE*Form Approved
OMB No. 0704-0188*

The public reporting burden for this collection of information is estimated to average 1 hour per response, including the time for reviewing instructions, searching existing data sources, gathering and maintaining the data needed, and completing and reviewing the collection of information. Send comments regarding this burden estimate or any other aspect of this collection of information, including suggestions for reducing the burden, to the Department of Defense, Executive Services and Communications Directorate (0704-0188). Respondents should be aware that notwithstanding any other provision of law, no person shall be subject to any penalty for failing to comply with a collection of information if it does not display a currently valid OMB control number.

PLEASE DO NOT RETURN YOUR FORM TO THE ABOVE ORGANIZATION.

1. REPORT DATE (DD-MM-YYYY)		2. REPORT TYPE		3. DATES COVERED (From - To)	
4. TITLE AND SUBTITLE				5a. CONTRACT NUMBER	
				5b. GRANT NUMBER	
				5c. PROGRAM ELEMENT NUMBER	
6. AUTHOR(S)				5d. PROJECT NUMBER	
				5e. TASK NUMBER	
				5f. WORK UNIT NUMBER	
7. PERFORMING ORGANIZATION NAME(S) AND ADDRESS(ES)				8. PERFORMING ORGANIZATION REPORT NUMBER	
9. SPONSORING/MONITORING AGENCY NAME(S) AND ADDRESS(ES)				10. SPONSOR/MONITOR'S ACRONYM(S)	
				11. SPONSOR/MONITOR'S REPORT NUMBER(S)	
12. DISTRIBUTION/AVAILABILITY STATEMENT					
13. SUPPLEMENTARY NOTES					
14. ABSTRACT					
15. SUBJECT TERMS					
16. SECURITY CLASSIFICATION OF:			17. LIMITATION OF ABSTRACT	18. NUMBER OF PAGES	19a. NAME OF RESPONSIBLE PERSON
a. REPORT	b. ABSTRACT	c. THIS PAGE			19b. TELEPHONE NUMBER (Include area code)

Table of Contents

EXECUTIVE SUMMARY	ii
Introduction and Organization	1
Chapter 1. Chemical Fluxes from Rialto Data.....	3
1.1 Operational conditions at the Time of Biomass Sampling.	3
1.2 Fluxes	3
Chapter 2. Community Function and Structure	8
Chapter 3. Solids and EPS in the Biofilm.....	16
3.1 Solids analysis.....	16
3.2 EPS analysis.....	17
Chapter 4. Microscopic Analysis on Distribution of Live and Dead Portions within the Biofilm.....	19
Chapter 5. Synthesis for the Side-Reactors and Reactor Modules in the MBfR Vessels	25
6.1 Permeation Rates for Hydrogen Gas Through MBfR Fibers.....	28
6.2 Ecological Interactions Between DB and SRB in the MBfR Biofilm	30
6.3 Phylogenetic analysis of DB and SRB in hydrogen-fed biofilms.....	34
6.4 Interactions Between DB and PRB in a H ₂ -Based Biofilm	37
6.5 Competition Among Perchlorate, Nitrate, and Sulfate Reductions	39
6.6 Two-Stage MBfR to Achieve Full Perchlorate Reduction with Rialto's Groundwater.....	43
Chapter 7. Exploring Mechanisms and Performance with Mechanistic Modeling	47
7.1 Developing the Multi-Species Model for a H ₂ -Based Biofilm Able to Do NO ₃ ⁻ and ClO ₄ ⁻ Reductions	47
7.2 Application of the NO ₃ ⁻ and ClO ₄ ⁻ Model to MBfR Performance.....	50
7.3 A Model for NO ₃ ⁻ and SO ₄ ²⁻ Reductions in the MBfR Biofilm	53
Chapter 8. Special Modeling Evaluation of the Pilot MBfRs.....	57
Chapter 9. Global Synthesis.....	62
Chapter 10. References	65

EXECUTIVE SUMMARY

Background

This report summarizes the findings of research carried out at Arizona State University (ASU) in parallel with a field pilot study led by CDM Smith in cooperation with APTwater and reported in its own final report. The objective of the overall project was biological treatment of a groundwater contaminated with two oxidized contaminants: nitrate (NO_3^-) and perchlorate (ClO_4^-). Dissolved oxygen (O_2) and sulfate (SO_4^{2-}) are oxidized compounds that also were present. The treatment goal was to use the H_2 -based Membrane Biofilm Reactor (MBfR) to achieve microbial reduction of NO_3^- and ClO_4^- into innocuous substances (N_2 , H_2O , and Cl^-), while not promoting SO_4^{2-} reduction to sulfide.

The MBfR promotes the growth of autotrophic bacteria capable of using hydrogen gas (H_2) as their electron donor by its diffusion through bubbleless gas-transfer membranes. A microbial community develops as a biofilm attached to the membrane's outer surface; the biofilm normally is comprised of a diverse spectrum of autotrophic and heterotrophic microorganisms embedded in a matrix composed of extracellular polymeric substances (EPS). "Side-reactors" were established as part of the pilot MBfRs to study the biofilm and its microbial community structure. The ASU team carried out in-depth analyses of the biofilms from the side-reactors, as well as from two pilot modules. These analyses included microbial ecology, microscopy, and chemical analyses.

The ASU team also carried out a series of experiments with bench-scale MBfR and developed mechanistic mathematical models of the biofilms. The goal of these studies was to gain fundamental understanding of the kinetic, transport, and ecological mechanisms controlling the performance of the pilot MBfRs. Thus, the over-arching goal of the ASU research was to provide a fundamental, mechanistic foundation for understanding the results obtained in the pilot study and for identifying strategies to improve performance for future applications.

The report is divided into nine chapters plus the cited references. The first five chapters address ASU's analyses for the pilot MBfRs. Chapters 6 to 8 report on the bench-scale and modeling research. Chapter 9 then gives a global synthesis of all of the results. Much of the work reported here has been published in peer-review journals, and these primary sources are identified throughout the report.

Performance and characteristics of the biofilms from the pilot MBfRs

The field pilot study showed that, although the two-stage MBfR system was effective for reducing NO_3^- and ClO_4^- , it did not achieve one of the goals: an effluent ClO_4^- concentration less than $6 \mu\text{g/L}$. Attempts to reduce the loading rates of the electron acceptors by lowering the flow rate did not lead to the desired outcome of $\text{ClO}_4^- < 6 \mu\text{g/L}$ for sustained operation, but led to SO_4^{2-} reduction, an undesired outcome. Regularly switching the lead and lag positions also did not bring about the desired result. The ASU Team focused on uncovering why the two-stage MBfR system did not achieve the $6\text{-}\mu\text{g/L}$ goal, even though it performed well in other ways. The ASU team performed chemical, ecological, and kinetic evaluations to gain comprehensive insight into MBfR performance.

The biofilms in the side reactors and the reactor modules in the MBfR vessels had consistent characteristics that reflect the operating conditions at the pilot site. While the biofilm thickness varied, it typically was about 200 μm . The biofilm was only about 10% inorganic, which means that precipitation was prevented well by the pH-control system. Although the biofilm contained 40 – 50% extracellular polymeric substances (EPS), the cells were predominantly live, particularly near the membrane substratum. For all MBfRs, perchlorate-reducing bacteria (PRB) always made up the smallest fraction of the active bacteria, sulfate-reducing bacteria (SRB) always were present, and SRB became more important when SO_4^{2-} reduction was the a major sink for H_2 .

Analysis of the fluxes of the four electron acceptors (i.e., ClO_4^- , NO_3^- , O_2 , and SO_4^{2-}) showed that H_2 availability and acceptor fluxes determined the degree of success with ClO_4^- removal and minimizing SO_4^{2-} reduction. The lead MBfR was responsible of reducing 70-90% of the NO_3^- loading and > 99% of the O_2 loading. A $\text{NO}_3^- + \text{O}_2$ surface loading of $\geq 0.3 \text{ g H}_2/\text{m}^2\text{-day}$ suppressed SO_4^{2-} reduction in the lead MBfR. With most NO_3^- and all O_2 removed by the lead MBfR, the low surface loading of NO_3^- and O_2 influent to the lag MBfR allowed the onset of SO_4^{2-} reduction in the lag MBfR. Quantitatively, a NO_3^- flux $< \sim 0.1 \text{ g H}_2/\text{m}^2\text{-day}$ allowed SO_4^{2-} reduction in the lag MBfR when H_2 delivery was not limiting. (In order to compare all fluxes, they are expressed as H_2 consumption flux in $\text{g H}_2/\text{m}^2\text{-day}$.)

ClO_4^- respiration occurred in the lead and lag MBfRs, but the highest ClO_4^- reduction occurred at the lag MBfR, where competition from NO_3^- and O_2 respirations was minimized. However, ClO_4^- reduction flux in the lag MBfR was inversely correlated to the SO_4^{2-} flux. A SO_4^{2-} flux of $0.003 \text{ g H}_2/\text{m}^2\text{-day}$ or more seemed to slow ClO_4^- reduction. A SO_4^{2-} flux of $0.001 \text{ g H}_2/\text{m}^2\text{-day}$ allowed the highest ClO_4^- flux.

Operational conditions applied to the pilot MBfRs affected the microbial communities in ways that corresponded to acceptor fluxes. When acceptor surface loadings were high due to a high flow rate, the pilot MBfRs (especially the lead MBfR) experienced a limitation of H_2 delivery, and DB were dominant. Increasing the HRT, which decreased the surface loading for all acceptors, eliminated H_2 limitation, but at the expense of favoring SRB, whose metabolic versatility helped them remain in the biofilm regardless of SO_4^{2-} reduction activity.

Bench-scale experiments and modeling

The ASU team carried out a series of bench-scale experiments designed to elucidate critical kinetic and ecological mechanisms that control the performance of the MBfR when ClO_4^- reduction to $\mu\text{g/L}$ concentrations is the goal. Of over-arching importance is that multiple electron acceptors were present in the influent water: O_2 , NO_3^- , SO_4^{2-} , and ClO_4^- . Typically and in the case of the field study, ClO_4^- is present at by far the lowest concentration. This means that PRB must compete for the common electron donor (H_2) and space in the biofilm with bacteria that reduce the other acceptors. The competition can be an important factor controlling whether or not the PRB are able to reduce ClO_4^- to very low concentrations.

In a series of experimental studies, the ASU team evaluated competition for H₂ and space among PRB, DB, and SRB. Three of the studies focused specifically on the ability to reduce ClO₄⁻ to μg/L concentrations, while three others provided foundation information needed to interpret the studies about ClO₄⁻ reduction.

In parallel to the bench-scale experiments, the ASU team developed and applied a series of mechanistic mathematical models. The primary objective of the mathematical modeling was to integrate and quantify the many ecological, kinetic, and transport mechanisms occurring when H₂ is delivered to a biofilm of bacteria exposed to multiple electron acceptors. Two models addressed different combinations of electron acceptors, but with a common framework. One model described NO₃⁻ and ClO₄⁻ reductions occurring in a H₂-based biofilm. The second model represented NO₃⁻ and SO₄²⁻ reductions.

Bench-scale experiments were able to achieve < 6 μgClO₄⁻/L under proper conditions, and modeling results provided mechanistic understanding about how the fluxes of NO₃⁻, O₂, and SO₄²⁻ need to be managed to allow for complete ClO₄⁻ reduction. Taken together, the bench-scale and modeling results, which are consistent with pilot results, lead to the follow guidance on managing electron-acceptor surface loadings.

First, a moderate flux of NO₃⁻ + O₂ is a key to helping promote PRB and ClO₄⁻ reduction by giving the PRB three electron acceptors (ClO₄⁻, NO₃⁻, and O₂) without causing too much competition for H₂ and space. A NO₃⁻ + O₂ flux of ≤ ~0.21 g H₂/m²-day promotes ClO₄⁻ reduction, while a flux ≥ ~0.36 g H₂/m²-day begins to cause serious inhibition to ClO₄⁻ reduction. For comparison, the pilot MBfRs gave the highest ClO₄⁻ flux in the lag MBfR when the NO₃⁻ + O₂ flux was ~ 0.17 g H₂/m²-day.

Second, the NO₃⁻ + O₂ flux should be held in a moderate range to suppress SO₄²⁻ reduction. A target flux for NO₃⁻ + O₂ is ~ 0.3 g H₂/m²-day. For comparison, NO₃⁻ + O₂ fluxes > 0.3 g H₂/m²-day stopped SO₄²⁻ reduction in the pilot lead MBfR, but lower NO₃⁻ + O₂ fluxes allowed SO₄²⁻ reduction in the lag MBfR.

Interpreting the pilot results in light of modeling and bench-scale results

Factors specific to the operation of the pilot MBfRs affected performance for ClO₄⁻ reduction. The ASU team performed special modeling runs to gain insight into the observed performance and to define possibilities for achieving better performance in the future. The team also made direct comparisons with the bench-scale experiments.

Modeling the pilot conditions suggested that external mass-transport resistance may have been greater in the pilot MBfRs than in the bench-scale MBfRs. This interpretation was supported by the observation that a large amount of biomass accumulated between the spacers in the side reactors. The special modeling runs also point to the possibility that the pilot biofilms selected for different and less-efficient PRB.

A difference between the pilot and bench-scale MBfRs is that the influent of the lag MBfRs was oxygenated for the bench-scale experiments, but not for the pilot. Oxygenation

made it possible to control the $\text{NO}_3^- + \text{O}_2$ surface loading to the lag MBfR, keeping it in the optimal range even though most of the NO_3^- was removed in the lead MBfR. Inter-stage oxygenation is a good option to build into MBfR systems designed for reducing ClO_4^- and NO_3^- .

Another difference is that the lead and lag MBfRs were switched regularly in the field pilot, while they were maintained as lead or lag for the bench-scale studies and special modeling analysis. The switching definitely caused the biofilm communities to be similar between lead and lag MBfRs, although they were distinct in the bench-scale MBfRs. Switching also may have played a role in accentuating accumulation of SRB by making the biofilm thicker in the lag MBfR.

In summary, the modeling and bench-scale results show no intrinsic roadblock for achieving a very low ClO_4^- concentration when the influent water contains much higher concentrations of NO_3^- , O_2 , and SO_4^{2-} . One clear key is managing the $\text{NO}_3^- + \text{O}_2$ loading so that it promotes PRB while simultaneously suppressing SO_4^{2-} reduction. The two-stage strategy is well tuned for this goal, and particular attention has to be paid to the $\text{NO}_3^- + \text{O}_2$ loading to the lag MBfR.

Introduction and Organization

This report summarizes the findings of research carried out at Arizona State University (ASU) in parallel with a field pilot study led by CDM Smith in cooperation with APTwater. All of the results of the pilot study are reported in a separate final report (Evans et al., 2013). The objective of the overall project was biological treatment of a groundwater contaminated with two oxidized contaminants: nitrate (NO_3^-) and perchlorate (ClO_4^-). Dissolved oxygen (O_2) and sulfate (SO_4^{2-}) are oxidized compounds also present. Table 1 synthesizes the concentrations of these compounds in the groundwater from West Valley Water District Well 22 in Rialto, CA. The treatment goal was to use the H_2 -based Membrane Biofilm Reactor (MBfR) to achieve microbial reduction of NO_3^- and ClO_4^- into innocuous substances (N_2 , H_2O , and Cl^-) (Rittmann 2007), while not promoting SO_4^{2-} reduction to sulfide.

The MBfR promotes the growth of autotrophic bacteria capable of using hydrogen gas (H_2) as their electron donor by its diffusion through bubbleless gas-transfer membranes. A microbial community develops as a biofilm attached to the membrane's outer surface; the biofilm normally is comprised of a diverse spectrum of autotrophic and heterotrophic microorganisms embedded in a matrix composed of extracellular polymeric substances (EPS).

Table 1. Concentrations of oxidized compounds in the groundwater treated at Rialto, CA

Electron Acceptor	Concentration
Nitrate, NO_3^-	8-9 mg N/L
Perchlorate, ClO_4^-	160-200 $\mu\text{g/L}$
Oxygen, O_2	~9 mg/L
TCE, C_2HCl_3	50-60 $\mu\text{g/L}$
Sulfate, SO_4^{2-}	20-22 mg/L

Figure 1a shows one of the “side-reactors” that were established as part of the pilot MBfRs to study the biofilm and its microbial community structure. Figure 1b shows biofilm development on the fiber sheet of side reactors. The side-reactors were removed and shipped to ASU at the end of each phase (i.e., start-up, optimization, and challenge) of testing at Rialto, CA (Evans et al., 2013). While CDM Smith and APTwater focused on the operational conditions for the pilot MBfR vessels, ASU was in charge of elaborating in-depth analyses of the side-reactors established at Rialto, CA. During operation of the pilot MBfR vessels, some pilot-reactor modules were taken down due to leaking problems. These broken reactor modules also were sent to ASU to perform the same analysis done to the side-reactors.



Figure 1a Side reactor shipped to ASU. **1b** Biomass development on the surface of fibers in the side reactor.

The ASU report summarizes the findings of the molecular, microscopy, and chemical analysis that the ASU team carried out with biofilm samples from the side-reactors, as well as from membranes removed from broken reactor modules in the MBfR vessels. The report also summarizes our results from bench-scale MBfRs operated at ASU and mathematical modeling to help us understand the microbial community function and structure during nitrate, perchlorate, and sulfate reductions. The over-arching goal of the ASU research was to provide a fundamental, mechanistic foundation for understanding the results obtained in the pilot study and for extrapolating the pilot finding to improve performance for future application.

We divide this report into ten chapters, of which the first five address our analyses for the Rialto pilot MBfRs:

1. Chemical fluxes from Rialto pilot data
2. Community function and structure
3. Solids and EPS in the biofilm
4. Microscopic analysis on distribution of live and dead portions within the biofilm
5. Synthesis for the side-reactors and reactor modules in the MBfR vessels.
6. Exploring mechanisms and performance with bench-scale experiments
7. Exploring mechanisms and performance with mechanistic modeling
8. Special modeling of the pilot MBfRs
9. Global synthesis
10. References

Materials, methods, results, and interpretations are provided in each of Chapters 1 through 8, and Chapter 9 synthesizes all of the results in a way that interprets them in the context of the pilot experiments.

Chapter 1. Chemical Fluxes from Rialto Data

1.1 Operational conditions at the Time of Biomass Sampling.

Experimental results from the pilot reactors (e.g., influent and effluent concentrations) used for the ASU analyses were presented in detail in the ESTCP Demonstration Final Report (Evans et al., 2013). We selected six time points to establish the ClO_4^- , NO_3^- , SO_4^{2-} , and O_2 concentrations and removal fluxes; they correspond to the sampling dates for reactor modules and side-reactors sent to ASU from Rialto. Table 2 summarizes the shipment numbers, phases, and other operating conditions. Cells shaded in blue correspond to the shipments from module reactors, while cells shaded in red correspond to the shipments of side-reactors. Flow rates were provided to ASU by APTwater, and we assumed that they were constant leading up to the sampling times. For shipment 5, we received two sets of side-reactors, which are named 5 and 5*.

Table 2. Synthesis of the field-MBfR operational conditions at the time of the module shipments

Shipment	Phase	Shipment date	H ₂ pressure (psig)		Flow rate (GPM)	
			Lead	Lag	Lead	Lag
1	Start up	6/20/2011	17.1	11.4	12	12
2	Start up	8/15/2011	26.6	19.0	18	18
3	Optimization	10/3/2011	14.3	12.4	10	10
4	Optimization	11/28/2011	17.1	14.3	8	8
5 5*	Challenge	1/9/2012	15.6	8.6	6	6
6	Challenge	1/9/2012	15.6	8.6	6	6

Red corresponds to side reactors, and blue corresponds to field modules.

1.2 Fluxes

We use fluxes of ClO_4^- , NO_3^- , SO_4^{2-} , and O_2 as performance metrics. Flux is defined as the mass of electron acceptor reduced per unit membrane surface area per unit time. For interpreting the results with the side-reactors, all chemical concentrations were from the two MBfR vessels (lead/lag configuration). We made two important assumptions when linking the field results to the results with the side-reactors:

- The operational conditions (H_2 pressure and temperature) and chemical concentrations were the same for the side-reactors and reactor modules in the MBfR vessels.
- Biofilms developed in side-reactors were representative for biofilms in the reactor modules in the MBfR vessels.

The calculations of ClO_4^- , NO_3^- , SO_4^{2-} , and O_2 fluxes were based on these conditions:

- All fluxes were calculated individually for lead and lag MBfRs as $J = Q(S_{\text{in}} - S_{\text{eff}})/A$, in which J = the substrate flux ($\text{g substrate/m}^2\text{-d}$), Q = the influent flow rate to the MBfR pilot module (m^3/d), S_{in} = influent concentration (g/m^3), S_{eff} = effluent concentration (g/m^3), and A = the biofilm surface area (m^2).

- b. For the surface area of the field MBfRs, we considered 4 modules per MBfR vessel. Total fiber surface area of field MBfR was then 576 m^2 (4 field modules = $144 \text{ m}^2 \times 4$).
- c. The flux for each substrate was converted to a H_2 flux ($\text{g H}_2/\text{m}^2\text{-day}$) using the stoichiometry in Zhao et al. (2011) and Ontiveros-Valencia et al. (2012).
- d. The effluent from a lead MBfR was the influent to its lag MBfR.
- e. Because sulfide concentrations always were zero in the lead reactor and were detected only from the lag MBfR, we assumed SO_4^{2-} was reduced only in the lag MBfR.
- f. The lead and lag MBfRs switched positions every three days.

We present in Figure 2a a general overview of the consumption of H_2 by each electron acceptor and a comparison of the experimental H_2 fluxes (calculated by the method of Ontiveros-Valencia et al. (2012)) with the maximum-possible H_2 flux as calculated by Tang et al. (2012) for the polypropylene fibers and the operating H_2 pressures. The comparison between the experimental and maximum-possible H_2 flux points out that H_2 delivery was sufficient at the time of shipments 1, 3, 4, 5, and 6 (a difference of at least $0.19 \text{ g H}_2/\text{m}^2\text{-d}$). However, the difference between experimental and maximum H_2 fluxes was small for shipment 2 ($0.03 \text{ g H}_2/\text{m}^2\text{-d}$), which suggests that H_2 limitation was possible at the time of shipment 2, particularly for the lead MBfR. To complement the picture, Figure 2b shows the H_2 pressures and influent flow rates applied over the course of time (corresponding to the different shipments to ASU) to the pilot MBfRs. Particularly important is the reduction of flow rate right after shipment 2 (August 15, 2011), which eliminated any limitation from H_2 delivery, as shown in Figure 2a.

The major sink for electrons was denitrification, followed by O_2 , SO_4^{2-} , and ClO_4^- reductions. The fluxes for SO_4^{2-} and ClO_4^- were significantly smaller than the fluxes for NO_3^- and O_2 , and they cannot be distinguished in Figure 1. Therefore, we plot the ClO_4^- and SO_4^{2-} fluxes separately in Figure 3a.

The lead MBfRs were responsible for ~99% of the O_2 respiration, 70-90% of the denitrification, and a small loss of ClO_4^- . In the lead MBfR, the $\text{NO}_3^- + \text{O}_2$ flux was greater than $\sim 0.3 \text{ g H}_2/\text{m}^2\text{-day}$, and SO_4^{2-} reduction was completely suppressed. The excellent removals of NO_3^- and O_2 in the lead MBfR created a scenario in which NO_3^- (with an average of 2.4 mg N/L) and SO_4^{2-} (average concentration of $\sim 20 \text{ mg/L}$) were the dominant electron acceptors entering the lag MBfR, but with a total acceptor loading much less than for the lead MBfR. This allowed greater ClO_4^- reduction in the lag MBfR (Figure 3b), the desired outcome, due to reduced competition for H_2 and space in the biofilm. For the same reason, it also favored SO_4^{2-} reduction, an undesired outcome. Comparing Figures 2 and 3 shows that the SO_4^{2-} flux (in the lag MBfR) was inversely proportional to the $\text{NO}_3^- + \text{O}_2$ flux. Specifically, the lag MBfR had significant SO_4^{2-} reduction, particularly for shipments 4-6, when the total electron acceptor loading was $< 0.1 \text{ g H}_2/\text{m}^2\text{-day}$.

For the lag MBfR, the ClO_4^- and SO_4^{2-} fluxes were linked to the ClO_4^- and SO_4^{2-} loadings, which co-varied with the flow rate (Figure 2a). However, the ClO_4^- flux was higher when the SO_4^{2-} flux was low. At the time of the second sample (20 days from the end of the start up phase), the ClO_4^- flux in the lag MBfR increased from $0.0006 \text{ g H}_2/\text{m}^2 \text{ day}$ (1st shipment) to $0.0019 \text{ g H}_2/\text{m}^2 \text{ day}$, while the SO_4^{2-} flux was reduced from $0.003 \text{ g H}_2/\text{m}^2 \text{ day}$ to $0.001 \text{ g H}_2/\text{m}^2 \text{ day}$. Shipment 2 was the only point at which the ClO_4^- flux exceeded the SO_4^{2-} flux, and that

was the time when H₂ delivery was limiting. Around the second shipment, the influent flow rate to the MBfR system was 18 gpm (Figure 2b), which was the highest value throughout the operational period. Therefore, a relatively high surface loading of all electron acceptors, combined with some H₂-delivery limitation, seems to have caused decreased SO₄²⁻ reductions and increased ClO₄⁻ removal for the time of the second shipment.

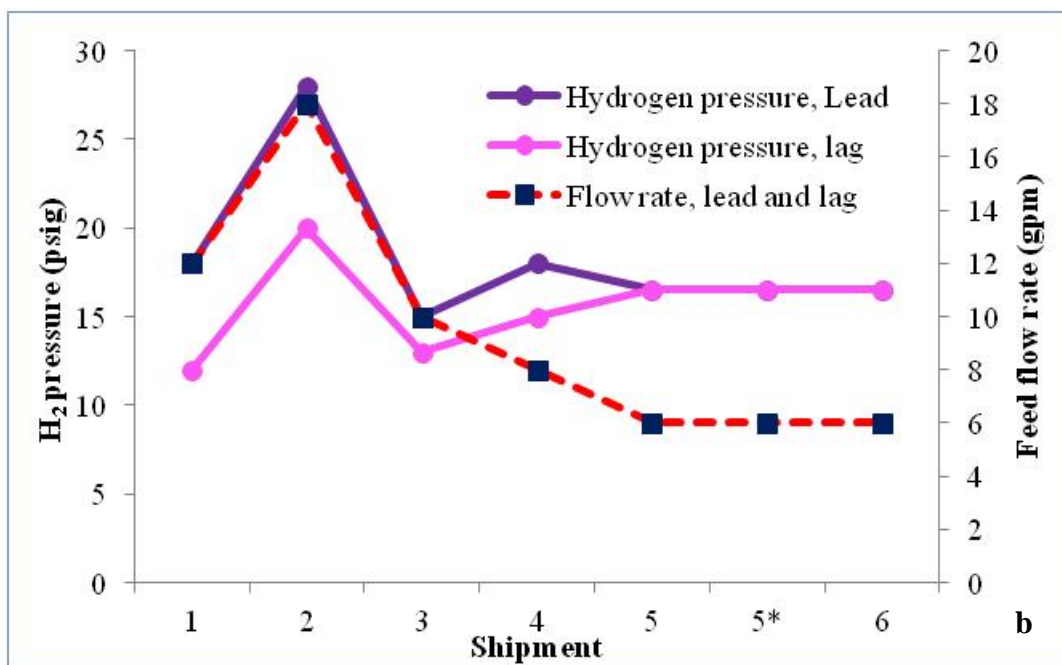
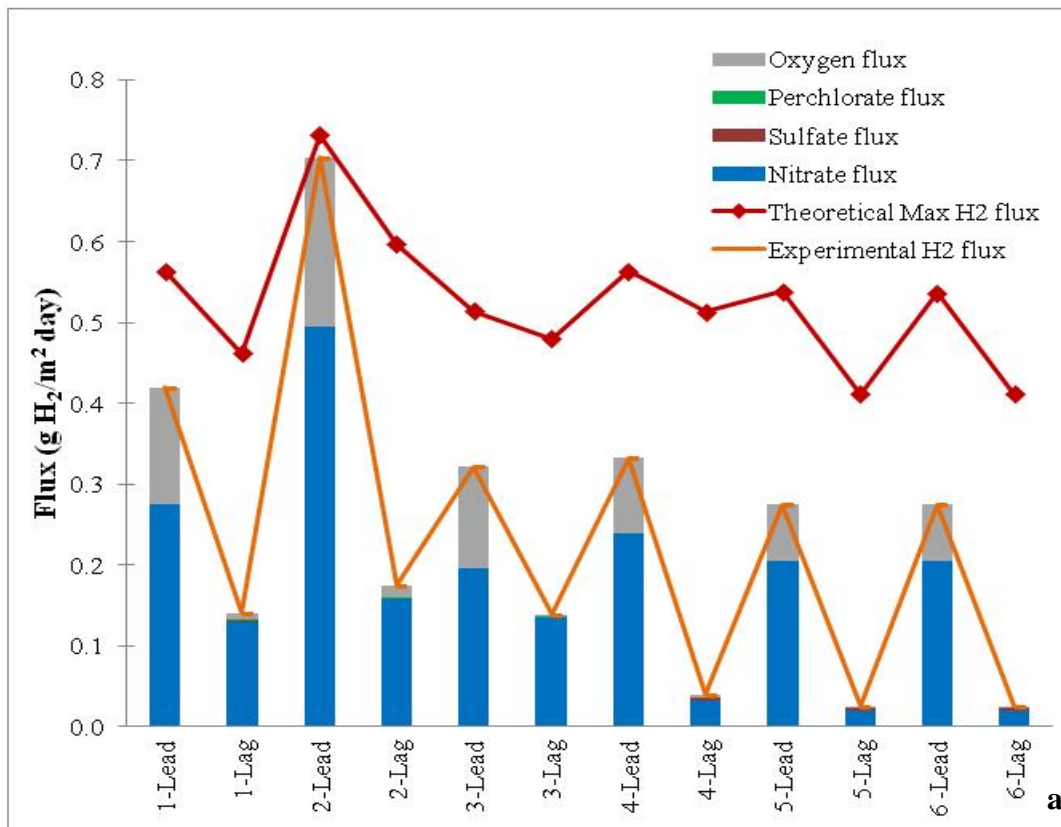


Figure 2a Electron acceptor fluxes (as H₂ consumption), along with experimental and maximum total H₂ fluxes for all shipments of lab and field modules. **2b** Corresponding operational conditions: H₂ pressure and flow rate (red dashed line).

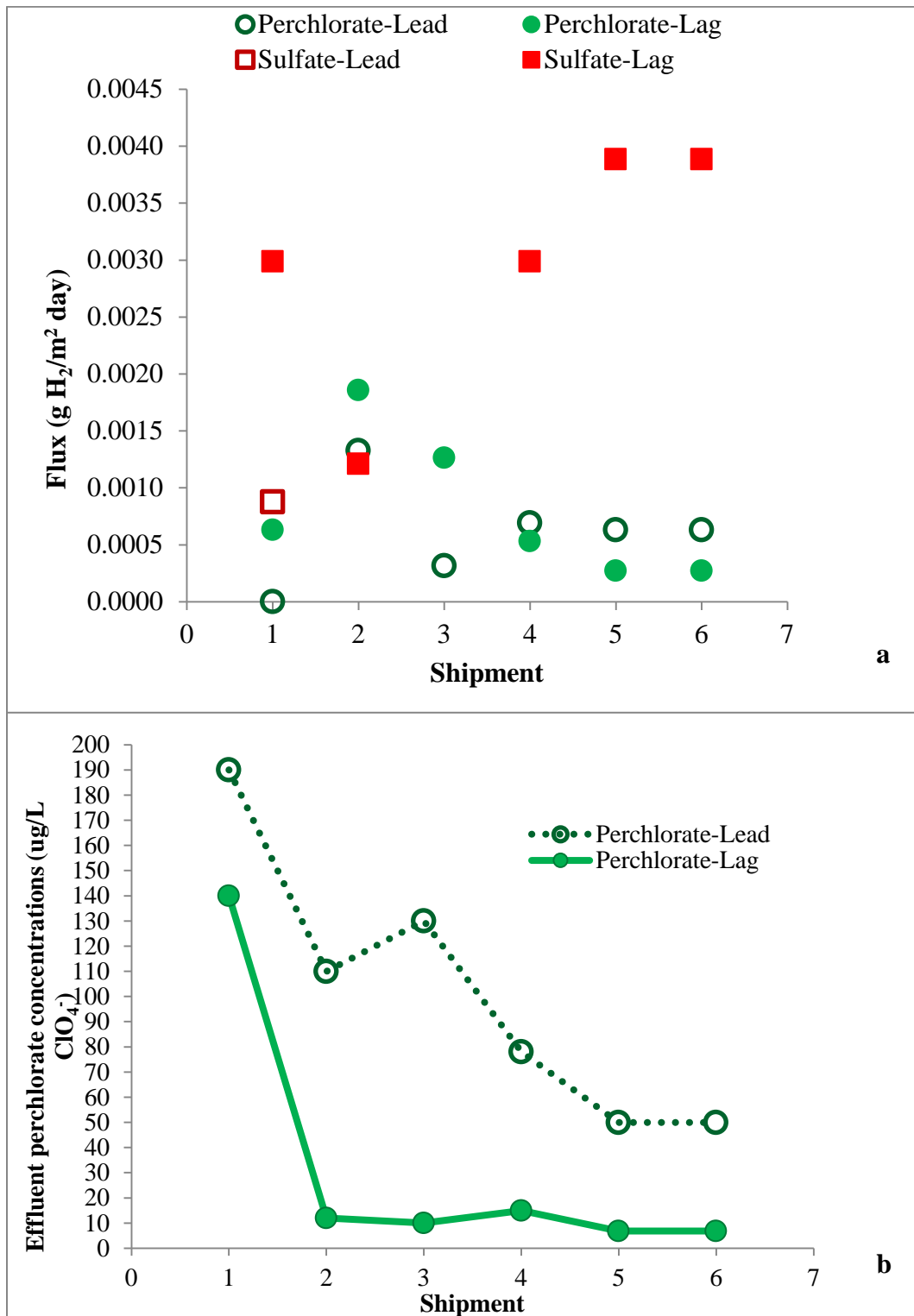


Figure 3a. Comparison of ClO_4^- and SO_4^{2-} fluxes for the pilot MBfRs at the times of module shipments. We lacked a SO_4^{2-} influent concentration for shipment 3, which explains the absence of SO_4^{2-} removal flux for that point. **3b.** Effluent ClO_4^- concentrations for lead and lag pilot MBfRs.

Chapter 2. Community Function and Structure

In this section, we synthesize the results of the quantitative Polymerase Chain Reaction (qPCR) analysis we did for the biofilm samples sent to ASU from the Rialto pilot site. We present results for the shipments of 5 side-reactors and 11 biofilm samples from broken reactor modules in the MBfR vessels, and we correlate them to the chemical fluxes reported in the previous section.

The procedures of DNA extraction and qPCR protocols are explained in detail in Ontiveros-Valencia et al. (2012) and Zhao et al. (2011). For RNA extraction, we directly cut a section of the fiber sheet and processed it (vortexing and centrifuging) while using "RNA protect bacteria reagent" all of the time. After collecting 1 mL of solution in a micro-centrifuge tube, we followed the manufacturer's protocol of the RNeasy Mini Kit (QIAGEN, USA). We then did 2 DNase treatments for 5 μ L of RNA each, and we ran PCR with 16S rDNA primers to confirm the absence of DNA contamination in the RNA samples. After successful DNase treatment, we performed reverse transcription PCR using an Omniscript RT kit to generate cDNA for downstream qPCR analysis, which followed the methods of Ontiveros-Valencia et al. (2012) and Zhao et al. (2011).

We normalized the qPCR data from gene copy numbers to cells by using the following conversion factors:

1 *dsrA* gene per cell of sulfate-reducing bacteria (SRB) (Kondo et al., 2004)

1 *nirK* gene per cell of denitrifying bacteria (DB) (Phillipot, 2006)

2 *nirS* genes per cell of DB (Coates et al., 2001)

1 *pcrA* gene per cell of perchlorate-reducing bacteria (PRB) (Coates et al., 2001)

4 16S rDNA genes per microbe cell. We took the average number of 16S rDNA genes found in Proteobacteria phylum, which is the expected dominant phylum in our samples, as reported by Kapplenbach et al. (2001) and Lee et al. (2008).

Figure 4 combines the electron-acceptor removal fluxes with the biomass distributions (cells/cm² of biofilm) for the lead MBfR (Figure 4a) and lag MBfR (Figure 4b) side-reactors. The lead MBfR was mostly utilizing the electrons donated by H₂ to reduce NO₃⁻ and O₂ (Fig. 2a). Since the lead and lag positions were switched every 3 days, the microbial communities from both MBfRs had similar biomass distributions. Thus, most of the changes were related to the changes in overall operating conditions, not to being in the lead or lag position.

DB comprised the largest fraction in biofilm samples from both MBfRs for shipments 1, 2, and 4. However, SRB became the highest microbial fraction for shipments 5 and 5*, when SRB had slightly higher cells/cm² than for total bacteria. This apparent discrepancy might be explained by the presence of *Archaea* that contain the *dsrA* gene (Muyzer and Stams; 2008). The reduction of flow rate (after shipment 2, Figure 2b) dramatically favored SRB.

DB assayed by the functional gene *nirS* gene were more abundant than DB assayed with the functional gene *nirK* gene (data not shown here). The abundance of *nirS* also was significantly higher in studies by Zhao et al. (2011) and Ontiveros-Valencia et al. (2012) in denitrifying MBfR biofilms. A single DB with both genes has not been reported. Ontiveros-

Valencia et al. (2012) discussed that DB with *nirK* are more sensitive to nutrient limitation, a situation that might favor the abundance of DB with *nirS* in autotrophic biofilms.

SRB (assayed by the functional gene *dsrA*) significantly increased their abundance for shipment 5 (Figure 4a&b). In terms of operational conditions, shipment 5 (challenge phase) showed the lowest flow rate tested (6 gpm) for the field MBfR (Figure 2b) and the largest SO_4^{2-} flux for the lag MBfR (Figure 4a&b). A reduction of flow rate for the field reactor increased the hydraulic retention time (HRT), which lowered the electron-acceptor surface loadings, a situation that favored the slow-growing SRB, which became the major biomass fraction in the biofilm for shipments 5 and 5*.

In both MBfRs, PRB (assayed by the functional gene *pcrA*) showed an increasing trend of their abundance over time, and they increased with the lower flow rate (Figures 4a&b and 2b), most noticeably for shipment 5. Of particular note is that PRB were the third largest fraction of the biofilm community, being out-numbered by SRB and DB. However, PRB cannot be clearly separated from DB, since some DB are capable of respiring ClO_4^- either by using a nitrate-reductase or by having the *pcrA* gene along with the *nirS* or *nirK* gene. Also, most PRB can reduce NO_3^- .

Figure 5 synthesizes the mRNA transcripts for all the shipments corresponding to lead (Figure 5a) and lag (Figure 5b) side-reactors. A comparison between Figures 4 and 5 shows higher numbers of transcripts than the number of cells for general bacteria/cm², which implies a highly active biofilm. The abundance of the transcripts for the lead and lag lab modules verifies that DB had the greatest activity for the first two samples, but SRB were similar to or even greater than DB for samples 4, 5, and 5*. Also, *pcrA* transcripts were significantly enriched in shipment 5 and 5*, although the difference between *pcrA* and *nirS/K* transcripts was lower than an order of magnitude. Lastly, *dsrA* transcripts were slightly higher than *pcrA* transcripts, but we should be cautious when interpreting differences lower than an order of magnitude with a logarithmic method such as qPCR.

Figure 6 shows results from DNA samples from the broken reactor modules in the MBfR vessels for shipments 3 (optimization phase) and 6 (challenge phase). The results are normalized to cells/cm² of biofilm. Samples 1-9 were sent to ASU as shipment 3, while samples APT 107 and APT 185 were sent to ASU as shipment 6. Table 2 provides the operational conditions for these two shipments. The abundance of general bacteria was not homogeneously distributed for all 9 samples for shipment 3. This might indicate an uneven distribution of biofilm across the field MBfR or some loss of biomass when handling the samples. Despite some variability, it is clear that DB and SRB established a strong competition for space within the biofilm community. DB were slightly higher for sample 3, but SRB were slightly higher for sample 6. PRB clearly were the smallest fraction within the microbial communities. These trends are consistent with the results for the side-reactors, and (as will be discussed in depth later) the biomass distributions correspond to the removal fluxes of the electron acceptors NO_3^- , SO_4^{2-} , and ClO_4^- . In particular, the flow rate was lowered between shipments 3 and 6, and this led to SRB becoming the largest portion within the biofilm community.

Figure 7 reports the mRNA transcripts for general bacteria and functional genes for the 9 samples of shipment 3 and 2 samples of shipment 6. Worth noting is that the biofilms were patchy in the reactor modules. This patchiness might correspond to the location of the biofilm sample within the reactor module (e.g., inner membrane sheet, top, or bottom of the reactor module). In parallel with the side-reactors, the number of transcripts for 16S rRNA were significantly higher than the number of genes for 16S rDNA, indicating that the biofilm was highly active. The number of transcripts for the functional genes *nirS*, *nirK*, and *dsrA* were smaller than the number of genes, while the number of transcripts for *pcrA* were slightly higher than the number of genes. Perhaps the most significant finding is the large increase of *dsrA* transcripts from samples for shipment 3 to samples for shipment 6. This reinforces that SRB were favored by the reduction of the flow rate and subsequent decrease on total electron acceptor surface loading (Table 2).

Figure 8 combines the electron-acceptor fluxes with the biomass distributions (in cells/cm²) for the field MBfRs. We report average values for each of shipments 3 and 6; this practice is supported by the similar biomass distributions we saw between lead and lag side-reactors. Figure 8 shows trends similar to those in Figures 6 and 7: DB, PRB, and SRB showed an increasing trend over time, but the increase was larger for the broken reactor modules in the MBfR vessels. Likewise, SRB out-numbered DB and PRB for shipment 6, which had a longer HRT and lower total-acceptor and NO₃⁻ fluxes for a significant amount of time (Table 2 and Figure 2b), even though the NO₃⁻ flux was much higher than the SO₄²⁻ flux. Ontiveros-Valencia et al. (2012) also observed high abundance of SRB in denitrifying MBfR biofilms regardless of SO₄²⁻ reduction activity. Clearly, the biofilm samples of side-reactors (Figure 4a&b) and reactor modules in the MBfR vessels (Figure 8) had many more SRB than PRB, and this seemed to favor incomplete ClO₄⁻ reduction in the lag MBfR. As interpreted by Ontiveros-Valencia et al. (2012), this high fraction of SRB could be active in O₂ respiration, fermentation of organics, and even NO₃⁻ respiration. Therefore, the metabolic diversity of SRB makes it not surprising that SRB had high abundance despite small or no SO₄²⁻ reduction. Regardless of the specific activity of SRB within the biofilm, they surely competed for electron donor and space situations with PRB.

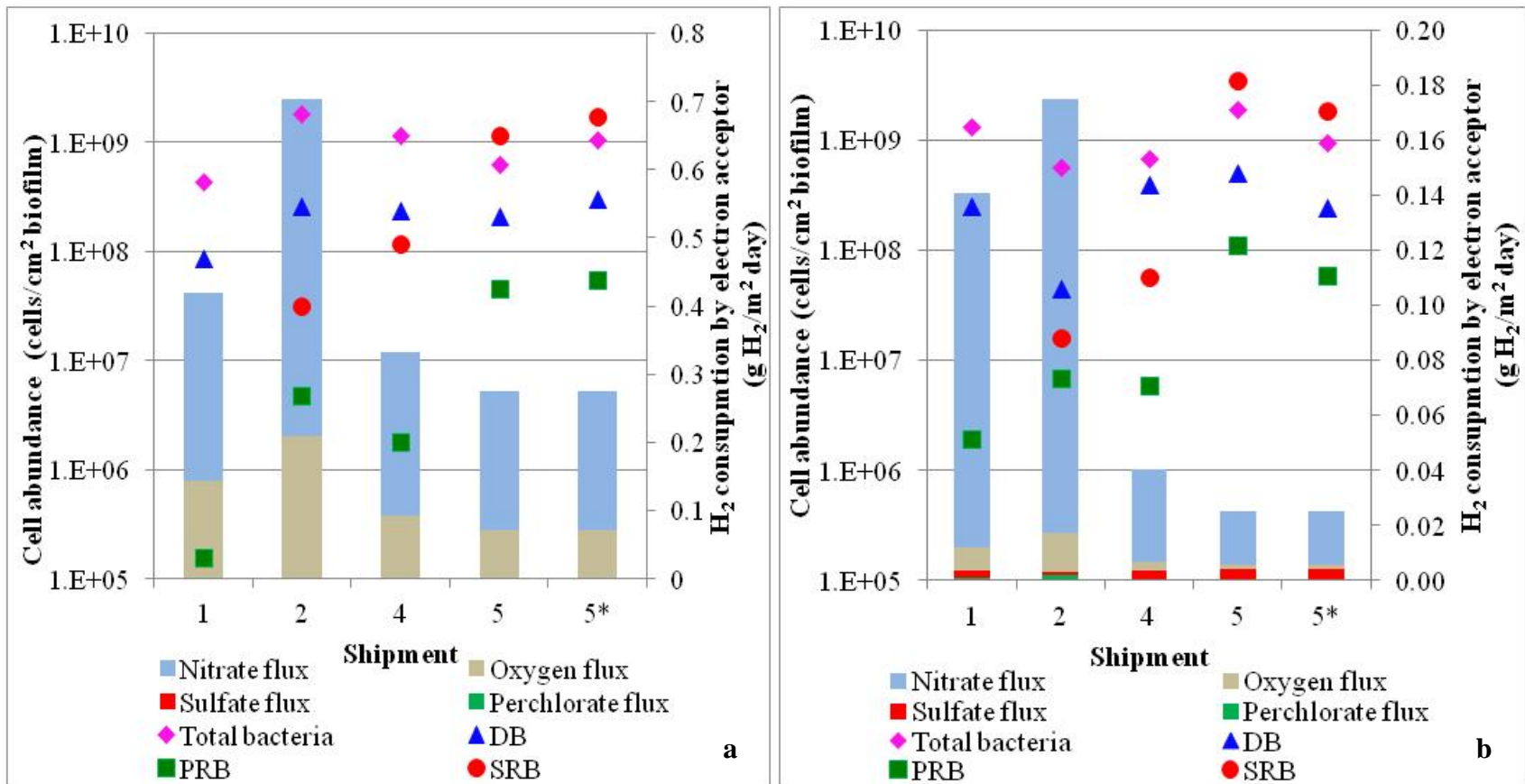


Figure 4. Microbial groups within the biofilm samples and corresponding acceptor fluxes (as H₂ consumption by each electron acceptor) for lead (4a) and lag (4b) side-reactors.

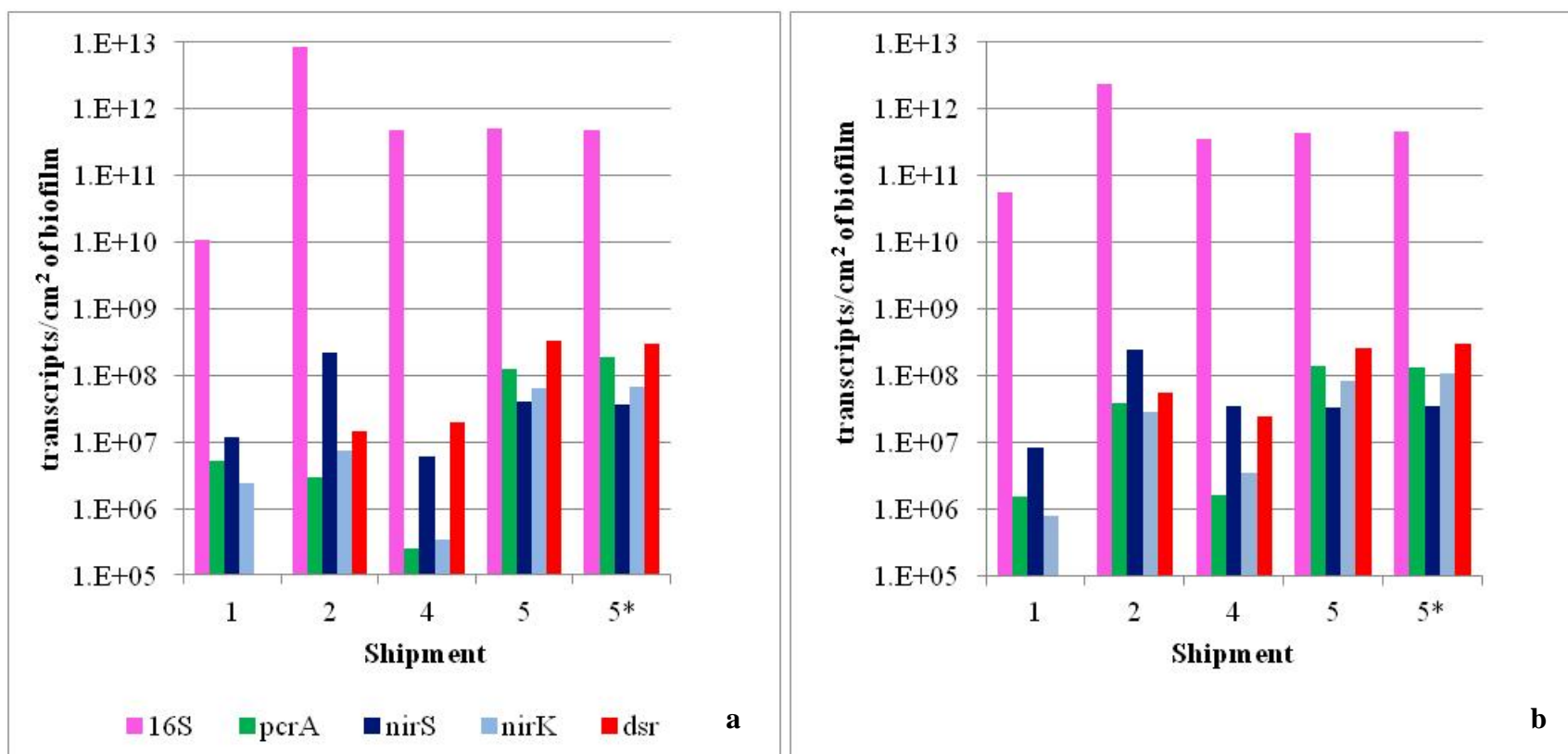


Figure 5. Abundances of total bacterial and functional transcripts (RNA samples) for lead (5a) and lag (5b) side-reactors.

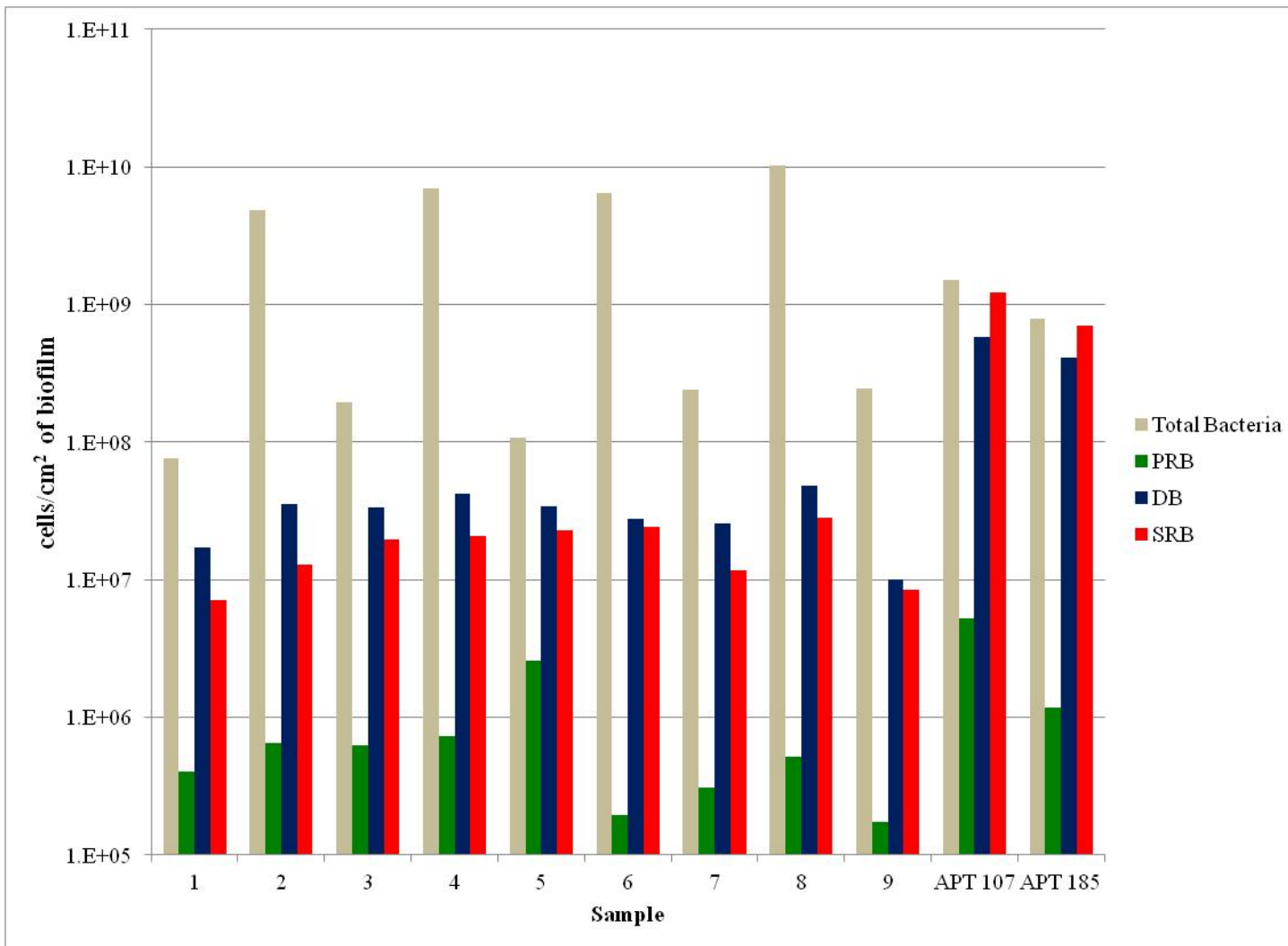


Figure 6. Biomass distributions for broken reactor modules in the MBfR vessels. Samples 1-9 correspond to shipment #3, while samples 107 & 185 correspond to shipment #6.

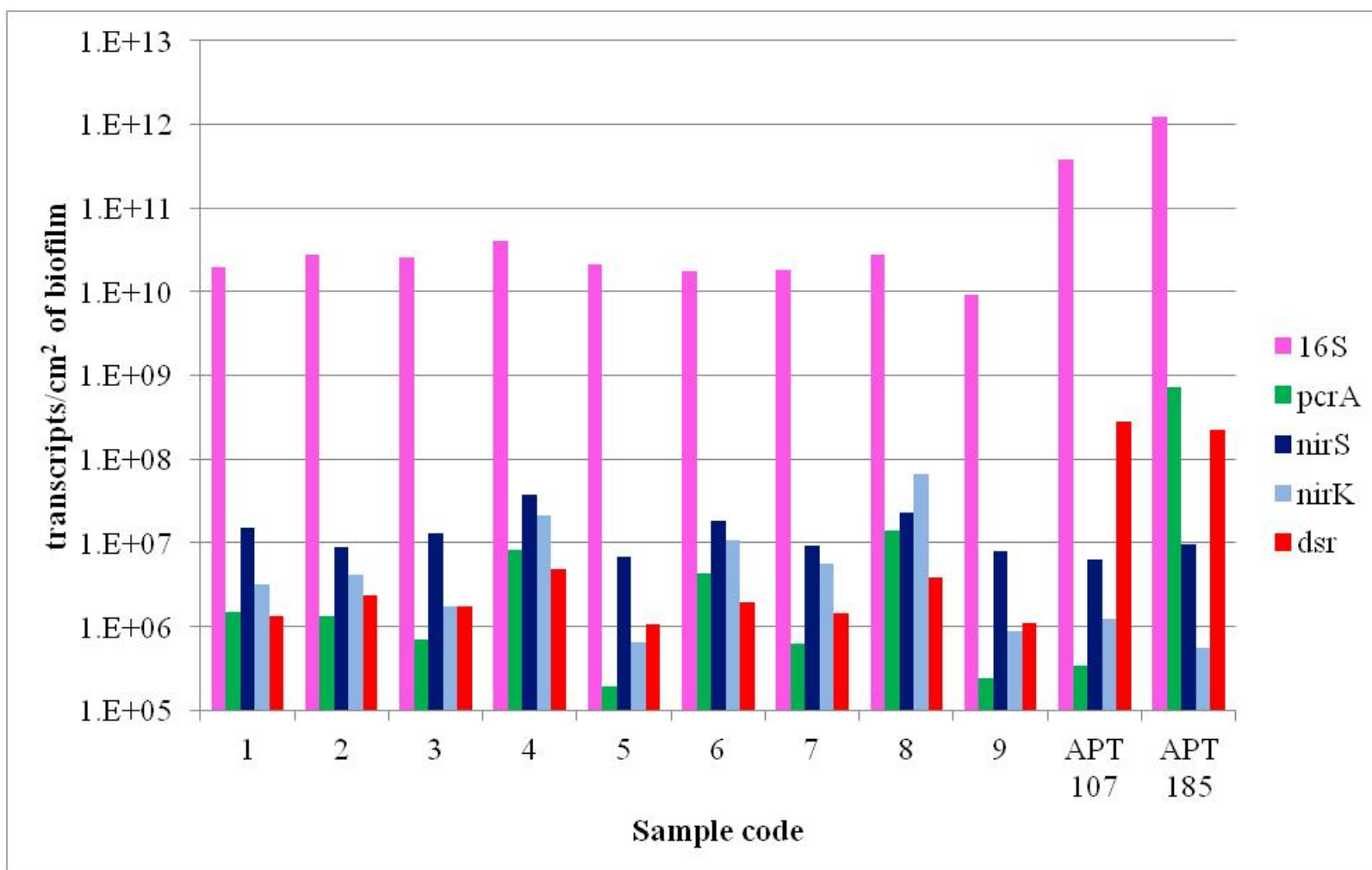


Figure 7. Abundances of total bacteria and functional transcripts for the broken reactor modules in the MBfR vessels. Samples 1-9 correspond to shipment #3, while samples 107 & 185 correspond to shipment #6.

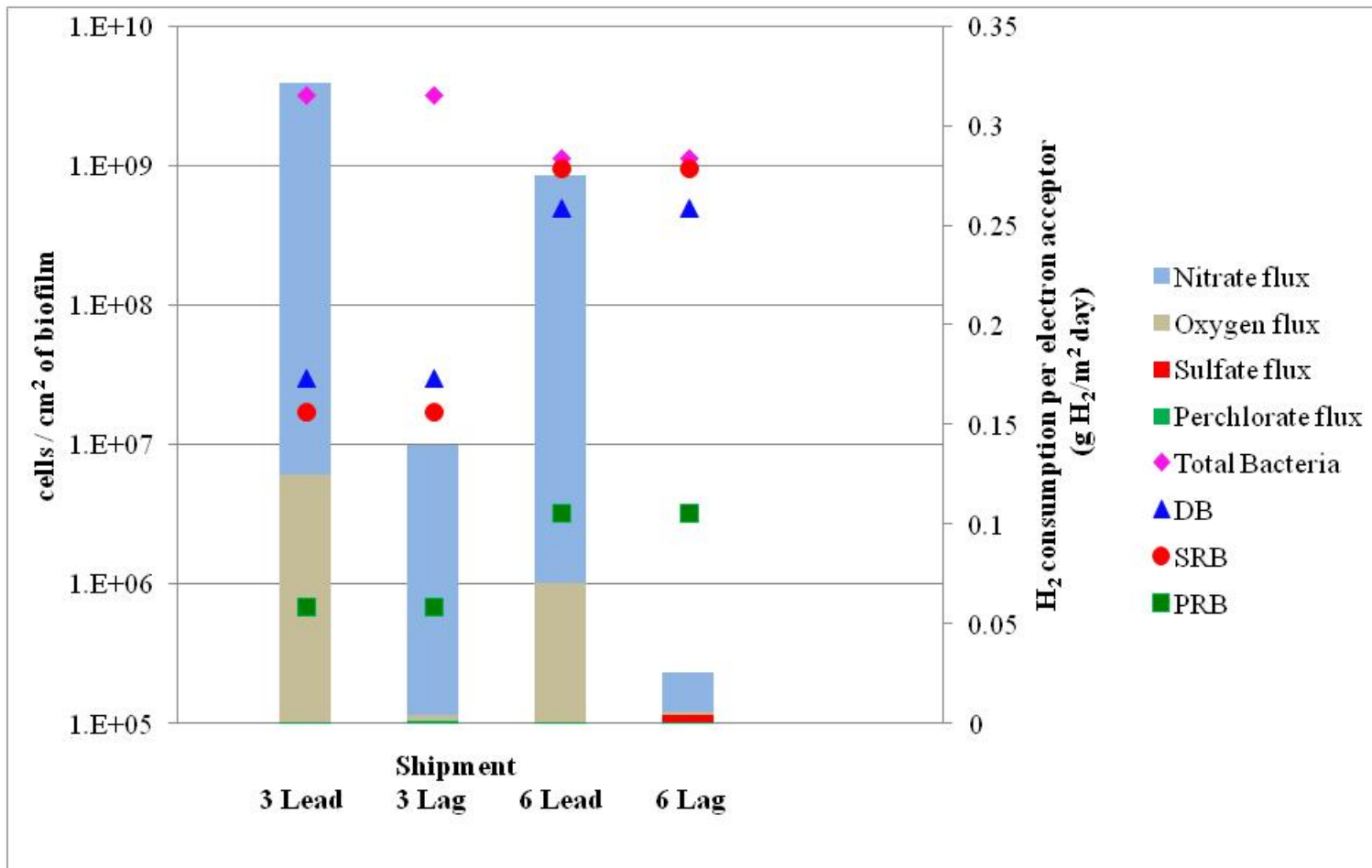


Figure 8. Microbial groups within the biofilm and acceptor fluxes (as H₂) for lead and lag field reactor modules in the MBfR vessels. The perchlorate fluxes are too small to see in three cases.

Chapter 3. Solids and EPS in the Biofilm

3.1 Solids analysis

Except for the first side-reactor, we collected biomass only from the fibers. The reason was that the significant agglomeration of biomass covering spacers in the side reactors had characteristics clearly distinct from the biomass on the fibers, where the H₂-based reductions took place. Some of these distinctions were color, viscosity, and texture. Also, when dismantling the side-reactors, we observed that the biomass associated with the spacers was separated from the fiber surface, further supporting that the biomass on the spacers was not receiving H₂ in the same manner as did the biofilm solids. Hence, we assumed that the biomass on the spacers was not representative of the biofilm carrying out H₂-based reductions, and we sampled only biofilm material for samples 2 – 6.

We measured TCOD, SCOD, TSS, VSS, TS, VS, and extracellular polymeric substances (EPS) for solids samples. We normalized the solids mass to the area of the corresponding fiber sheet. TCOD and SCOD were analyzed using Hach[®] COD vials (product #2415915), and TSS, VSS, TS, and VS were measured using *Standard Methods* 2540 A, 2540 B, 2540 D, and 2540 E, respectively (AWWA; APWA; WEF, 2011). Methods for EPS are summarized in the section that reports the EPS results. All biomass masses were normalized to the area of the corresponding fiber sheet. We applied a typical dense-biofilm VSS concentration of 50,000 g/m³ (Rittmann & McCarty, 2001) to estimate the thickness of the biofilm.

3.1.1 Solids analysis results

The average solids-analysis results for lead and lag MBfRs are summarized in Table 3. We differentiate the origin of biofilm samples as either from side-reactor or reactor modules in the MBfR vessels. For side-reactors, the solids from sample 1 were much higher than the others, a sign that they included suspended solids retained by the spacers. The solids of shipment 2 were by far the lowest among all samples. Although this correlates to H₂ limitation in the MBfRs (Figure 1), another explanation is that biomass continued to accumulate over time for the later shipments, although shipment 5 had relatively lower biomass. For the reactor modules in the MBfR vessels, the solids of shipment 6 were generally higher than those for shipment 3. A possible explanation is that the biofilm for shipment 6 was more metabolically active in respiring all electron acceptors, a situation enhanced by a significant increase in the HRT and an ample supply of H₂ as electron donor.

All samples had high %VSS/TSS and %VS/TS ratios, around 90% in all cases. This indicates low mineral precipitation due to successful pH control (Evans et al., 2013). The estimated biofilm thicknesses were around 200 μm when using a biomass concentration of

50,000 g VS/m³. The L_f values were not consistently different for the lead and lag MBfRs, the expected outcome of regular switching of their positions.

Table 3. Results of solids analyses for biofilm samples from side-reactors (red-shaded cells) and reactor modules in the MBfR vessels (blue-shaded cells). The solids in sample 1 were exaggerated due to including suspended solids trapped by spacers.

Parameter Shipment	1st		2nd		3rd	4th		5th		6th
	Lead	Lag	Lead	Lag	Lead/ Lag	Lead	Lag	Lead	Lag	Lead/ Lag
TCOD [g TCOD/m ²]	20	77	7.1	4.0	16.9	16.7	12.4	14.5	19.5	28.3
SCOD [g SCOD/m ²]	1.0	1.0	0.7	0.2	0.4	1.1	1.1	0.8	0.9	0.6
TSS [g TSS/m ²]	32	58	5.3	3.1	13	14	7.9	10	13	20
VSS [g VSS/m ²]	28	51	5.0	2.9	12.5	13.4	7.7	9.8	13.0	19
VSS/TSS [%]	87	87	94	94	95	94	97.2	95	97	96
TS [g TS/m ²]	13.0	41.0	6.8	6.0	14.5	16.8	13.0	9.9	12.5	21.1
VS [g VS/m ²]	12.0	33.0	5.4	3.3	13.6	14.8	10.0	8.7	11.5	19.2
VS/TS [%]	92	81	79	55	94	88	78	87	92	91
L _f , μm	560	1060	100	58	250	270	150	200	260	390

L_f was computed from the g VSS/m² and with an assumed biofilm VSS concentration of 50,000 gVSS/m³.

3.2 EPS analysis

Extracellular polymeric substances (EPS) are solid-phase products of bacterial metabolism that the cells use for aggregation, including attachment as biofilms. EPS offer other benefits to the microorganisms, such as formation of protective layer against harsh environmental conditions, protection against predation, and energy and carbon storage (Liu & Fang, 2002).

EPS are composed of various organic polymers that can be categorized roughly as carbohydrates, proteins, humics, and nucleic acids (Liu & Fang, 2002, Frølund et al., 1996; Sutherland and Kennedy, 1996; Cescutti et al., 1999; Veiga et al., 1997). Information on the four major components in EPS in biofilms is limited in general (Liu & Fang, 2002) and absent for MBfR biofilms.

We analyzed EPS components for every biofilm sample. We first extracted EPS using the NaOH + formaldehyde method, since it gives highest yield reported in literature (Liu & Fang, 2002). Then, we used the phenol-sulfuric acid method to measure carbohydrates (Dubois, et al., 1951), the Folin method to measure humics (Box, 1983), and the BCA method for protein

analysis (Thermo Fisher Scientific Inc., 2011). We converted all EPS component values into g COD/m² based on the conversion factors for protein (1 g protein = 1.5 g COD), carbohydrates (1 g carbohydrate = 1.1 g COD), humic substances (1 g humics = 1.34 g COD), and nucleic acids (1 g nucleic acids = 1.1 g COD) (Rittmann & McCarty, 2001).

Figure 9 synthesizes the average amount of EPS for the side-reactors and reactor modules in the MBfR vessels. Most EPS measurements were in the range of 7 to 9 g COD/m²; however, EPS results for shipment 1 were significantly higher (~32 g COD/m²). The high value for sample 1 corresponds to the inclusion of biomass from the spacers in the extraction of EPS for shipment 1. We standardized biofilm sampling for shipments 2 through 6 to capture only biofilm from fibers. Except for shipment 2, the EPS-COD constituted 36 – 52% of the TCOD. Thus, a substantial portion of the biofilm was EPS, not active cells.

For the side-reactors and reactor modules in the MBfR vessels for shipments 2 - 6, humic substances accounted for the highest portion of the EPS, followed by proteins and carbohydrates. The distribution was quite different for shipment 1, another sign that it contained solids other than bacteria. We do not have a conclusive understanding about the role of humic substances in the biofilm development and its EPS. Perhaps the most logical reason for the relatively large build up of humics is that they are hard to biodegrade (Blondeau, 1988; Masahiro et al., 2008). Clearly, more research would be needed to know why humics comprised the largest portion in the MBfR biofilms. Lastly, the low values of nucleic acids suggest that EPS extraction occurred with minimum cell lysis, an indication that the analysis was conducted correctly.

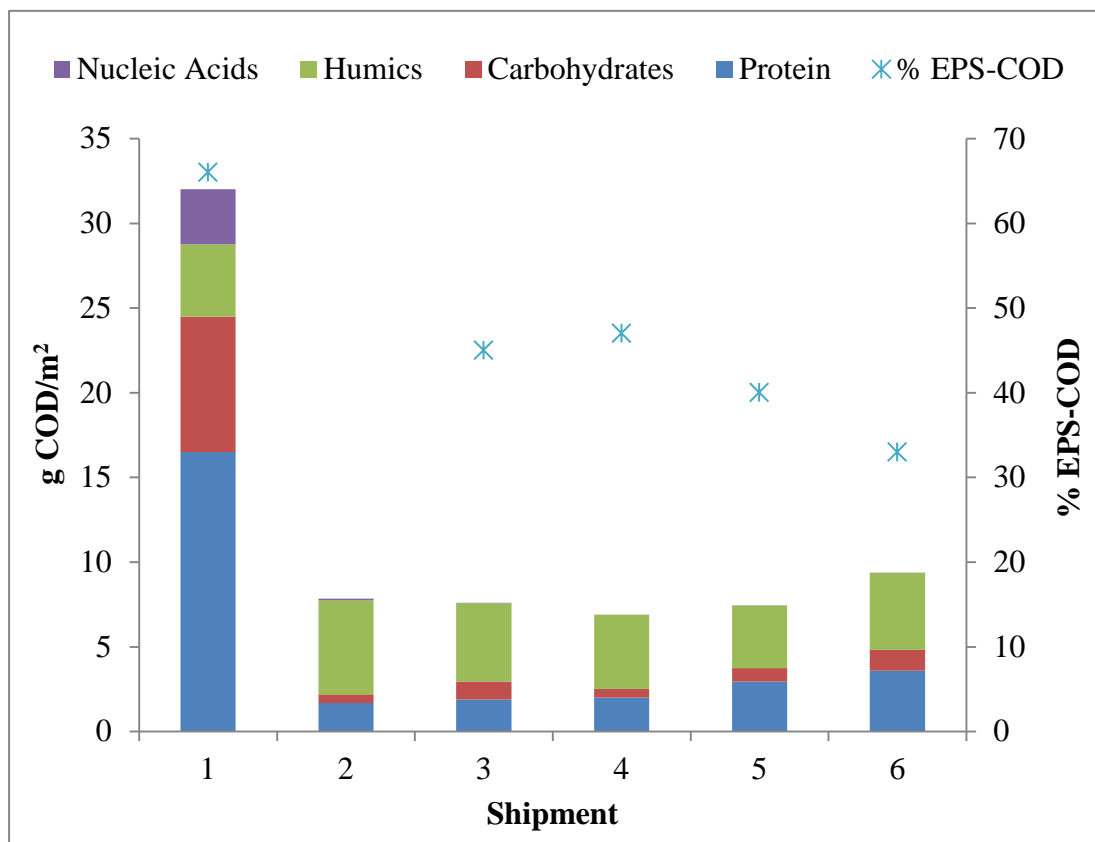


Figure 9. Breakdown of EPS components for the six shipments, as well as the percentage of the biofilm’s TCOD that is EPS-COD. Samples 1, 2, 4, and 5 correspond to lab modules, while samples 3 and 6 correspond to field MBfRs.

Chapter 4. Microscopic Analysis on Distribution of Live and Dead Portions within the Biofilm

For shipments 2 - 6, a subset of samples from the fiber sheet was taken for confocal laser scanning microscopy (CLSM) analysis, a technique used to visualize biofilms at high resolution with depth selectivity. With CLSM, we can observe specimens one-level depth at a time, while the computer software provided with the CLSM equipment can aggregate these individual observations at a particular depth to construct a final three-dimensional image. For visualization, we used the Live/Dead staining kit from Invitrogen (USA). Cells with undamaged membranes are stained green with SYTO9 dye at a wavelength of 488 nm, while cells with damaged membranes are stained red with propidium iodide at a wavelength of 543 nm. Green zones are considered live portions of the biofilm, while the red zones are considered dead. The kit we used to perform the CLSM analysis just captures cells membranes and is unable to quantify EPS within the biofilm.

Here, we report key findings across the different shipments, and we only include figures that highlight the key conclusions.

For shipments 2 and 3, we took individual fibers from the fiber sheets. Figure 10 shows representative images from shipment 3. The fluorescent green and red zones from one fiber sample from the lab module are shown in three ways: live (10a), dead (10b), and combined (10c). Due to possible artifacts from removing individual fibers from the sheet before CLSM, the thicknesses are not necessarily representative of the biofilm on the sheet or the absolute amounts of live or dead cells. In contrast, the chemical analysis performed with intact fiber sheets should give more representative thickness values for the entire sheet. Perhaps more important is that the biofilm used for CLSM appeared to be uneven. A possible explanation for unevenness is biofilm loss during shipping and processing the fiber sample. Thus, to reduce the amount of biofilm detachment, we decided to analyze a sample of ~ 0.5 cm x 0.5 cm of fiber sheet for further shipments.

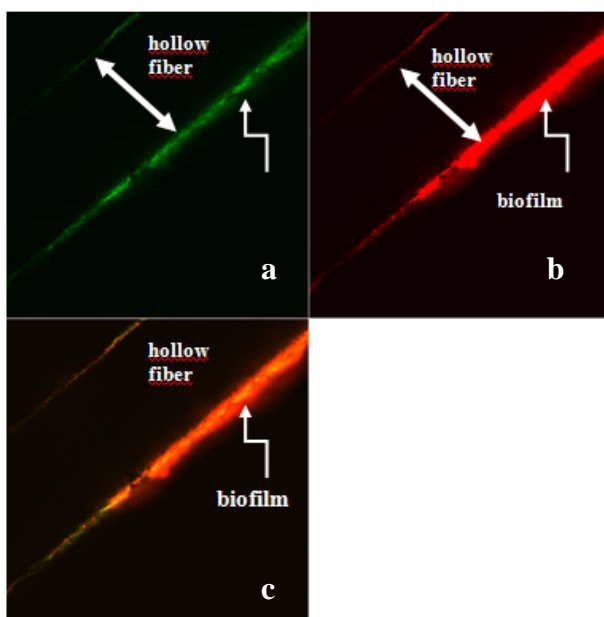


Figure 10. Live and dead portions in the biofilm from side-reactor in the lag position at time of shipment 3. Images were taken with 40X resolution. The fiber is in the middle, with biofilm on either side. The biofilm thickness shown here is ~ 20 μm . The panels are: live (10a), dead (10b), and combined (10c).

The uneven distribution of the biofilm is well illustrated with a 3D view of the biofilm from side-reactor samples corresponding to shipment 5, shown in Figure 11. Figure 12 shows the intensities captured by the green and red channel for the same sample, but it is a 2D representation accompanied by a visualization of the biofilm at the top. Higher intensity for the green or red channel correlates to higher abundance of live or dead cells, respectively. Across

the biofilm sample, the intensity received by the green channel was higher (Figure 11a and 12) than the intensity received by the red channel (Figure 11b and 12); however, the live/dead assay should not be interpreted quantitatively due to possible artifacts caused by sample shipping and handling. While the living cells were more evenly distributed than the dead cells, the overall interpretation may be that the biofilm had an uneven distribution for bacterial cells, which corresponds to the visually patchy nature of the biofilms. The CLSMs do not show the distribution of EPS, which may make the biofilm more physically homogeneous than for the bacterial cells.

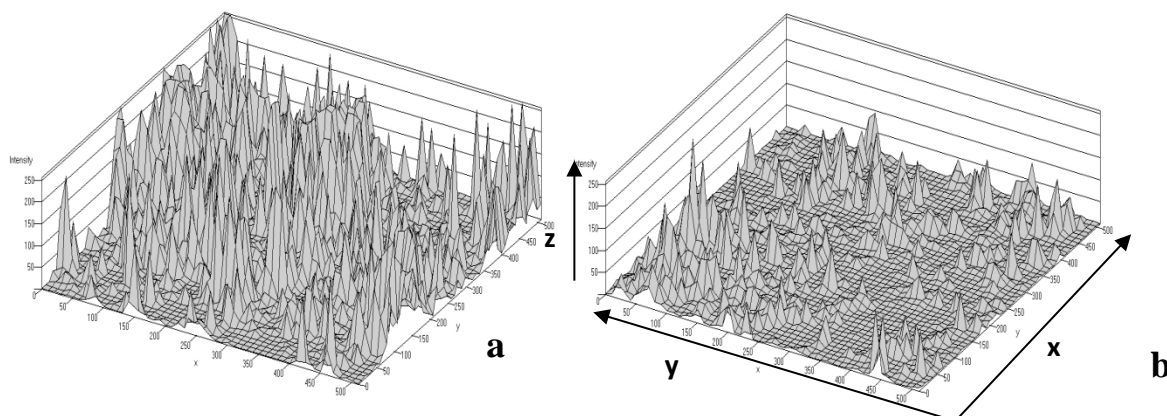


Figure 11. 3D representation of biofilm from lab-module R100D. The portions of the biofilm stained green (a) and red (b) are illustrated according to an x-y-z vector graph, where x and y are the length and width of sample analyzed, and z is the intensity of the fluorescent signal. A higher z intensity represents a higher abundance of either live cells (left) or dead cells (right).

The apparent differences between Figure 10 and Figure 11 probably are explained by the sampling procedures before CLSM. While Figure 10 shows a single fiber, Figure 11 shows a portion of a fiber sheet sample (~0.5 cm X 0.5 cm). Thus, less biofilm detachment probably occurred for the sample illustrated in Figure 11 than for Figure 10. If this is true, then the relative proportions between live and dead cells are better represented by Figure 11, and indicates that live cells are more significant than dead cells within the biofilm.

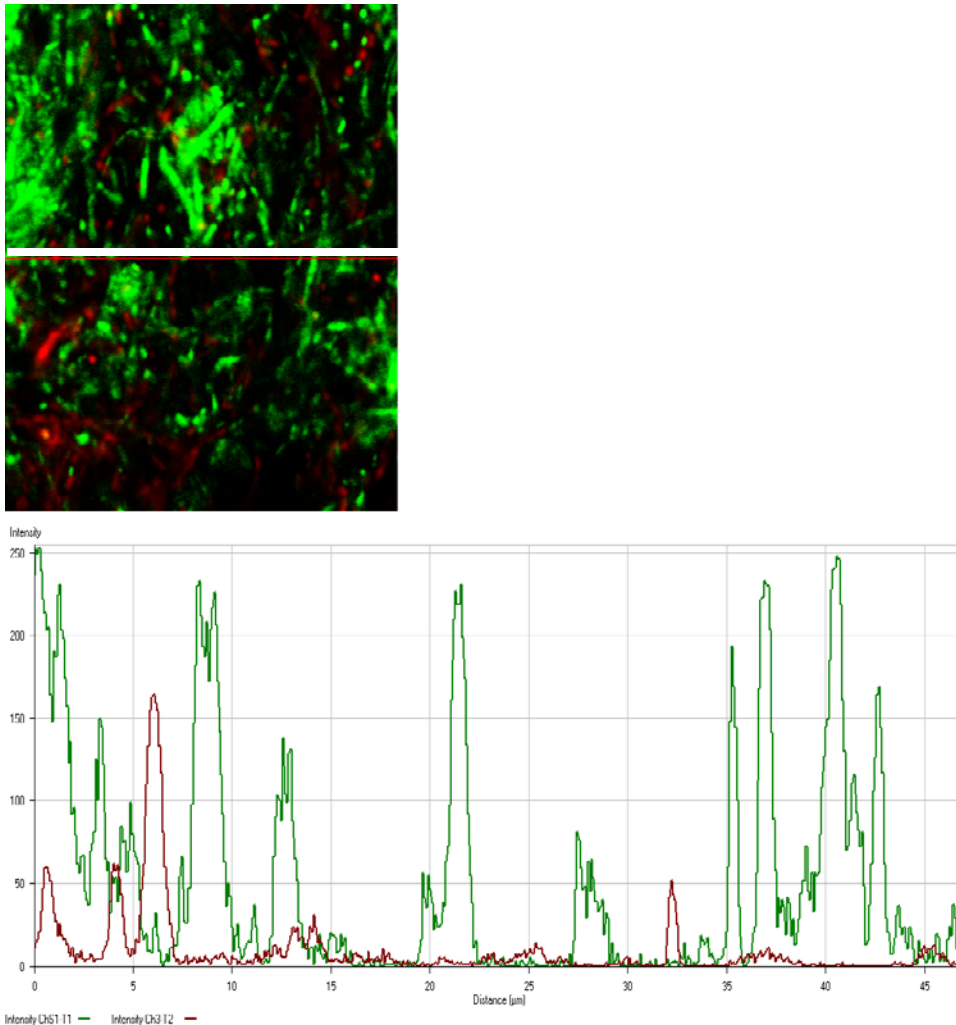


Figure 12. 2D graph of the intensities caught by the green and red channels. The top shows the 2D image, while the bottom shows the intensities along the transect indicated by the red line in the top image.

To investigate further if the biofilm was mostly populated with living areas rather than dead areas, we took several images of the same biofilm sample from a fiber sheet, but from different areas. Figure 13 shows the 3D representations of the intensities received by the green channel (Figure 13a) and red channel (Figure 13b) for the biofilm from the field sample coded as APT107 (shipment 6). The 3D representation in gray scale of the same sample for the green and red channel is also included to help understanding the location and coverage of living and dead portions within the biofilm. The 3D images make it clear that the biofilm had substantially more live biomass than dead biomass. Furthermore, the live biomass was more uniform.

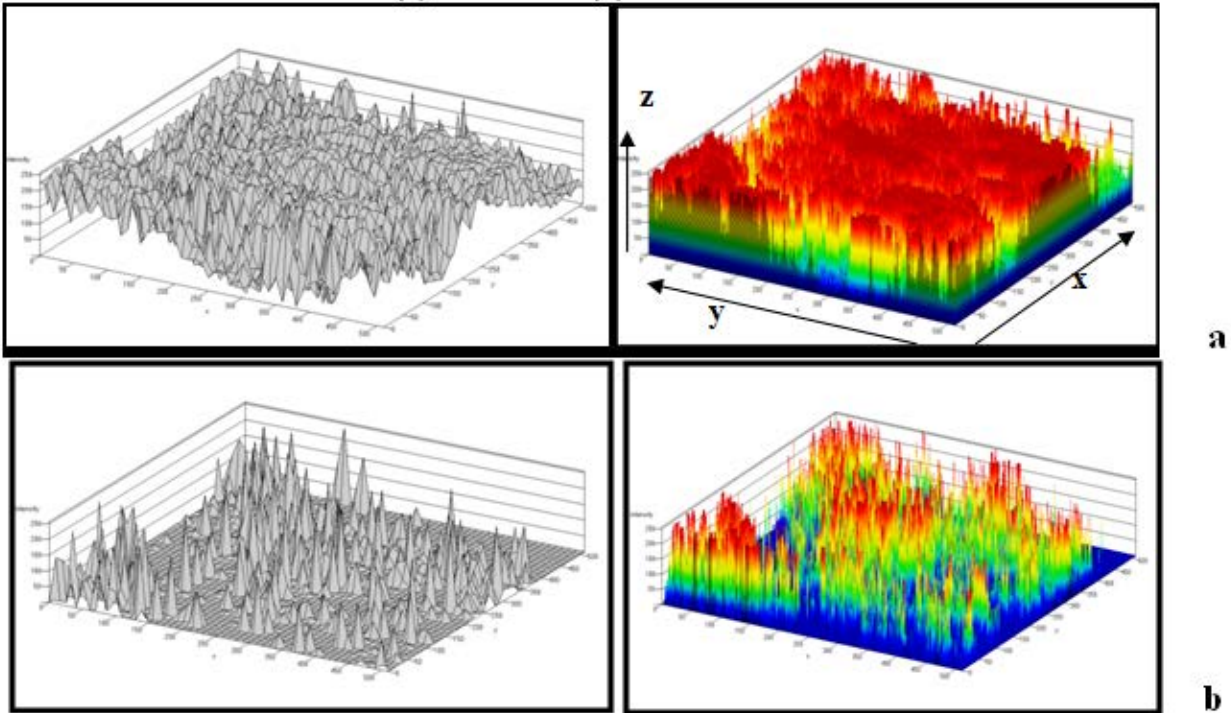


Figure 13. 3D black (left) and color (right) representation of biofilm from field sample coded as APT107, first spot. The portions of the biofilm that stained green (a) and red (b) are illustrated according to a x-y-z vector graph, where x and y are the length and width of sample analyzed, and z is the intensity of the fluorescent signal. A higher intensity represents a higher abundance of either live cells (a) or dead cells (b).

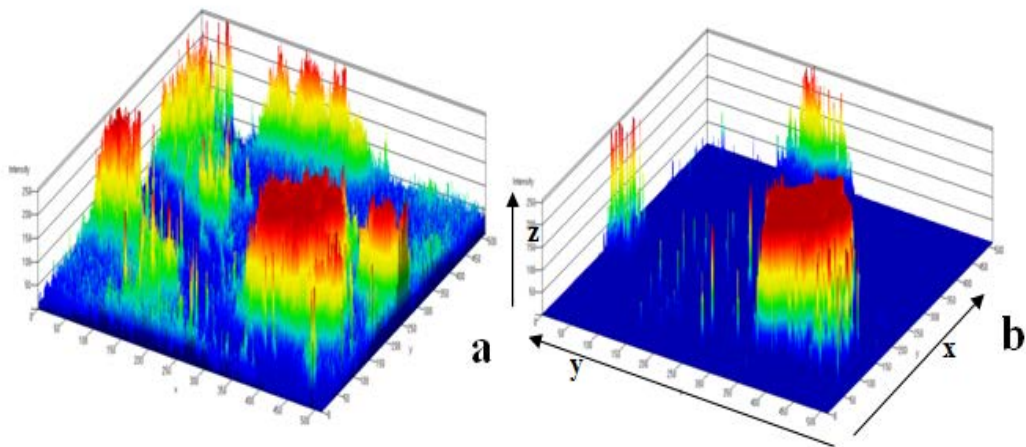


Figure 14. 3D color-representation of biofilm from field sample APT107, second spot. The portions of the biofilm that stained green (a) and red (b) are illustrated according to a x-y-z vector graph, where x and y are the length and width of sample analyzed, and z is the intensity of the fluorescent signal. A higher intensity represents a higher abundance of either live cells (a) or dead cells (b).

Figure 14 is from the biofilm of sample APT107, but for a second spot. It shows the same pattern of dominant living zones as in Figure 13, but all of the biomass appears patchier for this spot.

Another important observation that can be taken from CLSM imaging is illustrated well in Figure 15, which shows a gallery of Z-scans from the attachment substratum to the outer surface of the biofilm. The living portions (green zones) are closest to the fiber. When H_2 is limiting, the active biomass tends to grow best close to the fiber, where it has better access to H_2 . This trend is consistent with modeling results presented later. Reinforcing this trend is that water flowing past the biofilm creates forces that help remove the outer layer of the biofilm, which reduces the total biofilm thickness. Since the active biomass is farthest from the liquid, the most active biofilm is relatively protected from detachment. This usually is good for MBfR performance, because a thin and highly active biofilm promotes solute mass transport from the bulk liquid to the active portion of the biofilm. Substrates (e.g., NO_3^-) must diffuse into the biofilm to promote growth, and alkalinity must diffuse out of the biofilm to maintain a suitable pH. These complementary trends, which tend to keep the MBfR biofilm active, also are reflected in the clear trends that the biomass is much more active than dead (e.g., Figures 10 – 14) and has little inorganic solids (Table 3).

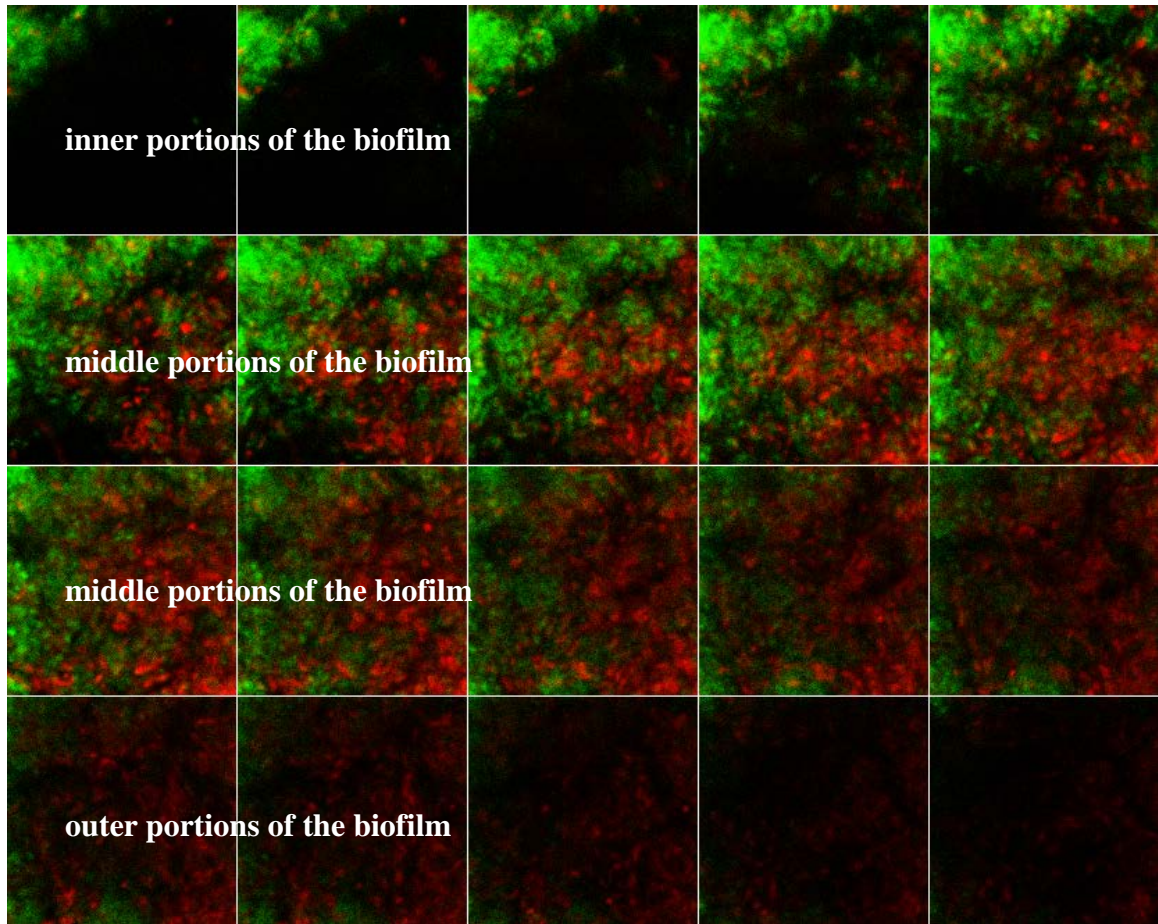


Figure 15. Combined overlay at 40X of biofilm from the pilot reactor for shipment #3. Live cells stain green, while dead cells stain red. This figure is a gallery of the Z-scan function provided by the software of the CLSM, and the 20 panels represent a depth of view of ~150 μm , which is consistent with the typical biofilm thickness in Table 3. The Z-scan function layers the specimen at different depths. Each square is the dissection procedure done by the confocal laser at different depths in the specimen. The spatial distribution of the live and dead cells is clear. The inner layers (closest to the fibers) are almost totally active, while the outer layers (near the liquid) have a predominance of dead cells.

Chapter 5. Synthesis for the Side-Reactors and Reactor Modules in the MBfR Vessels

We conclude with a synthesis of the major findings for the acceptor fluxes, microbial community structure, EPS composition, and CLSM imaging for the side-reactors and reactor modules in the MBfR vessels at Rialto. We offer preliminary interpretations about why the pilot MBfRs failed to meet consistently the $6\text{-}\mu\text{g/L}$ goal for ClO_4^- , even though they performed well for acceptor removal overall. These interpretations are tested and refined by the laboratory experiments and modeling summarized in the next sections.

a) The relative magnitudes of the surface loadings for the electron acceptors allowed denitrification and O₂ respiration to control the flow of electrons from H₂ in the lead MBfR. The lead MBfR was responsible of reducing 70-90% of the NO₃⁻ loading and 99% of the O₂ loading. The NO₃⁻ + O₂ surface loading of ≥ 0.3 g H₂/m²-day suppressed SO₄²⁻ reduction.

b) The NO₃⁻ influent concentration for the lag MBfR was 0.2-4.4 mg N/L, which allowed the onset of SO₄²⁻ reduction in the lag MBfR. Quantitatively, a NO₃⁻ flux < ~0.1 g H₂/m²-day allowed SO₄²⁻ reduction in the lag MBfR when H₂ delivery was not limiting.

c) ClO₄⁻ respiration was observed in the lead and lag MBfRs, but the highest ClO₄⁻ reduction occurred at the lag MBfR, where competition from NO₃⁻ and O₂ respirations was minimized.

d) ClO₄⁻ reduction flux in the lag MBfR was inversely correlated to the SO₄²⁻ flux. A SO₄²⁻ flux of 0.003 g H₂/m²-day or more seemed to slow ClO₄⁻ reduction. A SO₄²⁻ flux of 0.001 g H₂/m²-day allowed the highest ClO₄⁻ flux.

e) Operational conditions applied to field MBfRs affected the microbial communities in ways that corresponded to acceptor fluxes. When acceptor surface loadings were high due to a high flow rate, the field MBfRs (especially the lead MBfR) experienced a limitation of H₂ delivery, and DB were dominant. Increasing the HRT, which decreased the surface loading for all acceptors, eliminated H₂ limitation, but at the expense of favoring SRB, whose metabolic versatility helped them remain in the biofilm regardless of SO₄²⁻ reduction activity.

f) The chemical and physical characteristics of the biofilm were similar for all conditions. All samples had a high ratio of % VS/TS and % VSS/TSS (~90%), indicating minimum mineral precipitation. The biofilm thickness was around 200 μm, EPS was a large portion of the biofilm mass (~ 40-50%), and EPS was dominated by humics, with proteins also important. Based on rRNA copies, mRNA transcripts, and CLSM visualization, the biofilms were highly active, particularly near the membrane substratum. Finally, the biofilms had uneven distributions of live and dead cells.

In summary, while the two-stage pilot system had an active biofilm and was effective for reducing NO₃⁻ and ClO₄⁻, it did not reliably achieve the 6-μg/L ClO₄⁻ goal because lowering the ClO₄⁻ surface loading also lowered the loading of all acceptors. In particular, low surface loading of NO₃⁻ in the lag MBfR led to SO₄²⁻ reduction, which had a negative impact on the rate of ClO₄⁻ reduction. For instance, shipments 4-6 had significantly higher HRT and thus smaller surface loadings for all acceptors (Evans et al., 2013); this situation allowed SRB to outcompete DB and PRB in the lag MBfR.

To control the overgrowth of SRB and achieve a very low effluent ClO₄⁻ concentration, the NO₃⁻ + O₂ surface loading has to be significant, but it should not be too large to cause excessive competition from denitrification and DB. Based on the pilot results, the NO₃⁻ + O₂ surface loading for the lag MBfR should be in the range of 0.1 – 0.3 gH₂/m³-day. This strategy is addressed in some of the bench-scale experiments reported in the following sections.

Chapter 6. Exploring Mechanisms and Performance with Bench-Scale Experiments

The ASU team carried out a series of bench-scale experiments designed to elucidate critical kinetic and ecological mechanisms that control the performance of the MBfR when ClO_4^- reduction to $\mu\text{g/L}$ concentrations is the goal. Of over-arching importance is that multiple electron acceptors are present in the influent water: O_2 , NO_3^- , SO_4^{2-} , and ClO_4^- . Typically and in the case of the Rialto field study, ClO_4^- is present at by far the lowest concentration. This means that PRB must compete for the common electron donor (H_2) and space in the biofilm with bacteria that reduce the other acceptors. The competition can be an important factor controlling whether or not the PRB are able to reduce ClO_4^- to very low concentrations.

In a series of experimental studies, the ASU team evaluated competition for H_2 and space among PRB, DB, and SRB. Three of the studies focused specifically on the ability to reduce ClO_4^- to $\mu\text{g/L}$ concentrations, while three others provided foundation information needed to interpret the studies about ClO_4^- reduction. All bench scale-related work was developed in 60-mL (total volume) MBfRs, as illustrated in Figure 16. This section provides a succinct summary of each experimental study and how they relate to the pilot performance. Each study resulted in a published or accepted manuscript that is listed at the beginning of each summary.



Figure 16. Bench scale MBfR showing the biofilm development on the fiber's surface.

6.1 Permeation Rates for Hydrogen Gas Through MBfR Fibers

Tang, Y., C. Zhou, S. Van Ginkel, A. Ontiveros, J. Shin, and B.E. Rittmann (2012b). Hydrogen-permeabilities of the fibers used in a H₂-based membrane biofilm reactor. *J. Membrane Sci.* **407-408**: 176 – 183.

The capacity to deliver the H₂ electron donor by diffusion through the walls of the gas-transfer fibers is fundamental information needed to interpret all of the experimental results, as well as to model and design MBfRs. In this published study, we developed and used steady-state permeation tests and a mathematical model to determine the H₂ permeabilities of the three hollow fibers commonly used in the H₂-based MBfR: composite from Mitsubishi-Rayon, polypropylene from Teijin, and polyester from Teijin. The H₂ permeabilities spanned a wide range: 1.6×10^{-6} , 1.8×10^{-7} , and 6.6×10^{-8} m³ H₂ @ standard temperature and pressure • m membrane thickness / (m² hollow fiber surface area • d • bar) for the composite, polypropylene,

and polyester hollow fibers, respectively; this represents a ratio of the maximum H₂ flux for composite: polypropylene: polyester hollow fibers = 32: 3.3: 1.

The H₂ permeabilities were then used to correlate hollow-fiber type to contaminant-removal flux from a wide range of previous MBfR experiments. As shown in Figure 17, only the experiments with composite hollow fibers were not routinely limited by H₂ delivery. However, the composite fiber was susceptible to fouling by mineral precipitates in its outer-layer micropores, and this lowered the H₂ flux in some cases with the composite fibers. The Teijin polypropylene fibers, which have no micropores and were used in the Rialto pilots, did not seem to be affected adversely by mineral precipitation. Having the permeability values made it possible to determine whether or not the bench-scale or pilot-scale experiments were limited by the H₂-delivery capacity. For the field-pilot studies, the H₂ delivery capacity was substantially greater than the H₂-consumption rate for most of the experimental program, except for the start up phase when side-reactor shipment 2 was delivered.

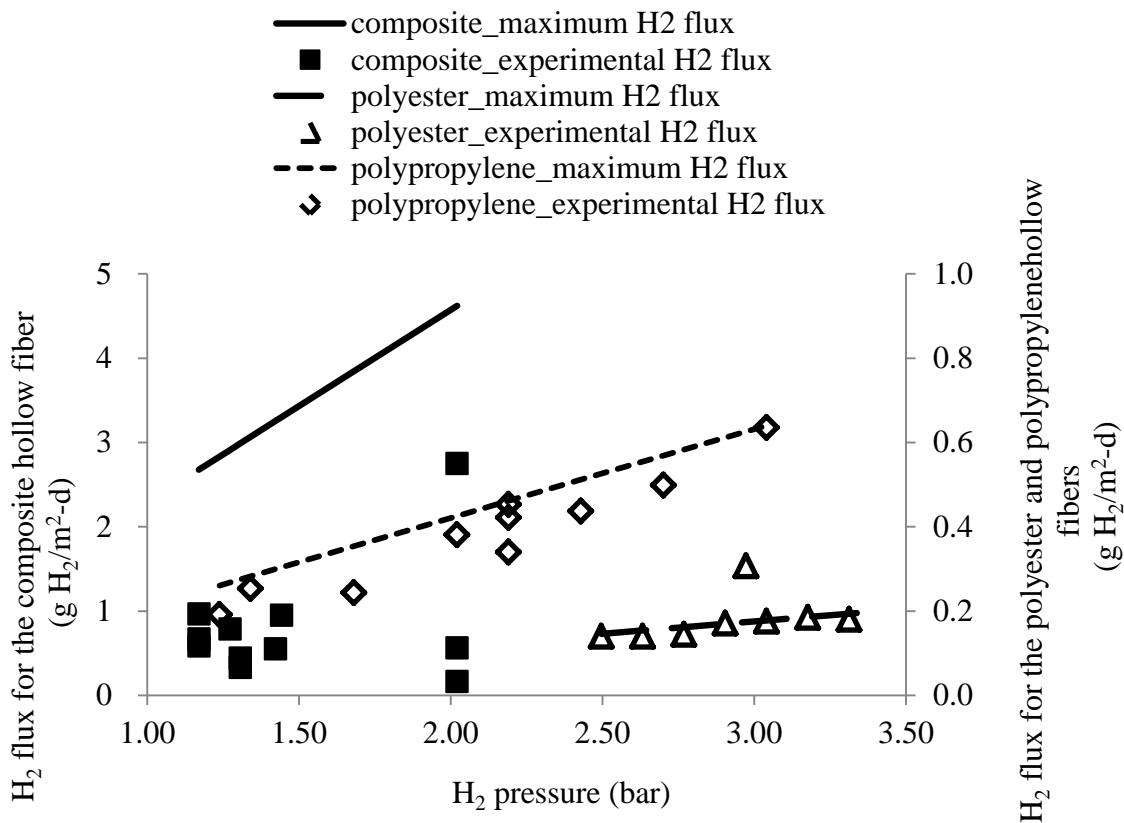


Figure 17. Comparison of maximum-possible H₂ fluxes and experimentally measured H₂ fluxes in MBfR experiments. The maximum-possible flux occurs when the water-phase concentration of H₂ is zero.

6.2 Ecological Interactions Between DB and SRB in the MBfR Biofilm

Ontiveros-Valencia, A., M. Ziv-El., H.-P. Zhao, L. Feng, B. E. Rittmann, and R. Krajmalnik-Brown (2012). Interactions between nitrate-reducing and sulfate-reducing bacteria coexisting in a hydrogen-fed biofilm. *Environ. Sci. Technol.* **46**: 11289-11298.

To explore the relationships between DB and SRB in H₂-fed biofilms, we operated two H₂-based MBfRs (bench-scale) with or without restrictions on H₂ availability. H₂ availability was gauged from the H₂ pressure and the H₂ permeabilities reported by Tang et al. (2012) (previous section) for the polypropylene fibers. Since DB and SRB compete for H₂ and space in the biofilm, SO₄²⁻ reduction should be out-competed by NO₃⁻ reduction when H₂ is limiting inside the biofilm, as SRB are slower growing than DB. We know that DB and PRB can co-exist, but the SRB appear to have a negative impact on PRB. Therefore, having DB out-compete SRB should have a profound positive impact on the PRB.

As shown in Figure 18 for experimental set EDvSS (standing for Electron-Donor-variable Steady States), NO₃⁻ reduction was proportional to the H₂ pressure when the supply of H₂ was restricted (at the lower H₂ pressures). Denitrification was complete at a H₂ pressure of 3 atm, and SO₄²⁻ reduction began at H₂ ≥ 3.4 atm. The H₂ flux for complete denitrification and no SO₄²⁻ reduction was ~0.4 g H₂/m²-day (corresponding to a NO₃⁻ removal flux of about 1.1 gN/m²-day). Figure 19 shows the results from experimental set EAvSS (standing for Electron-Acceptor-variable Steady States), in which the H₂ availability always was sufficient. NO₃⁻ was the preferred electron acceptor, and SO₄²⁻ was reduced only when the NO₃⁻ surface loading was ≤ ~0.2 g H₂/m²-day, which corresponds to a NO₃⁻ flux of ~ 0.5 g N/m²-day.

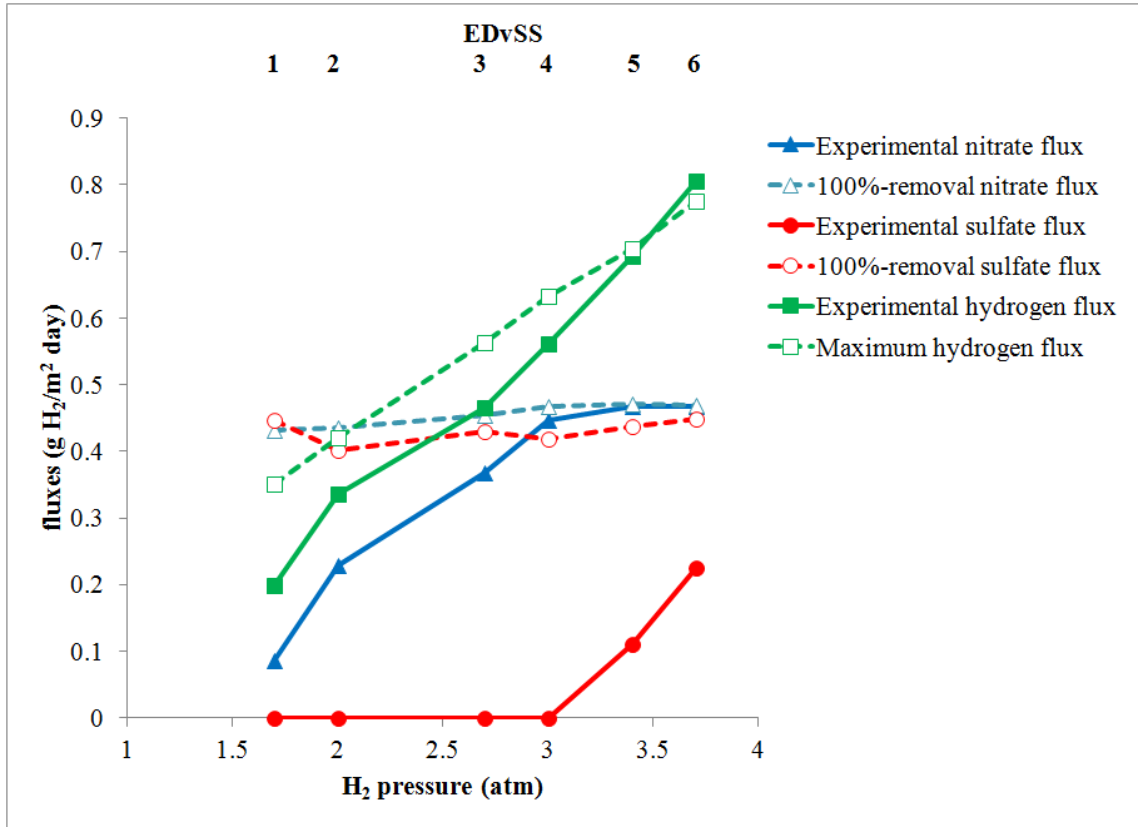


Figure 18. Removal fluxes of NO_3^- and SO_4^{2-} for the 6 steady states of EDvSS (noted at the top of the graph), 100%-reduction fluxes for these acceptors, the total H_2 removal flux for all acceptors, and the maximum-possible H_2 flux deliverable by the experimental H_2 pressure (in the range of 1.7 to 3.7 atm). All fluxes are expressed as H_2 equivalents. The H_2 flux due to O_2 reduction of $0.12 \text{ g H}_2/\text{m}^2\text{-day}$ for each EDvSS is included in the total H_2 flux. The EDvSS numbers indicate the chronological order of the experiments. The results are presented here in ascending order of ascending H_2 pressure.

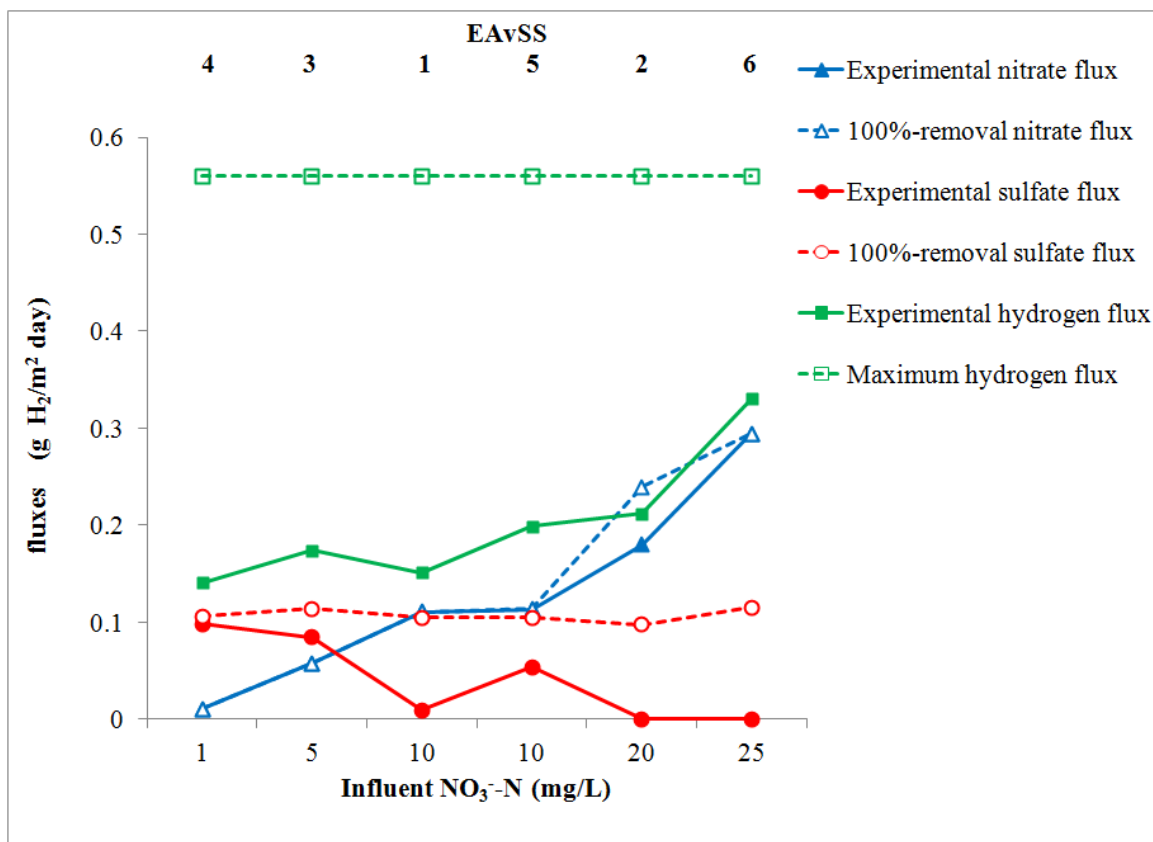


Figure 19. Removal fluxes of NO₃⁻ and SO₄²⁻ for the 6 steady states of EAvSS (indicated across the top of the graph), 100%-removal fluxes for these acceptors, the total H₂ removal flux for all acceptors, and the maximum-possible H₂ flux deliverable with a H₂ pressure of 25 psig (2.7 atm). All fluxes are expressed as H₂ equivalents. The H₂ flux due to O₂ reduction of 0.03 g H₂/m²-day for each EAvSS is included in the total H₂ flux. The EAvSS numbers indicate the chronological order of the experiments. The results are presented here in ascending order of influent NO₃⁻ concentration, and two experiments has an influent concentration of 10 mgN/L.

For biofilm samples, we assayed DB and SRB by the quantitative Polymerase Chain Reaction (qPCR) targeting the nitrite reductases and dissimilatory sulfite reductase, respectively. Figures 20 and 21 present the qPCR results. While DB and SRB increased with higher H₂ pressures when H₂ availability was limiting (Figure 20), SRB did not decline with higher NO₃⁻ removal flux when H₂ availability was not limiting (Figure 21), even when SO₄²⁻ reduction was absent. The SRB trend reflects that the SRB's metabolic diversity allowed them to remain in the biofilm whether or not they were reducing SO₄²⁻. In all scenarios tested, the SRB were able to initiate strong SO₄²⁻ reduction only when competition for H₂ inside the biofilm was relieved by nearly complete removal of NO₃⁻. Therefore, the onset of SO₄²⁻ reduction was suppressed by the presence of sufficient denitrification to out-compete SRB for H₂ and space in the biofilm.

In summary, denitrification out-competed SO_4^{2-} reduction when the H_2 flux for denitrification was $\sim 0.4 \text{ g H}_2/\text{m}^2\text{-day}$ and H_2 delivery was limiting. In this situation, SRB increased significantly when the NO_3^- removal flux was low enough to allow SO_4^{2-} reduction to begin. When H_2 delivery was not limiting, SRB were significantly present in all biofilms, and the H_2 flux due to denitrification had to be $\geq 0.2 \text{ g H}_2/\text{m}^2\text{-day}$ to suppress SO_4^{2-} reduction.

Similar trends were observed in the pilot MBfRs. With H_2 limitation, a NO_3^- flux of $0.3 \text{ g H}_2/\text{m}^2\text{-day}$ suppressed SO_4^{2-} reduction, while $0.17 \text{ g H}_2/\text{m}^2\text{-day}$ slowed SO_4^{2-} reduction when H_2 delivery was not limiting. Likewise, SRB were present in all cases, but stimulated when conditions allowed SO_4^{2-} reduction in the lag MBfR.

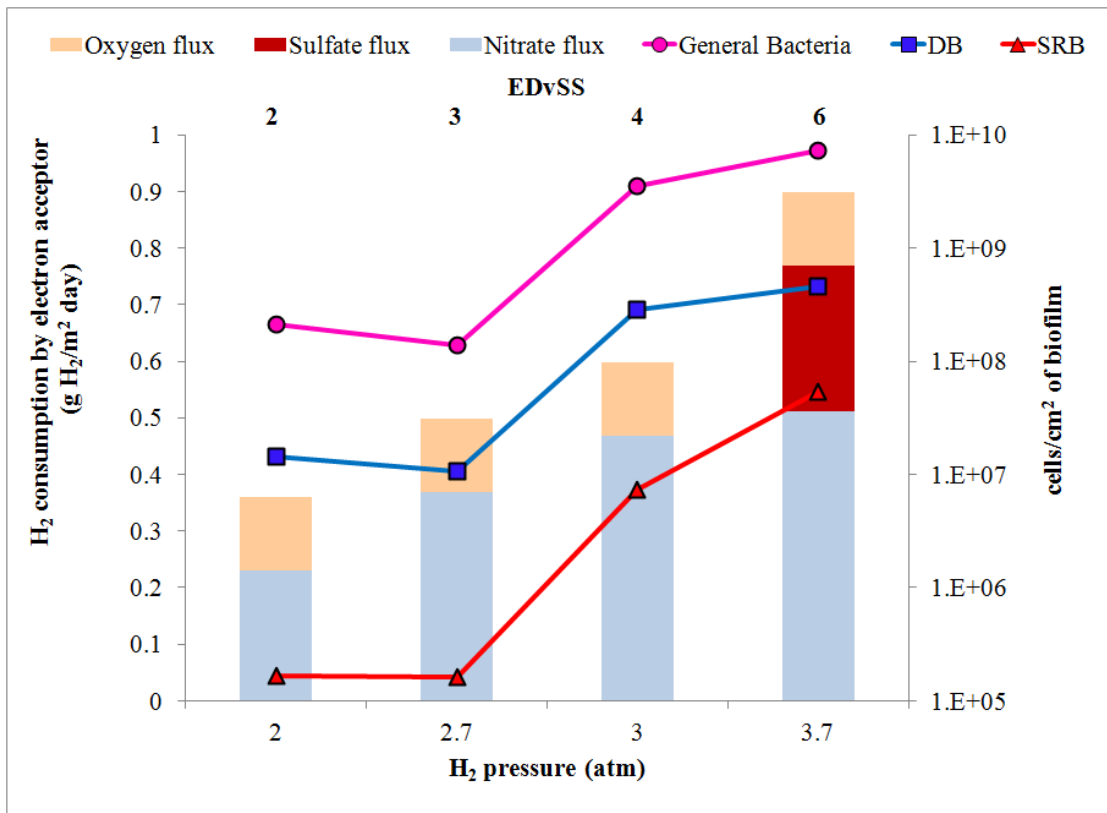


Figure 20. Abundances (in cells/cm²) of DB (sum of *nirS* and *nirK* genes), SRB, and general bacteria for four biofilm samples from EDvSS, along with the H_2 consumption rate by each electron acceptor.

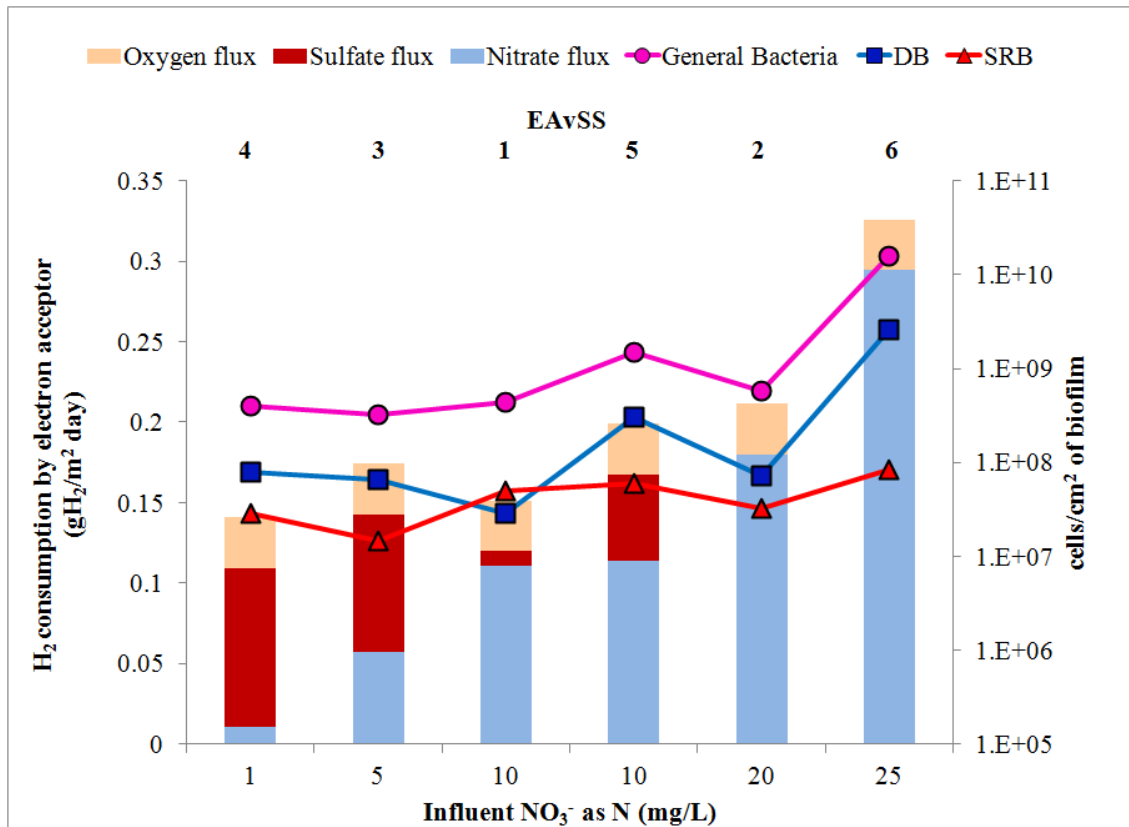


Figure 21. Abundances (in cells/cm²) of DB (sum of *nirS* and *nirK* genes), SRB, and general bacteria for six biofilm samples from EAvSS, along with the H₂ consumption rate by each electron acceptor. The EAvSS numbers indicate the chronological order of the experiments. The results are presented here in ascending order of influent NO₃⁻ concentration.

6.3 Phylogenetic analysis of DB and SRB in hydrogen-fed biofilms

Ontiveros-Valencia A, Ilhan ZE, Kang DW, Rittmann BE, Krajmalnik-Brown R (2013a) Phylogenetic analysis of nitrate- and sulfate-reducing bacteria in a hydrogen-fed biofilm *FEMS Microbial Ecology*, 85: 158-167.

Using pyrosequencing analysis, we studied the ecological interactions between DB and SRB in the MBfRs from the study in the previous section (Ontiveros-Valencia et al., 2012). We achieved a comprehensive understanding of the microbial community structure and function by employing two MBfR: one with changes to electron donor availability (called EDvSS) and the other with different electron acceptor (NO₃⁻) surface loadings (called EAvSS).

In EDvSS and with severe electron-donor limitation (samples 1a and 1b in Figure 22), the biofilm community was dominated by heterotrophic DB (i.e., *Burkholderiales*); when the limitation on H₂ decreased, the biofilm became more autotrophic, with DB-phylotypes closely related to *Rhodocyclales* and *Hydrogenophilales* dominating the biofilm community (samples 1c and 1d in Figure 20). In EAvSS and without donor limitation, the biofilm community was dominated by autotrophic DB; however, a decrease of NO₃⁻ loading allowed SRB (mostly *Desulfovibrionales*) to compete better for space in the biofilm. *Bacteroidales* were associated

with strong SO_4^{2-} reduction activity (samples 1d for EDvSS, and 2c, 2d for EAvSS) as they likely consumed soluble microbial products released by SRB.

Principal coordinate analysis (PCoA, not shown) and UniFrac analysis (Figure 23) pointed out that electron-donor availability and electron-acceptor surface loading framed the microbial community, with restricted electron-donor availability significantly decreasing the microbial diversity of the biofilm. The onset of SO_4^{2-} reduction led the biofilm communities of EDvSS and EAvSS to cluster together (sample 1d for EDvSS and all samples from EAvSS) (Figure 23), showing the importance of SO_4^{2-} reduction in determining community structure.

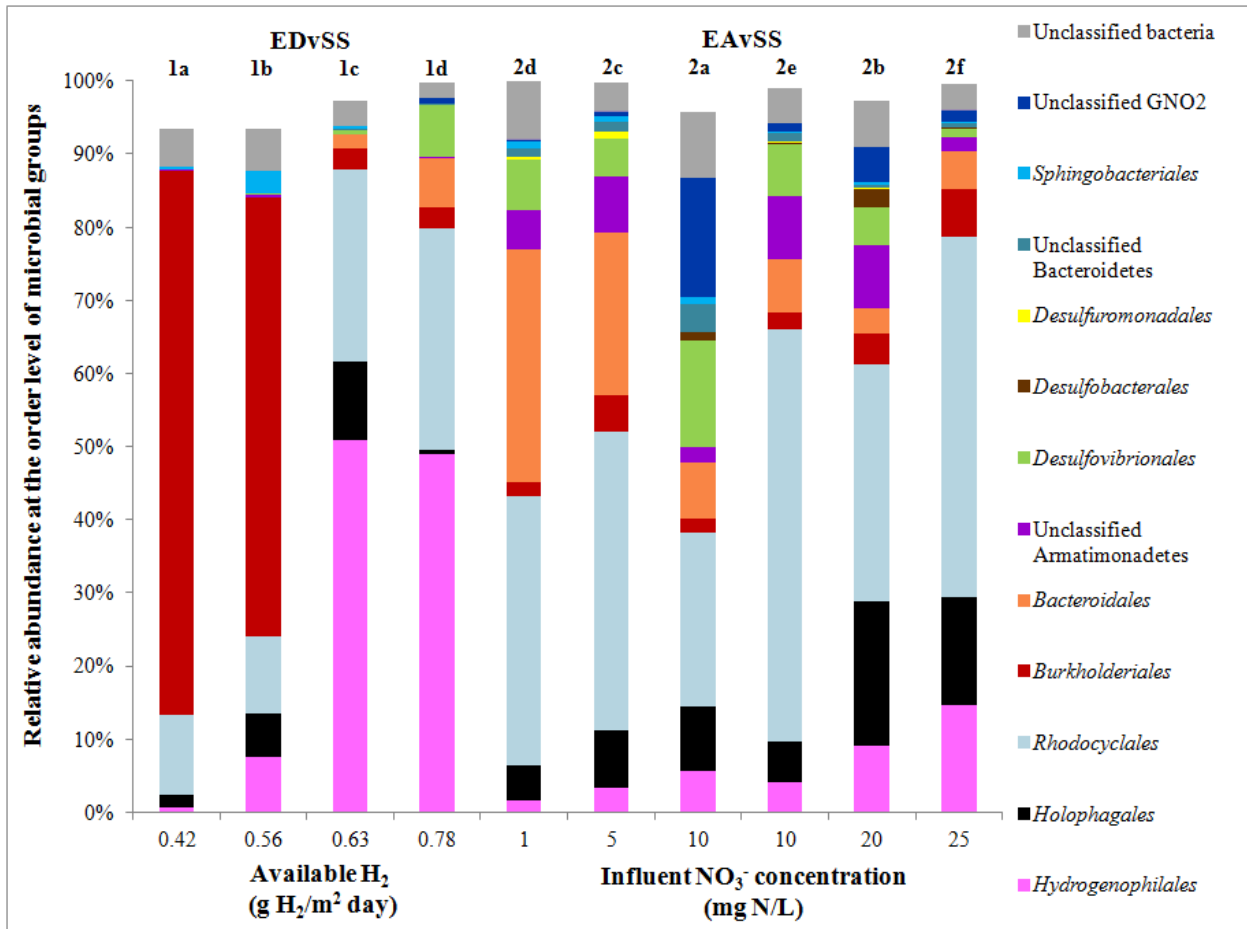


Figure 22. Relative abundances of the most abundant microbial phylotypes at the order level for EDvSS and EAvSS. The EDvSS and EAvSS letter and number codes show the chronological order of samples. Samples for EAvSS are shown according to increasing NO_3^- concentration. The sum does not add up to 100% in all cases because minor phylotypes are not shown.

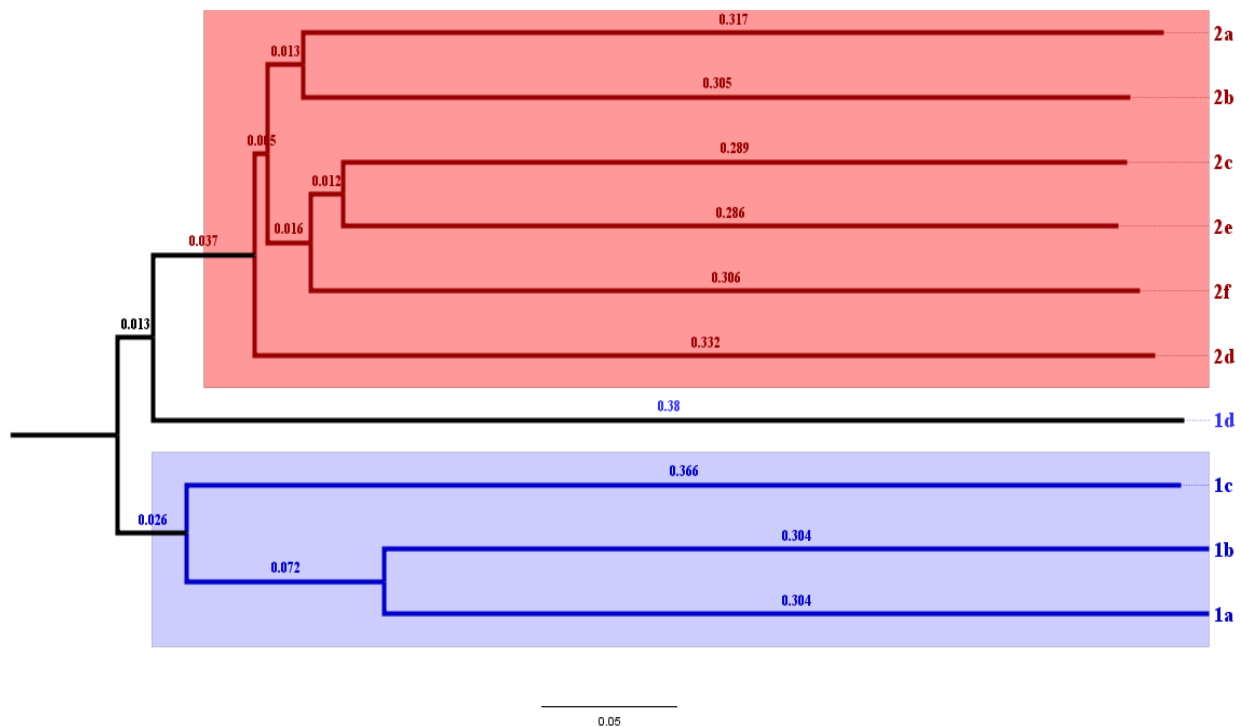


Figure 23. Clustering based on the unweighted UniFrac analysis. The branch length represents the distance between biofilm samples in UniFrac units, as indicated by the scale bar. 1a-1d correspond to EDvSS, with 1a = 0.42 g H₂/m² day, 1b = 0.56 g H₂/m² day, 1c = 0.63 g H₂/m² day, and 1d = 0.78 g H₂/m² day. 2a-2f correspond to EA vSS, with 2a = 10 mg N/L, 2b = 20 mg N/L, 2c = 5 mg N/L, 2d = 1 mg N/L, 2e = 10 mg N/L, and 2f = 25 mg N/L.

6.4 Interactions Between DB and PRB in a H₂-Based Biofilm

Zhao, H. P., Van Ginkel, S., Tang, Y., Kang, D.-W., Rittmann, B. E., and Krajmalnik-Brown, R. (2011) Interactions between perchlorate and nitrate reductions in the biofilm of a hydrogen-based membrane biofilm reactor. *Environ. Sci. Technol.* 45: 10155-10162.

We studied the direct functional and structural interactions between NO₃⁻ and ClO₄⁻ reductions in the H₂-based MBfR. We utilized qPCR directed toward the nitrate and perchlorate reductase genes, as well a high-throughput pyrosequencing. Figure 24 presents the H₂ fluxes and qPCR results according to the electron acceptor. Figure 25 summarizes the predominant genera according to high-throughput pyrosequencing.

When H₂ delivery was not limiting (especially Steady States 1 and 4, based on H₂ permeability of the polypropylene fiber (Tang et al., 2012)), ClO₄⁻ and NO₃⁻ reductions were complete (not shown), and the MBfR's biofilm was composed mainly of bacteria from the \square and β -*proteobacteria* classes, with autotrophic genera *Sulfuricurvum*, *Hydrogenophaga*, and *Dechloromonas* dominating the biofilm. Based on functional-gene and pyrosequencing assays, *Dechloromonas* played the most important role in ClO₄⁻ reduction, while *Sulfuricurvum* (an autotrophic denitrifier) and *Hydrogenophaga* were responsible for NO₃⁻ reduction.

When H₂ delivery was insufficient to completely reduce both electron acceptors (especially Stages 5 and 6, when the H₂ flux was ≥ 0.22 g H₂/m²-day), NO₃⁻ reduction out-competed ClO₄⁻ reduction for electrons from H₂, and mixotrophs (i.e., bacteria that can use H₂ or organics as the electron donor) became important in the MBfR biofilm. Under H₂ limiting conditions in steady state 5 and 6, β -*proteobacteria* became the dominant class: *Azonexus* and *Hydrogenophaga* (mixotrophs) replaced *Sulfuricurvum* (an autotrophic denitrifier) as a main genus.

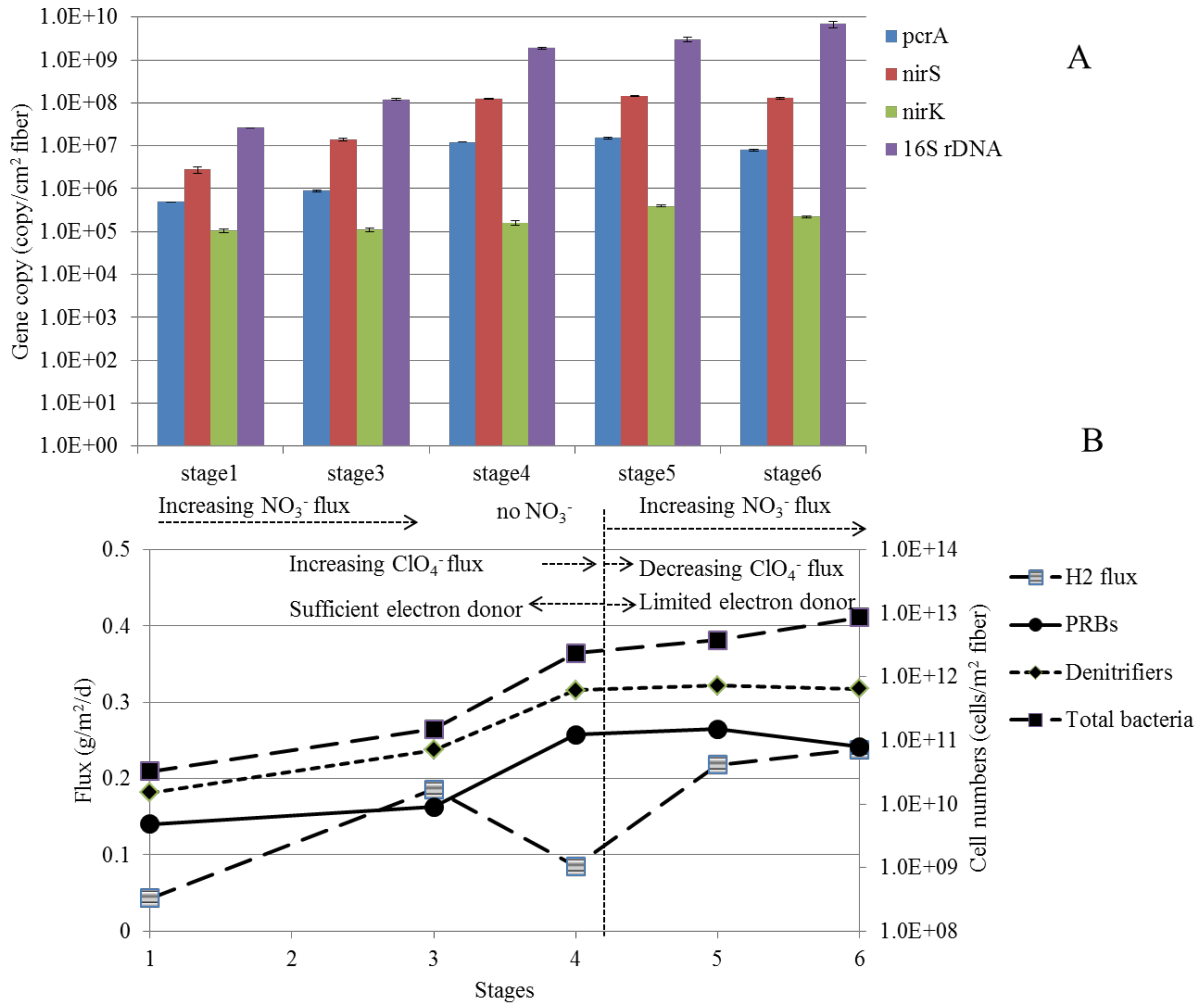


Figure 24. (A) *pcrA*, *nirK*, *nirS*, and 16S rRNA gene copy numbers per cm² fiber for, respectively, PRB, DB, DB, and general bacteria. (B) Estimated cells densities associated with the total flux of H₂. The vertical dashed line distinguishes no limitation from H₂ delivery (stages 1 – 4) from limitation from H₂ delivery in stages 5 and 6.

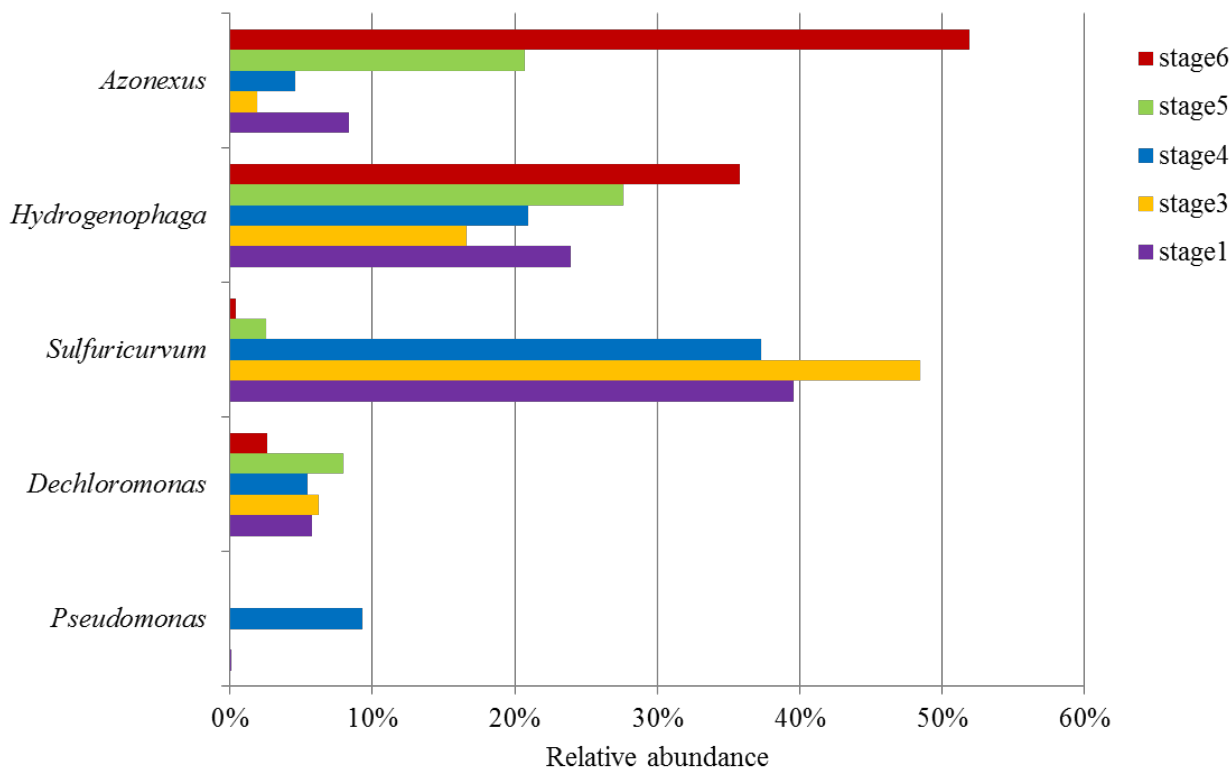


Figure 25. Predominant bacterial genera by relative abundance (%) in the MBfR biofilms.

The community differences suggest that mixotrophic NO_3^- -reducing bacteria had advantages over strict autotrophs when H_2 was limiting, because organic microbial products became important electron donors when H_2 was severely limiting. In this case, DB had an advantage over PRB (such as *Dechloromonas*), and ClO_4^- reduction was suppressed. This result underscores the value of identifying specific PRB, as well as the general presence of PRB using qPCR. While *Dechloromonas* is a prominent and apparently effective PRB, other PRB may be present instead of or along with *Dechloromonas*, especially when H_2 delivery is limited. Further investigations into the characteristics of the different PRB seem justified.

6.5 Competition Among Perchlorate, Nitrate, and Sulfate Reductions

Zhao, H. P., Z.-E. Ilhan, A. Ontiveros-Valencia, B. E. Rittmann, and R. Krajmalnik-Brown (2013b). Interactions among multiple electron acceptors and their effects on the microbial ecology in a hydrogen-based biofilm. *Environ. Sci. Technol.*, 47: 7396-4703.

To investigate interactions among multiple electron acceptors in a H_2 -fed biofilm, we operated an MBfR with H_2 -delivery capacity sufficient to reduce all acceptors. The research goal was to study the interactions among the reductions of the multiple electron acceptors when the practical goal is to obtain a very low effluent concentration of ClO_4^- . In particular, we

sought to understand if any fundamental ecological or kinetic phenomena were preventing full ClO_4^- reduction in the presence of the other acceptors. Based on H_2 permeabilities with the composite fibers (Tang et al., 2012), we carried out all experiments with sufficient H_2 -delivery capacity. ClO_4^- and O_2 were input electron acceptors in all stages at surface loadings of $0.08 \pm 0.006 \text{ g/m}^2\text{-d}$ ($10 \pm 0.7 \text{ e}^- \text{ meq/m}^2\text{-d}$) for ClO_4^- and $0.51 \text{ g/m}^2\text{-d}$ ($76 \text{ e}^- \text{ meq/m}^2\text{-d}$) for O_2 . SO_4^{2-} was added in Stage 2 at $3.77 \pm 0.39 \text{ g/m}^2\text{-d}$ ($331 \pm 34 \text{ e}^- \text{ meq/m}^2\text{-d}$), and NO_3^- was further added in Stage 3 at $0.72 \pm 0.03 \text{ g N/m}^2\text{-d}$ ($312 \pm 13 \text{ e}^- \text{ meq/m}^2\text{-d}$).

As summarized in Figure 26, ClO_4^- , O_2 , and NO_3^- (when present in the influent) were completely reduced at steady state for each stage; measured SO_4^{2-} reduction decreased from $78 \pm 4\%$ in Stage 2 to $59 \pm 4\%$ in Stage 3, when NO_3^- was present. Thus, we found no intrinsic barrier to full ClO_4^- reduction when NO_3^- and SO_4^{2-} were being reduced in parallel. Based on qPCR targeting the reductase genes (not shown), PRB remained stable throughout, although SRB became dominant when a high concentration of SO_4^{2-} was added.

While perchlorate-reducing bacteria (PRB), assayed by qPCR targeting the *pcrA* gene (not shown), remained stable throughout, sulfate-reducing bacteria (SRB), assayed by the *dsrA* gene, became dominant (35% of total bacteria, TB) when a high concentration of SO_4^{2-} was added. Denitrifying bacteria (DB), assayed by the *nirK* and *nirS* genes, became dominant (54% of TB) in Stage 3, but SRB remained important (13% of TB).

Figure 27 shows pyrosequencing results of the communities. *β -Proteobacteria* dominated in Stage 1, but *ϵ -Proteobacteria* became more important in Stages 2 and 3, when the input of multiple electron acceptors favored genera with broader electron-accepting capabilities. *Sulfuricurvum* (a sulfur oxidizer and NO_3^- reducer) and *Desulfovibrio* (a SO_4^{2-} reducer) become dominant in Stage 3, suggesting redox cycling of sulfur in the biofilm. Redox cycling probably involved SO_4^{2-} reduction to elemental sulfur (S°) and sulfide (S^{2-}) by SRB and S° oxidation by *Sulfuricurvum*.

In summary, we demonstrated that it was possible to achieve $\mu\text{g/L}$ concentrations of ClO_4^- in parallel to reductions of NO_3^- and SO_4^{2-} . The NO_3^- flux was $0.25 \text{ g H}_2/\text{m}^2\text{-day}$, the $\text{NO}_3^- + \text{O}_2 + \text{ClO}_4^-$ flux was $0.34 \text{ g H}_2/\text{m}^2\text{-day}$, the SO_4^{2-} flux was as high as $0.25 \text{ g H}_2/\text{m}^2\text{-day}$, and the total H_2 flux (up to $0.59 \text{ g H}_2/\text{m}^2\text{-day}$) was less than the H_2 -delivery capacity of the composite fibers. *Dechloromonas* appeared to be the main PRB, and having multiple electron donors present favored the genera with broader electron-accepting capabilities (e.g., *Sulfuricurvum* and *Dechloromonas*) in Stage 3.

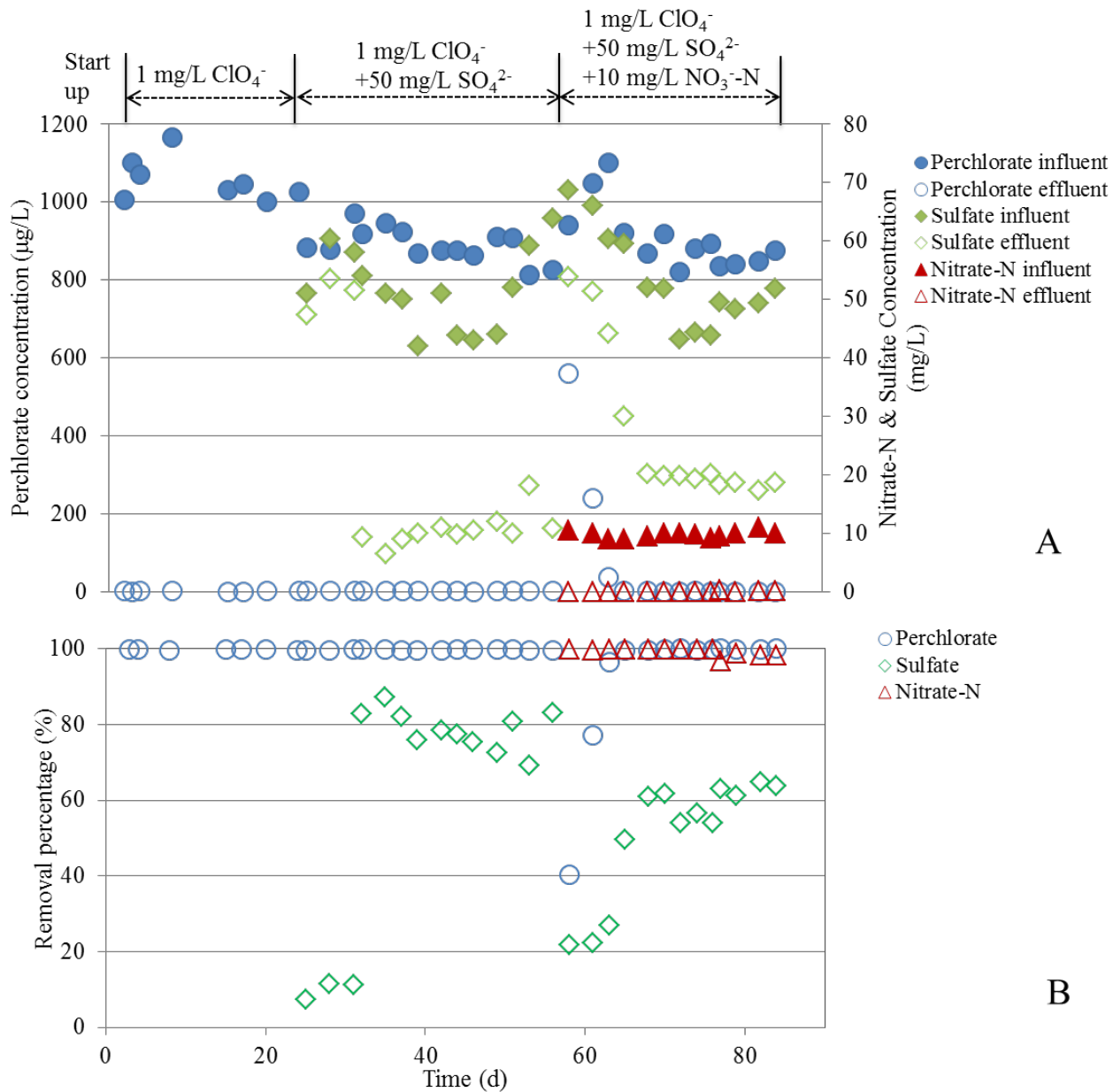
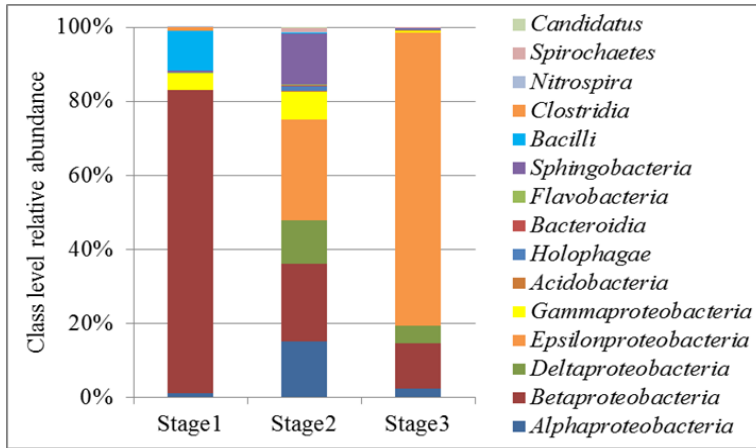
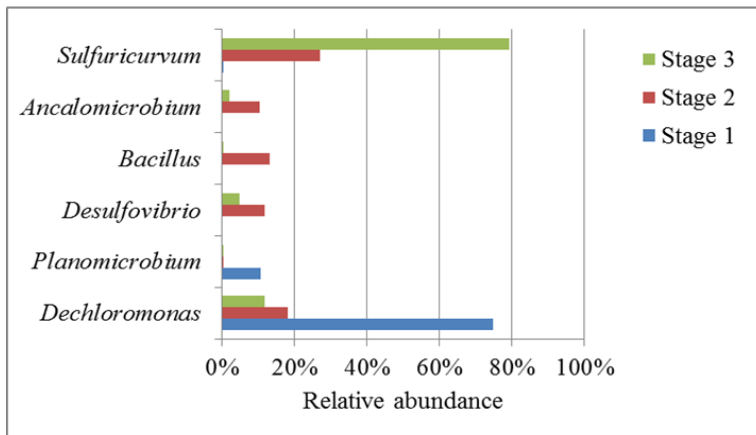


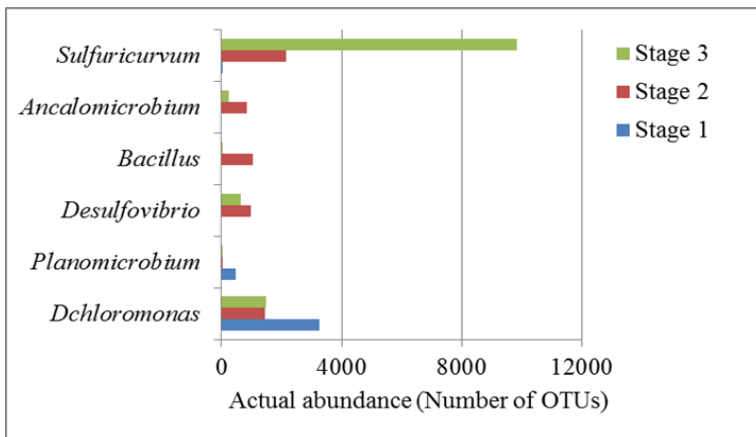
Figure 26. (A) Perchlorate, sulfate, and nitrate concentrations in the MBfR. (B) Perchlorate, sulfate and nitrate removal percentages.



A



B



C

Figure 27. (A) Class-level abundances based on pyrosequencing from the MBfR biofilms (X stands for unclassified by class). (B) Relative abundance (%) of the predominant bacterial genera in the MBfR biofilms. (C) Actual abundance (Number of OTUs) of the predominant bacterial genera in the MBfR biofilms. (Sequences that are 5% or less divergent to each other were combined as one OTU.)

6.6 Two-Stage MBfR to Achieve Full Perchlorate Reduction with Rialto's Groundwater

Zhao, H.-P., A. Ontiveros-Valencia, Y. Tang, B.-O. Kim, Z.-E. Ilhan, R. Krajmalnik-Browh, and B. E. Rittmann (2013a). Using a two-stage hydrogen-based membrane biofilm reactor (MBfR) to achieve complete perchlorate reduction in the presence of nitrate and sulfate. *Environ. Sci. Technol.* **47**: 1565 – 1572.

This work evaluated a two-stage strategy for achieving complete reduction of ClO_4^- without SO_4^{2-} reduction in a H_2 -based MBfR treating the Rialto groundwater, in which NO_3^- and SO_4^{2-} are present in much higher concentrations than ClO_4^- . This study was set up specifically to help understand why the field results did not show full ClO_4^- reduction and to find ways to overcome the roadblock to full ClO_4^- reduction. Furthermore, our preliminary results with one stage-treatment did not lead to full ClO_4^- reduction in a bench-scale MBfR treating a groundwater having 10 mg/L ClO_4^- (Ontiveros-Valencia et al., 2013b).

As shown in Figures 28 and 29, we achieved full ClO_4^- reduction in the Rialto groundwater (i.e., in the presence of much higher concentrations of SO_4^{2-} and NO_3^-) by using a two-stage MBfR with controlled $\text{NO}_3^- + \text{O}_2$ surface loadings and polypropylene fibers. With a $\text{NO}_3^- + \text{O}_2$ surface loading larger than 0.6 g N/m²-d (0.21 g H_2 /m²-day), the lead MBfR removed about 80% of NO_3^- and 30% of ClO_4^- . This decreased the surface loading of $\text{NO}_3^- + \text{O}_2$ to 0.3–0.5 g N/m²-d (0.11 – 0.18 g H_2 /m²-day) for the lag MBfR, in which ClO_4^- was reduced to non-detectable concentrations. SO_4^{2-} reduction also was eliminated without compromising full ClO_4^- reduction using a higher flow rate that gave a $\text{NO}_3^- + \text{O}_2$ surface loading of 0.94 g N/m²-d (0.34 g H_2 /m²-day) in the lead MBfR and 0.53 g N/m²-d (0.18 g H_2 /m²-day) in the lag MBfR.

Results from qPCR (not shown) and pyrosequencing (Figure 30) show that the lead and lag MBfRs had distinctly different microbial communities. DB, quantified using the *nirS* and *nirK* genes, dominated the biofilm in the lead MBfR, but PRB, quantified using the *pcrA* gene, became more important in the lag MBfR. The facultative anaerobic bacteria *Dechloromonas*, *Rubrivivax*, and *Enterobacter* were dominant genera in the lead MBfR, where their main function was to reduce NO_3^- . With a modest NO_3^- surface loading and full ClO_4^- reduction, the dominant genera shifted to *Sphaerotilus*, *Rhodocyclaceae*, and *Rhodobacter* in the lag MBfR. *Dechloromonas* was present in the lag MBfR, but not dominant. The difference in community structures probably was related to the fact that the lead and lag positions were not switched. For the pilot MBfRs, the microbial communities were similar for the lead and lag MBfRs, probably due to regular switching. Another difference is that the influent to the lag MBfR in our study was oxygenated.

These results show that it was possible to obtain essentially 100% reduction of ClO_4^- treating the Rialto groundwater when the electron-acceptor surface loadings were properly managed: lag-MBfR's $\text{NO}_3^- + \text{O}_2$ loading $\leq \sim 0.5$ g N/m²-day, or 0.18 g H_2 /m²-day. Furthermore, it was possible to attain this good result without incurring SO_4^{2-} reduction with the $\text{NO}_3^- + \text{O}_2$ loading ≥ 0.18 g H_2 /m²-day to the lag MBfR. Finally, it was not necessary to have the

biofilm dominated by *Dechloromonas* to achieve complete ClO_4^- reduction in the lag MBfR. These findings suggest that an “ideal” $\text{NO}_3^- + \text{O}_2$ loading to a lag MBfR is $\sim 0.18 \text{ g H}_2/\text{m}^2\text{-day}$ to suppress SO_4^{2-} reduction while encouraging ClO_4^- reduction. In this study, the $\text{NO}_3^- + \text{O}_2$ surface loading was controlled by O_2 , since the lead MBfR removed most of the NO_3^- . This illustrates the value of using O_2 addition to the second stage, a practice not utilized for the field study.

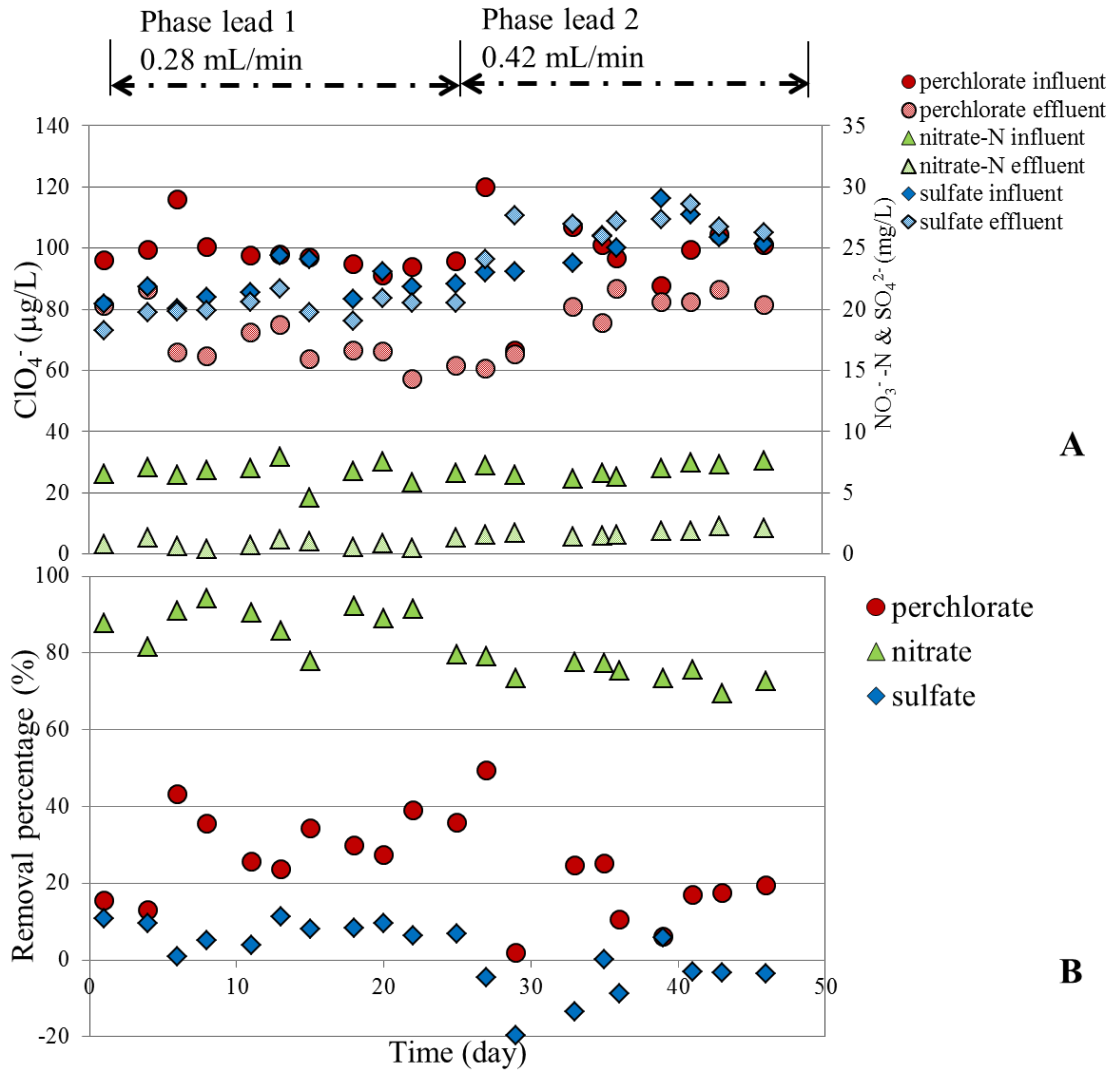


Figure 28. Concentrations and removals of NO_3^- , ClO_4^- , and SO_4^{2-} in the lead MBfR.

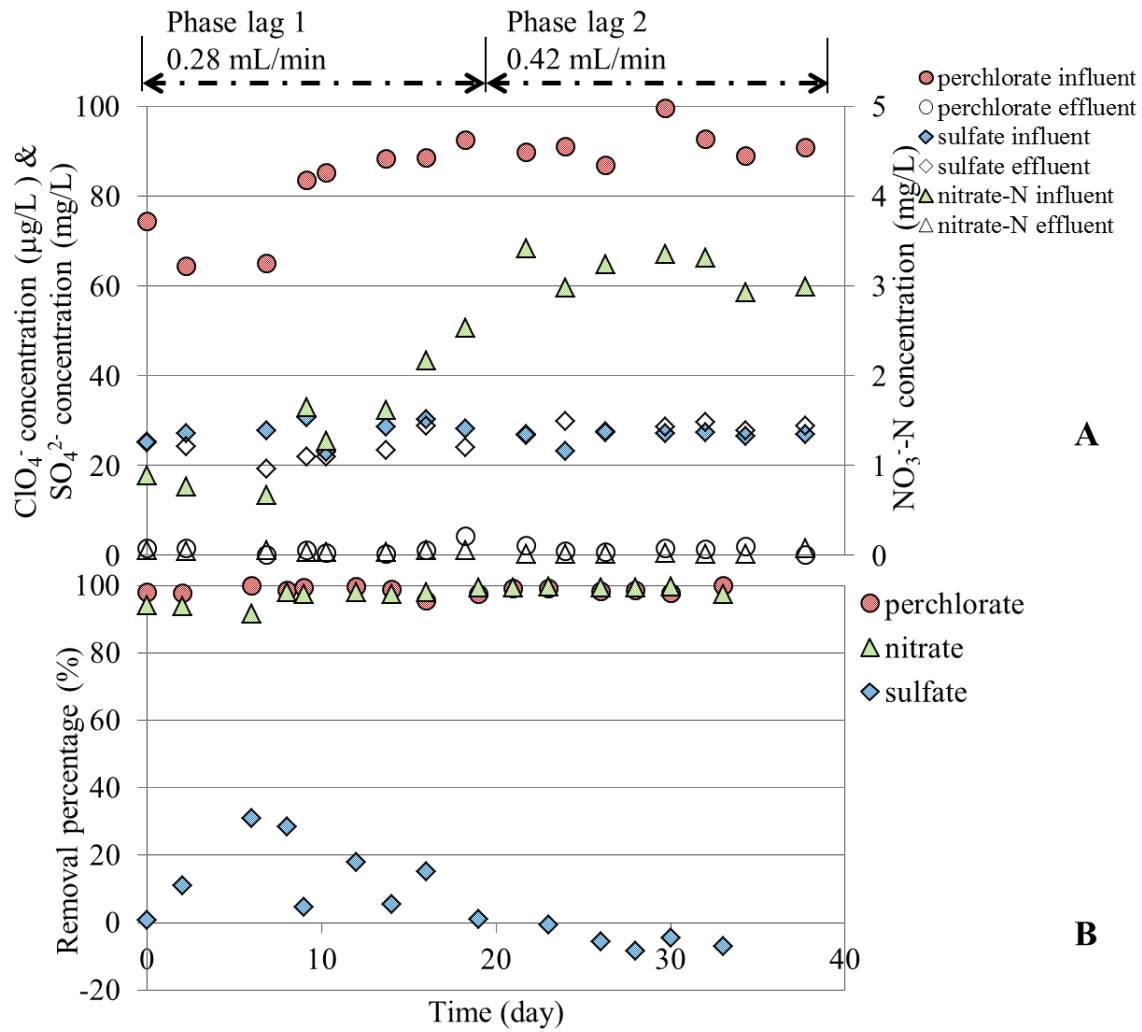
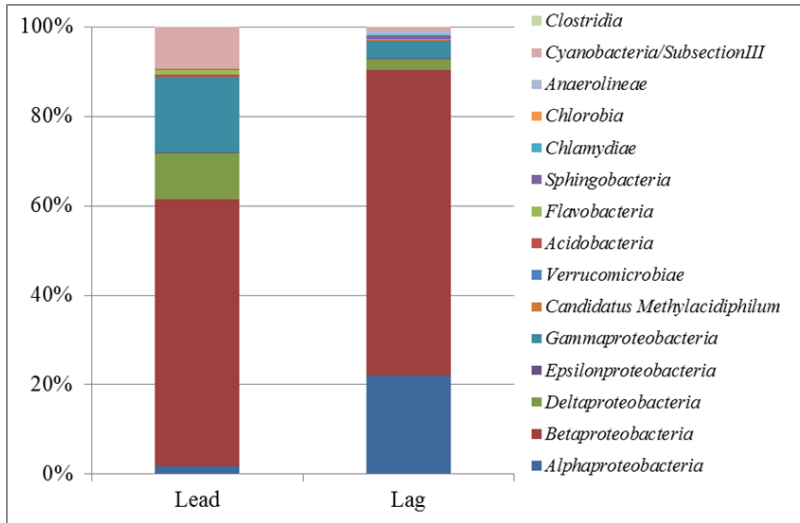
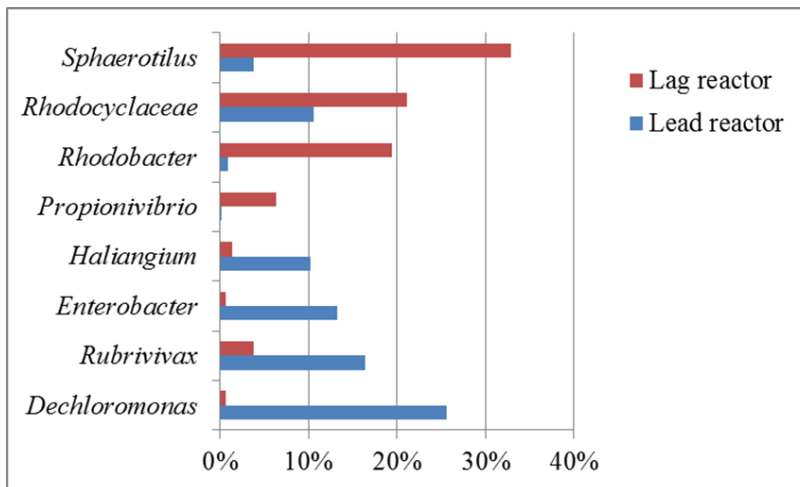


Figure 29. Concentrations and removals of NO_3^- , ClO_4^- , and SO_4^{2-} in the lag MBfR.



A



B

Figure 30. Microbial community structure in the MBfRs for steady state at the flow rate of 0.28 mL/min. The top panel is the distribution of bacteria at the class level. The bottom panel is the distribution of the most common genera.

Chapter 7. Exploring Mechanisms and Performance with Mechanistic Modeling

In parallel to the bench-scale experiments, the ASU team developed and applied a series of mechanistic mathematical models. The primary objective of the mathematical modeling was to integrate and quantify the many ecological, kinetic, and transport mechanisms occurring when H_2 is delivered to a biofilm of bacteria exposed to multiple electron acceptors. We developed two models having different combinations of electron acceptors, but a common framework. One model described NO_3^- and ClO_4^- reductions occurring in a H_2 -based biofilm. The second model represented NO_3^- and SO_4^{2-} reductions. The models were published in three manuscripts that are summarized in this section.

7.1 Developing the Multi-Species Model for a H_2 -Based Biofilm Able to Do NO_3^- and ClO_4^- Reductions

Tang, Y, H. P., Zhao, A. K. Marcus, and B. E. Rittmann (2012c). A steady-state biofilm model for simultaneous reduction of nitrate and perchlorate -- Part 1: model development and numerical solution. *Environ. Sci. Technol.* **46**: 1598 – 1607.

We developed a multispecies biofilm model for simultaneous reduction of NO_3^- and ClO_4^- in the biofilm of a H_2 -based MBfR. The one-dimension model includes dual-substrate Monod kinetics for a steady-state biofilm with five solid and five dissolved components. The solid components are autotrophic DB, autotrophic PRB, heterotrophic bacteria (HB), inert biomass (IB), and EPS. The dissolved components are NO_3^- , ClO_4^- , H_2 , substrate-utilization-associated products (UAP), and biomass-associated products (BAP). The structure of the model is illustrated in Figure 31.

The model explicitly considers four mechanisms involved in how three controllable operating conditions (H_2 pressure, NO_3^- loading, and ClO_4^- loading) affect NO_3^- and ClO_4^- removals: 1) competition for H_2 , 2) promotion of PRB (such as *Dechloromonas*) due to having two electron acceptors (NO_3^- and ClO_4^-), 3) competition between NO_3^- and ClO_4^- reductions for the same resources in the biofilm (electrons and enzymes), and 4) competition for space in the biofilm. Two other special features of the model are having H_2 delivered from the membrane substratum and solving directly for steady state using a novel three-step approach: finite-difference for approximating partial differential and/or integral equations, Newton-Raphson for solving non-linear equations, and an iterative scheme to obtain the steady-state biofilm thickness.

An example result illustrates the model's features. Figure 32 presents profiles of the five soluble components and distributions of the five solid components in the biofilm, which has a thickness of 55 μm at steady state for this example. The NO_3^- and ClO_4^- concentrations are higher on the liquid side, while the H_2 concentration is higher on the membrane side, but essentially zero on the liquid side. The latter demonstrates that H_2 delivery is limiting inside the biofilm. Because UAP and BAP are produced in the biofilm and diffuse into the liquid,

their concentrations are higher on the membrane side. Competition for space and H_2 results in non-uniform biomass distributions inside the biofilm. The fraction of DB and PRB are higher on the membrane side, because H_2 is limiting and depleted before the outside of the biofilm. In this example, the fraction of PRB is much higher than that of DB; this is due to relatively low nitrate and perchlorate concentrations in the biofilm. Low NO_3^- and ClO_4^- concentrations mean weak competition for a common enzyme and for electrons from H_2 in PRB; thus, PRB can grow faster than DB, since PRB can use nitrate and perchlorate for growth. This promotion effect allows PRB to outcompete DB for H_2 and space in the biofilm.

Consistent with our measurements from the side reactors of the field pilots, EPS comprised the largest fraction of the biomass, up to 50% near the membrane. According to the model, EPS are higher on the membrane side, since most EPS are produced by DB and PRB. HB also are significant (up to 24%), and they are higher on the liquid side of the biofilm, because competition from DB and PRB is lessened due to depleted H_2 . IB is a low fraction (< 7%), but is denser near the outer surface, where H_2 is depleted so that competition from DB and PRB is lessened.

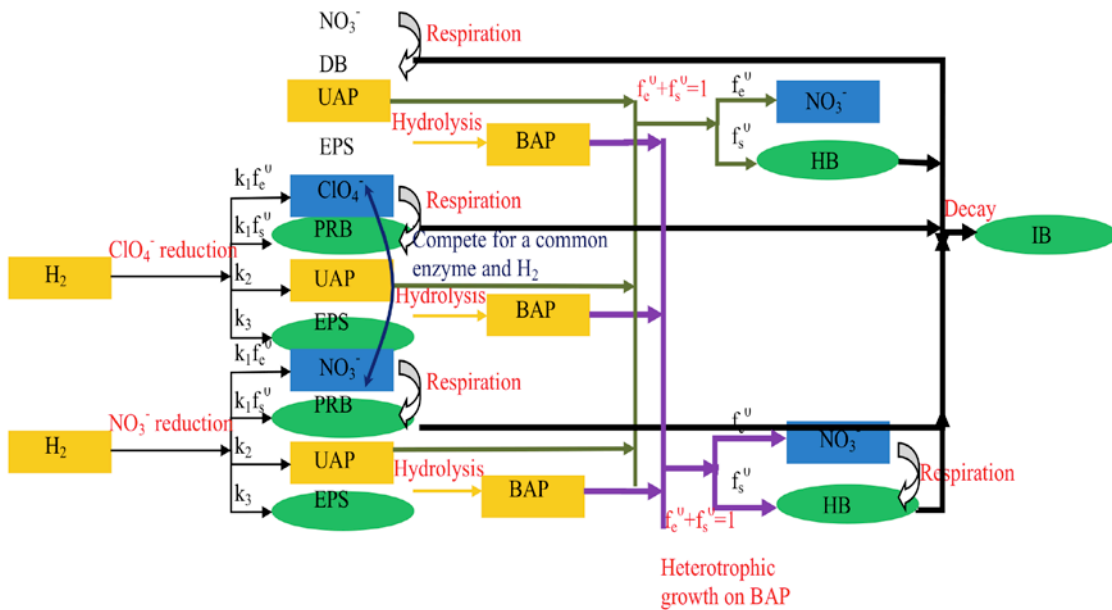
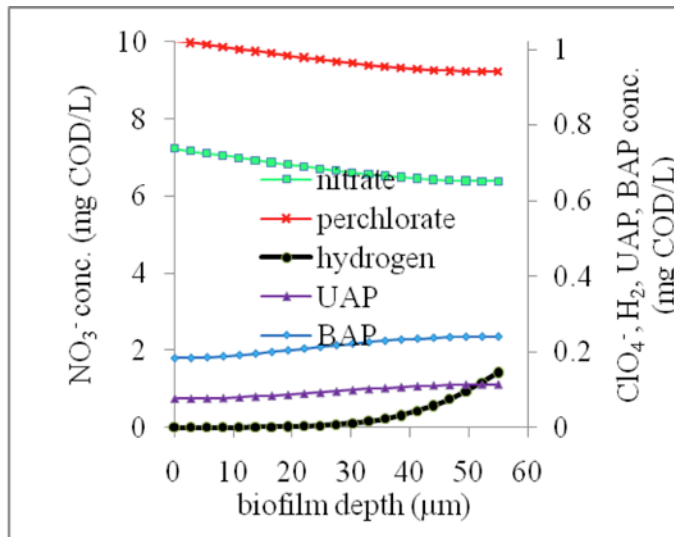
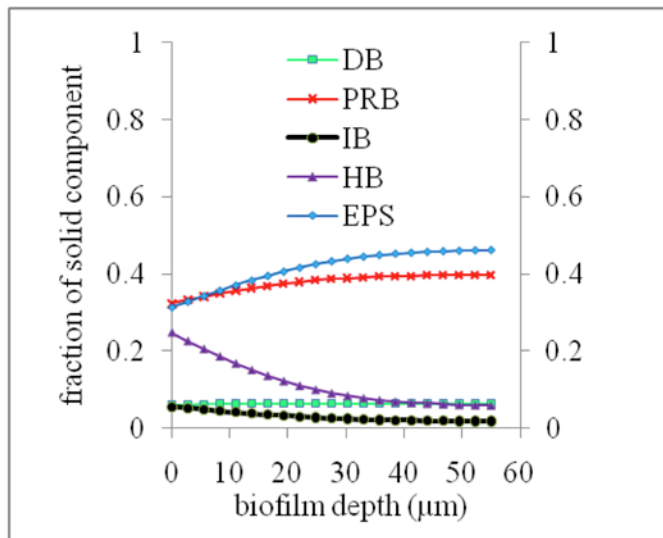


Figure 31. Schematic describing how the dissolved components (rectangles) and solid components (ellipses) interact.



a.



b.

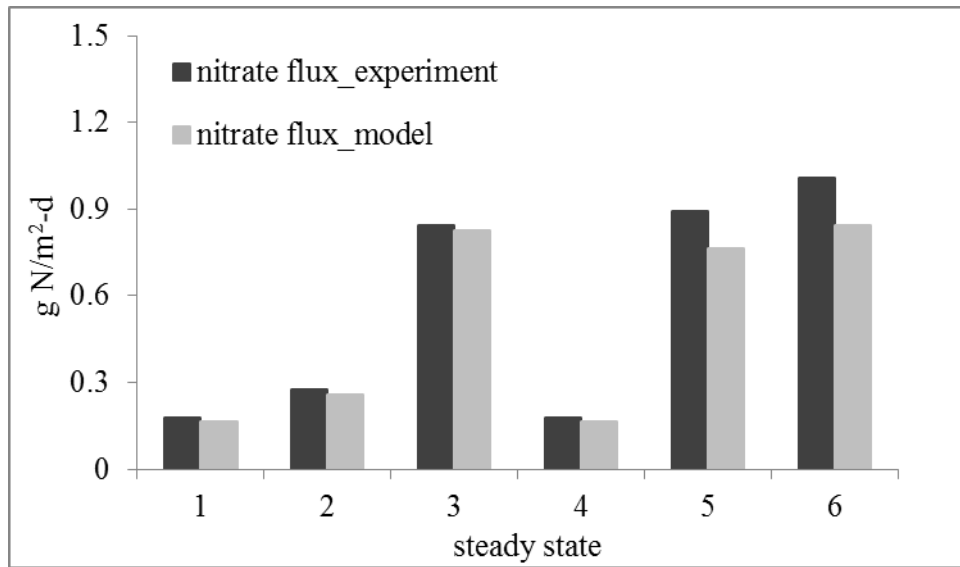
Figure 32. Substrate profiles and biomass distributions in the example. The liquid is to the left, and the membrane is to the right. The thickness of the biofilm is shown by the extent of the symbols to the right.

7.2 Application of the NO_3^- and ClO_4^- Model to MBfR Performance

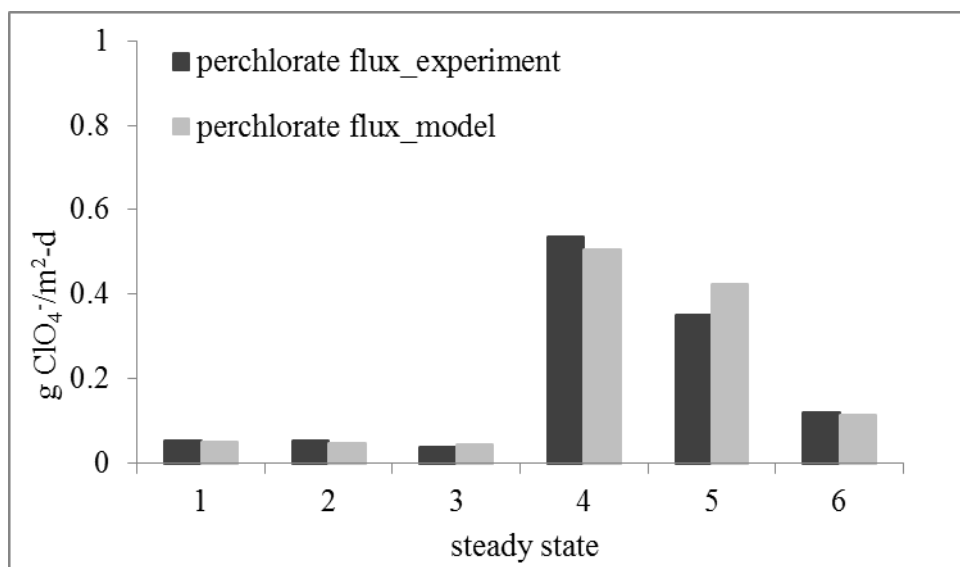
Tang, Y., H. P., Zhao, A. K. Marcus, R. Krajmalnik-Brown, and B. E. Rittmann (2012d). A steady-state biofilm model for simultaneous reduction of nitrate and perchlorate -- Part 2: parameter optimization and results and discussion. *Environ. Sci. Technol.* **46**: 1608 – 1615.

Part 1 developed a steady-state, multispecies biofilm model for simultaneous reductions of NO_3^- and ClO_4^- in the H_2 -based MBfR and presented a novel method to solve it. In Part 2, we optimize the half-maximum-rate concentrations and inhibition coefficients of NO_3^- and ClO_4^- by fitting data from experiments with different combinations of influent NO_3^- and ClO_4^- concentrations. Figure 33 compares the model-generated and experimental values (from the bench-scale studies of Zhao et al. (2011) (reported above)) for NO_3^- and ClO_4^- fluxes, along with the optimized parameter values. The model accurately captured the experimental trends for steady states that had high versus low fluxes of NO_3^- and ClO_4^- .

We next used the model with optimized parameters to quantitatively and systematically explain how three important operating conditions (NO_3^- loading, ClO_4^- loading, and H_2 pressure) affect NO_3^- and ClO_4^- reductions and biomass distributions in the biofilm. ClO_4^- reduction and accumulation of PRB in the biofilm are affected by four promotion or inhibition mechanisms: (1) simultaneous use of NO_3^- and ClO_4^- by PRB, and competition for (2) H_2 , (3) the same enzymes in PRB, and (4) space in a biofilm. Table 4 summarizes the patterns identified by the model. For the H_2 pressure evaluated experimentally, a low NO_3^- loading ($< 0.1 \text{ g N/m}^2\text{-day}$, or $< 0.036 \text{ g H}_2\text{/m}^2\text{-day}$) slightly promotes ClO_4^- removal, because of the beneficial effect from PRB using both acceptors. However, a NO_3^- loading $> 0.6 \text{ g N/m}^2\text{-day}$ ($0.21 \text{ g H}_2\text{/m}^2\text{-day}$) begins to inhibit ClO_4^- removal, as the competition effects become dominant. Therefore, the NO_3^- loading needs to be held below about $0.2 \text{ g H}_2\text{/m}^2\text{-day}$ to make excellent ClO_4^- reduction feasible. This result is coincident with the two-stage bench-scale results of Zhao et al. (presented above). The field pilot had fluxes of $0.02 - 0.18 \text{ g H}_2\text{/m}^2\text{-day}$ in the lag MBfR, but it differed from the bench-scale study in that the lead and lag MBfRs were switched in the field study, the lag MBfR had SO_4^{2-} reduction, and dissolved oxygen was introduced to the lag reactor in the laboratory study.



a.



b.

Figure 33. Comparison of fluxes of NO_3^- and ClO_4^- from the experiments and from the model with optimized parameters ($K_1 = K_{21} = 0.2 \text{ mg N/L}$ and $K_{22} = 0.8 \text{ mg ClO}_4^- /\text{L}$).

Table 4 The Mechanistic Effects of Nitrate Loading on PRB and Perchlorate Removal

Nitrate-Loading Situation	Promotion Mechanism	Inhibition Mechanisms			Net Effect
		2 Using NO ₃ ⁻ and ClO ₄ ⁻ as electron acceptors	3 Competition for the same resources within PRB	1 Competition for H ₂	
1 < 0.1 g N/m ² -day (< 0.036 g H ₂ /m ² -day)	+	+	No	+	promotion
2 0.1-0.6 g N/m ² -d (0.036-0.22 g H ₂ /m ² -day)	++	++	No	++	no effect
3 0.6-1.0 g N/m ² -d (0.22-0.36 g H ₂ /m ² -day)	+++	+++	No	+++	inhibition
4 >1.0 g N/m ² -d (>0.36 g H ₂ /m ² -day)	++++	++++	Yes	++++	strong inhibition

Notes: +: very weak effect; ++: weak effect; +++: strong effect; ++++: very strong effect. The effects are qualitative.

7.3 A Model for NO_3^- and SO_4^{2-} Reductions in the MBfR Biofilm

Tang, Y., A. Ontiveros-Valencia, L. Feng, C. Zhou, R. Krajmalnik-Brown, and B. E. Rittmann (2012a). A biofilm model to understand the onset of sulfate reduction in denitrifying membrane biofilm reactors. *Biotechnol. Bioengr.* 110: 763 – 772.

This work developed a multispecies biofilm model that describes the co-existence of DB and SRB in the H_2 -based MBfR. The model is based upon the same framework as the model for NO_3^- and ClO_4^- reductions (described in the previous two sections), but considers the unique metabolic and physiological characteristics of autotrophic SRB that use H_2 as their electron donor. The framework is illustrated in Figure 34. A critical feature is that the SRB do not reduce NO_3^- , while the DB do not reduce SO_4^{2-} . This differs from the case with PRB, which are able to reduce NO_3^- and ClO_4^- .

To evaluate the model, we simulated effluent H_2 , UAP, and BAP concentrations, along with biomass distributions in the biofilm. We compared all of these results to chemical analyses and qPCR data from the experiments on Ontiveros-Valencia et al. (2012) (reported above). Figure 35 shows that model outputs and experimental results match for all major trends and explain when SO_4^{2-} reduction does or does not occur in parallel with denitrification. Figure 35b indicates that SO_4^{2-} reduction is suppressed when all of the H_2 is consumed inside the biofilm (Fig. 34). In accordance with the experimental results of Ontiveros-Valencia et al. (2012), SO_4^{2-} reduction could be suppressed with a NO_3^- surface loading that is $0.4 \text{ g H}_2/\text{m}^2\text{-day}$ when H_2 delivery is limiting. Mechanistically, the model tells us that the onset of SO_4^{2-} reduction occurs only when the NO_3^- concentration at the fiber's outer surface is low enough so that the growth rate of the denitrifying bacteria is equal to that of the SRB. The model also predicts that effluent UAP and BAP increase noticeably when SO_4^{2-} reduction begins (Fig. 36). The increase of UAP and BAP translates into a rise of the DOC concentration, a factor observed in the field pilot study, when SO_4^{2-} reduction was significant (Evans et al., 2013).

An example shows how to use the model to design an MBfR that achieves satisfactory NO_3^- reduction, but suppresses SO_4^{2-} reduction. In Figure 37, good NO_3^- reduction is possible without SO_4^{2-} reduction when the flow rate is around $10 \text{ m}^3/\text{day}$, which corresponds to NO_3^- surface loadings of approximately $0.94 \text{ g N}/\text{m}^2\text{-day}$ or $0.33 \text{ g H}_2/\text{m}^2\text{-day}$. The effluent NO_3^- concentration increases for higher flow rates and NO_3^- surface loadings, reaching the 10-mg N/L MCL at around $1.5 \text{ g N}/\text{m}^2\text{-day}$ (NO_3^- surface flux of about $0.5 \text{ g H}_2/\text{m}^2\text{-day}$).

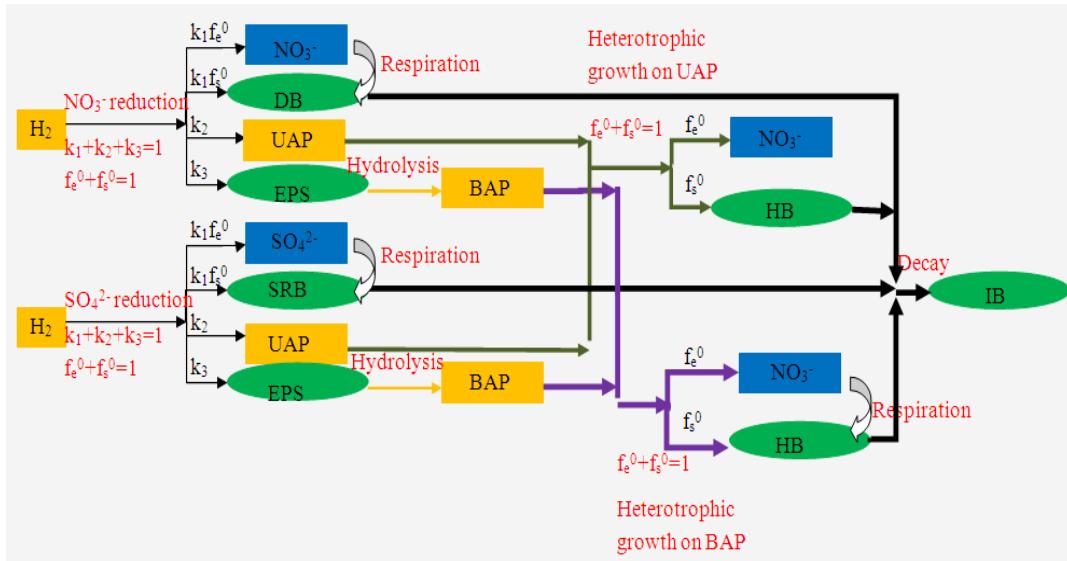
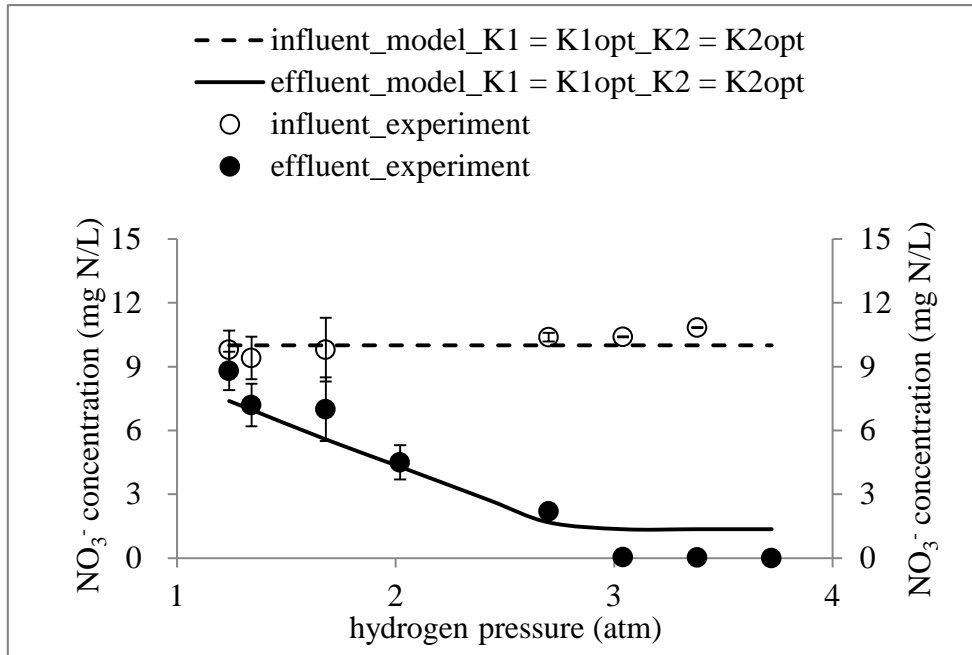
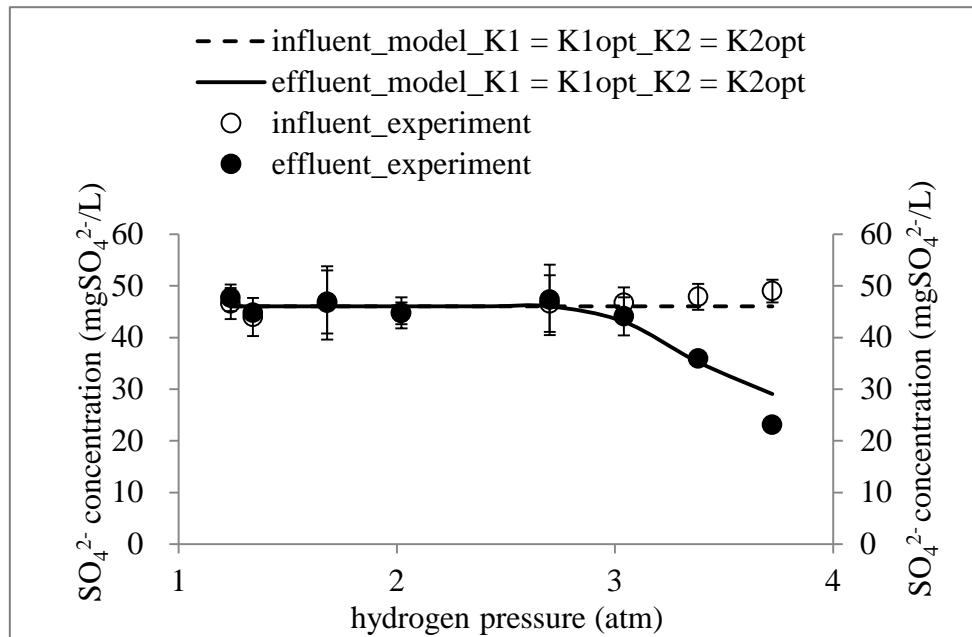


Figure 34. Schematic describing how the dissolved components (rectangles) and solid components (ellipses) interact for the biofilm model with NO_3^- and SO_4^{2-} reductions.



a.



b.

Figure 35. Comparison of effluent NO_3^- and SO_4^{2-} concentrations from the experiment (symbols) and from the model (lines) with optimized parameters ($K_1 = 0.2$ mg N/L and K_2 equals 1.6 mg SO_4^{2-} /L).

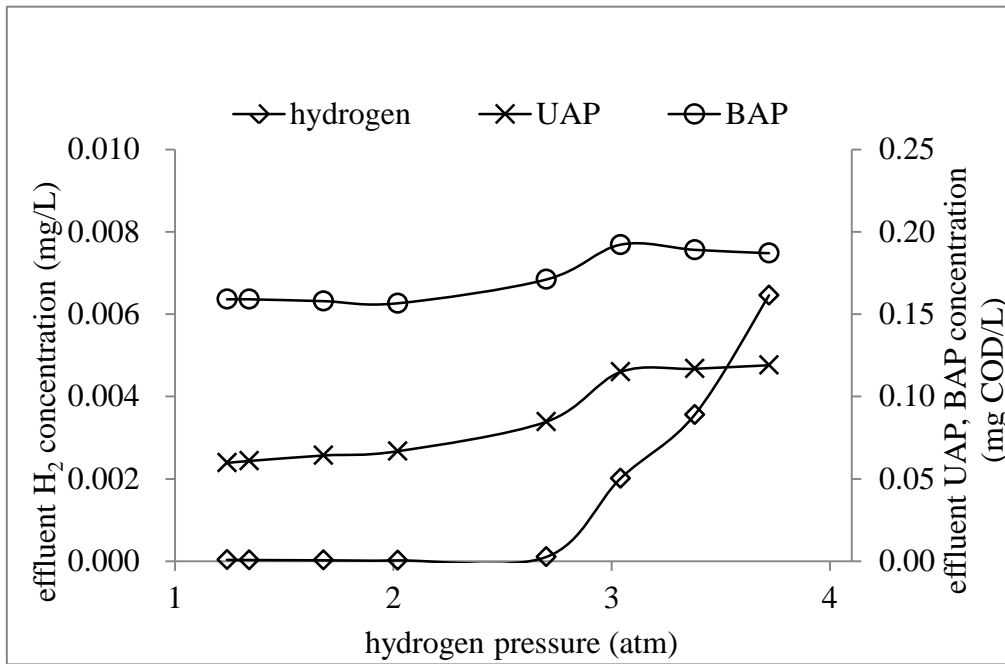


Figure 36. Model-simulated concentrations of H₂, UAP, and BAP in the effluent.

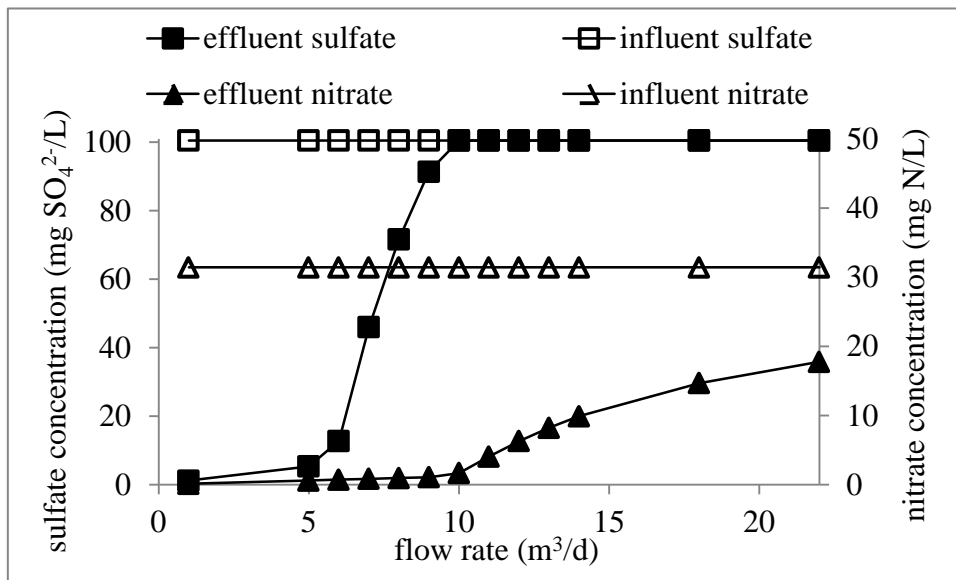


Figure 37. Model-simulated effluent NO₃⁻ and SO₄²⁻ concentrations at flow rates of 1 to 22 m³/d in a module having 320 m² of fiber surface area.

Chapter 8. Special Modeling Evaluation of the Pilot MBfRs

We applied the $\text{NO}_3^- + \text{ClO}_4^-$ model of Tang et al. (2012c,d) (reviewed previously) to the conditions of the Rialto pilot MBfRs. Here, we summarize the main modeling results in ways that help explain why pilot-MBfR performance changed with different conditions. In particular, we investigate why the ClO_4^- concentration could not be reduced consistently to below $6 \mu\text{g/L}$ in the pilot-scale MBfR.

Figures 38 and 39 plot simulated effluent NO_3^- , ClO_4^- , and H_2 concentrations relevant to the pilot-scale lead and lag MBfRs, respectively. Operating conditions are identified in the figure captions. The simulated operating conditions cover the range used in the pilot test. Extreme operating conditions are not simulated, as they are not relevant in practice or to the pilot experiments.

Important features to see while comparing the modeling results for the lead MBfR (Figure 38) to experimental results are:

- 1) The ClO_4^- panel can be divided into three areas:
 - a) Blue area, in which, the effluent ClO_4^- is stable at $\sim 50 \mu\text{g/L}$. For the simulated conditions, the lead MBfR never takes the ClO_4^- concentration below about $50 \mu\text{g/L}$, because the half-maximum-rate concentration for perchlorate is $780 \mu\text{g/L}$ in the model simulation, and this gives an S_{\min} value of $56 \mu\text{g/L}$. Since the flow rate is used to control the NO_3^- and ClO_4^- surface loadings, they are proportional to each other. We see that stable low ClO_4^- concentration begins when the effluent NO_3^- concentration is less than $\sim 1 \text{ mg N/L}$ and when the H_2 concentration is more than $\sim 500 \mu\text{g/L}$. Smaller NO_3^- and larger H_2 concentrations (due to lower flow rates) do not enhance ClO_4^- removal further. The border for entering the blue region is a NO_3^- surface loading of 0.5 to $0.7 \text{ g N/m}^2\text{-day}$ (0.18 to $0.25 \text{ g H}_2/\text{m}^2\text{-day}$), depending on the H_2 pressure.
 - b) Yellow area, in which the effluent perchlorate is very sensitive to H_2 pressure and flow rate. If a reactor is operated at this area, effluent ClO_4^- can change significantly for small changes in flow rate or NO_3^- loading.
 - c) Red area, in which ClO_4^- reduction does not occur due to competition from NO_3^- reduction. We expect no ClO_4^- removal for NO_3^- surface loading above 0.65 to $0.9 \text{ g N/m}^2\text{-day}$ (0.24 to $0.32 \text{ g H}_2/\text{m}^2\text{-day}$), depending on the H_2 pressure.
- 2) The pilot-scale lead MBfR was operated in either the blue area or the yellow area, depending on the hydrogen pressure and flow rate.
- 3) The effluent H_2 pressure represents the potential for SO_4^{2-} reduction. Seeing non-trivial H_2 signifies that SO_4^{2-} reduction is likely, because H_2 remains in the biofilm and can allow SRB growth and accumulation near the substratum. In particular, the green, yellow, and red areas to the upper left of the H_2 panel show where SO_4^{2-} reduction is likely in the lead MBfR; this is where the effluent ClO_4^- concentration is about $50 \mu\text{g/L}$.

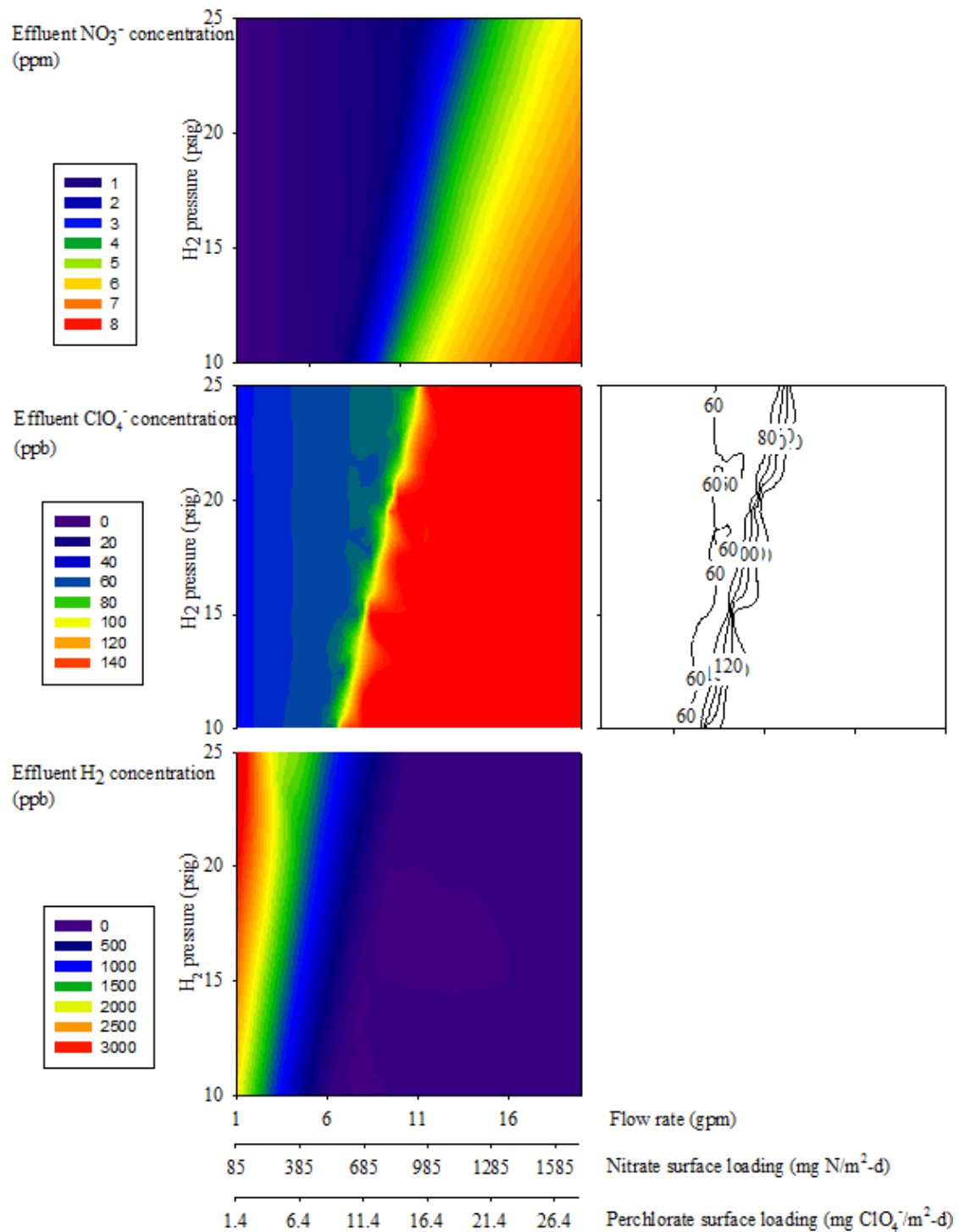


Figure 38. Simulated effluent NO₃⁻ (top), ClO₄⁻ (middle left and right), and H₂ (bottom) concentrations for the pilot-scale lead MBfR. The operating conditions are: fiber surface area = 576 m², influent DO = 8 mg/L, influent nitrate = 9 mg N/L, influent perchlorate = 150 μg/L, H₂ pressures = 10-25 psig, and flow rates = 1-20 gpm.

Figure 39 summarizes the model-simulated performance of a lag MBfR. The input conditions, noted in the caption, are typical of what is in the effluent of a lead MBfR and are consistent with the right edge of the blue area in the ClO_4^- plot of Figure 36. Figure 39 says that the lag MBfR ought to be able to achieve an effluent ClO_4^- concentration well below $6 \mu\text{g/L}$ for the range of conditions evaluated, since competition with DB is much lower than for the lead MBfR. Also, the relatively low NO_3^- concentration fed to the lag reactor promotes the growth of PRB, which help reduce ClO_4^- to an even lower level (Tang et al., 2012c,d). Since the flow rate is used to control the loadings of ClO_4^- and NO_3^- , the loadings and effluent concentrations of both electron acceptors vary together with flow rate. The NO_3^- concentration remains less than 0.4 mg N/L for all flow rates, which give a NO_3^- surface loading of 0.1 to $2 \text{ g N/m}^2\text{-day}$, or up to $0.7 \text{ g H}_2/\text{m}^2\text{-day}$. The effluent ClO_4^- concentration increases from $\leq 2 \mu\text{g/L}$ to about $6 \mu\text{g/L}$ as the ClO_4^- loading increased from 0.5 to $7.5 \text{ mg ClO}_4^-/\text{m}^2\text{-day}$. Thus, the lag MBfR seems capable of producing an effluent concentration less than $6 \mu\text{g/L}$ if sulfate reduction is minimized. This is consistent with the bench-scale results of Zhao et al. (2013a), reviewed earlier in the report.

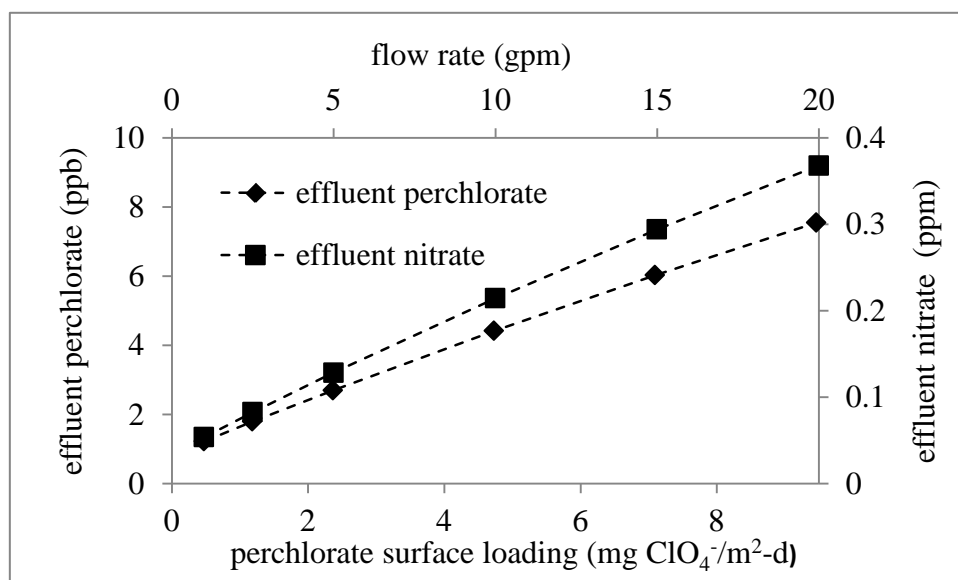


Figure 39. Simulated effluent NO_3^- and ClO_4^- concentrations for the pilot-scale lag MBfR. The operating conditions are: fiber surface area = 576 m^2 , influent $\text{DO} = 0 \text{ mg/L}$, influent nitrate = 2 mg N/L , influent perchlorate = $50 \mu\text{g/L}$, H_2 pressures = 15 psig , and flow rates = $1\text{-}20 \text{ gpm}$. Since H_2 pressure was always not limiting in the lag reactor, only one H_2 pressure is modeled. The effluent H_2 concentration was $> 80 \mu\text{g/L}$.

Because the pilot results did not achieve ClO_4^- concentrations less than $6 \mu\text{g/L}$, we used the model to simulate the effluent ClO_4^- concentrations for scenarios that correspond to one or more of the following possible causes of poorer ClO_4^- removal in the lag MBfR compared to model-simulated expectations:

- 1) No O_2 was available in the lag MBfR's influent. Dissolved O_2 is an electron acceptor for PRB, and its reduction can increase the PRB biomass.
- 2) The PRB in the pilot MBfRs have a higher half-maximum-rate concentration (K) for ClO_4^- than used in the model, which was able to simulate bench-scale results well. A higher K value slows the kinetics for ClO_4^- reduction, particularly for the desired low concentrations.
- 3) The mass-transport resistance of ClO_4^- to the biofilm is increased due to the spacers and inert biomass building up in and on the spacers. This effect is simulated by increasing the thickness of the liquid diffusion layer (L).

These conditions are outlined in Table 5, which also summarizes the results. On the one hand, scenario 1 (adding O_2 to the lag-MBfR influent) brings about a significant increase in the biofilm mass, but this results in only a small increase in ClO_4^- removal. On the other hand, scenarios 2 (higher K for ClO_4^- , probably due to different microbial populations), 3 (thicker L due to spacers or the flow path), and the combination of 2 and 3 show significant negative impacts on the effluent ClO_4^- concentration. Taken alone, scenario 2 or 3 increases the simulated ClO_4^- concentration from 2.7 $\mu\text{g/L}$ to 7.0 or 7.5 $\mu\text{g/L}$, respectively. Together, they lead to an effluent concentration of 11.4 $\mu\text{g/L}$.

The results in Table 5 suggest that physical details of the pilot MBfRs may have led to accumulation of biomass that increased mass-transport resistance and also may have selected for somewhat less-efficient PRB. When coupled with the field data, the modeling analysis suggests that improvements to the internal configuration of the MBfR may be the most efficient strategy for improving performance when the goal is to achieve a very low effluent concentration. In particular, experiments varying the recirculation ratio in the field pilot showed that the reduction kinetics for all acceptors were sensitive to the recirculation rate (Evans et al., 2013). This is consistent with the findings in Table 5 that external mass-transport resistance could have been a key factor for why the ClO_4^- concentration could not be driven below 6 $\mu\text{g/L}$. Likewise, the pilot MBfRs were operated with excess H_2 delivery capacity and had significant SO_4^{2-} reduction, which slows ClO_4^- reduction kinetics, as shown in bench scale research by Ontiveros-Valencia et al., (2013b).

Table 5. Simulated scenarios to investigate the difference in perchlorate removal in a typical lag MBfR

Simulated scenarios	Parameters change	Simulated effluent perchlorate ($\mu\text{g/L}$)	Simulated effluent nitrate (mg/L)	Simulated effluent hydrogen (mg/L)	Simulated biofilm thickness (μm)
Standard condition^a	none	2.7	0.13	2.06	13.5
1. Oxygen addition (S)	S increases from 0 to 8 mg/L	2.2	0.26	1.71	24.3
2. Higher half-maximum-rate concentration (K)	K increases from 0.8 to 4.0 mg/L	7.0	0.13	2.06	13.5
3. Thicker diffusion layer (L)	L (liquid diffusion layer) increases from 100 to 500 μm	7.5	0.37	2.03	12.4
4. Combined scenarios 2 and 3	K increases from 0.8 to 4.0 mg/L; L increases from 100 to 500 μm	11.4	0.37	2.03	12.3

a. The standard condition in the lag reactor of the pilot-scale MBfR: fiber surface area = 576 m^2 , influent DO = 0 mg/L, influent nitrate = 2 mg N/L, influent perchlorate = 50 $\mu\text{g/L}$, H_2 pressures = 15 psig, flow rates = 5 gpm.

Chapter 9. Global Synthesis

The field pilot study at Rialto, CA showed that, although the two-stage MBfR system was effective for reducing NO_3^- and ClO_4^- , it did not achieve one of the goals: an effluent ClO_4^- concentration less than $6 \mu\text{g/L}$. Attempts to reduce the loading rates of the electron acceptors by lowering the flow rate did not lead to the desired outcome of $\text{ClO}_4^- < 6 \mu\text{g/L}$ for sustained operation, but led to SO_4^{2-} reduction, an undesired outcome. Likewise, regularly switching the lead and lag positions did not bring about the desired result.

The ASU Team carried out a wide range of studies to uncover why the two-stage MBfR system did not achieve the $6\text{-}\mu\text{g/L}$ goal, even though it performed well in other ways. The team carried out extensive analyses of the acceptor and donor (H_2) fluxes during the pilot study and correlated them to a range of analyses of biofilm samples sent to ASU from Rialto. In parallel, the ASU team carried out bench-scale MBfR experiments and developed mechanistic mathematical models to identify and quantify the kinetic and ecological mechanisms underpinning the performance of the pilot and bench-scale MBfRs. The preceding sections of this report summarize all of those results.

This section synthesizes all of the results to provide a comprehensive understanding of what controlled the performance of the pilot MBfRs and what changes hold promise for improving MBfR performance when the goal is achieving a very low ClO_4^- concentration when a range of other electron acceptors is present.

The biofilms in the reactor modules in the MBfR vessels and side-reactors had consistent characteristics that reflect the operating conditions at the pilot site. While the biofilm thickness varied in the pilot MBfRs, it typically was about $200 \mu\text{m}$. The biofilm was only about 10% inorganic, which means that precipitation was prevented well by the pH-control system. While the biofilm contained around 40 – 50% EPS, the cells were predominantly live, particularly near the membrane substratum. For all MBfRs, PRB always made up the smallest fraction of the active bacteria, SRB always were present, and SRB became more important when SO_4^{2-} reduction was the a major sink for H_2 . In the bench-scale studies done at ASU, *Dechloromonas* was an important DB and PRB when ClO_4^- reduction was successful, but it was not always the main PRB.

Pilot, bench-scale, and modeling results were consistent about the need to manage the fluxes of NO_3^- , O_2 , and SO_4^{2-} to allow for complete ClO_4^- reduction. In order to compare all fluxes, we express all of them in terms of their H_2 consumption flux, or in $\text{g H}_2/\text{m}^2\text{-day}$.

1. According to modeling results and bench-scale experiments, a moderate flux of $\text{NO}_3^- + \text{O}_2$ is one key to helping promote PRB and ClO_4^- reduction by giving the PRB three electron acceptors (ClO_4^- , NO_3^- , and O_2) without causing too much competition for H_2 and space.
 - a. Modeling says that a $\text{NO}_3^- + \text{O}_2$ flux of 0.036 to $0.21 \text{ g H}_2/\text{m}^2\text{-day}$ promotes ClO_4^- reduction, while a flux $\geq 0.36 \text{ g H}_2/\text{m}^2\text{-day}$ begins to cause serious inhibition to ClO_4^- reduction.
 - b. With synthetic medium in a bench-scale MBfR, full ClO_4^- was possible at a $\text{NO}_3^- + \text{O}_2$ flux up to $0.33 \text{ g H}_2/\text{m}^2\text{-day}$ when the SO_4^{2-} flux was as high as $0.25 \text{ g H}_2/\text{m}^2\text{-day}$. It is possible the S cycling between SO_4^{2-} and S^0 played a role in enhancing ClO_4^- reduction despite significant SO_4^{2-} reduction by lowering the H_2 demand for SO_4^{2-} reduction.

- c. When using Rialto groundwater at the bench scale, a $\text{NO}_3^- + \text{O}_2$ flux $\leq 0.18 \text{ g H}_2/\text{m}^2\text{-day}$ in a lag MBfR (with polypropylene fibers) allowed full ClO_4^- reduction. A $\text{NO}_3^- + \text{O}_2$ flux $\geq 0.21 \text{ g H}_2/\text{m}^2\text{-day}$ allowed partial ($\sim 30\%$) ClO_4^- reduction in the same Rialto groundwater in the lead MBfR.
 - d. For comparison, the pilot MBfRs gave the highest ClO_4^- flux in the lag MBfR when the $\text{NO}_3^- + \text{O}_2$ flux was $\sim 0.17 \text{ g H}_2/\text{m}^2\text{-day}$, which is in the range that modeling and bench-scale studies suggest should give good ClO_4^- reduction.
2. Modeling and bench-scale results consistently point to keeping the $\text{NO}_3^- + \text{O}_2$ flux in a moderate range to suppress SO_4^{2-} reduction.
 - a. A flux of $0.2 - 0.4 \text{ g H}_2/\text{m}^2\text{-day}$ from $\text{NO}_3^- + \text{O}_2$ definitely prevented SO_4^{2-} reduction, with a typical target flux of $\sim 0.3 \text{ g H}_2/\text{m}^2\text{-day}$.
 - b. In a two-stage MBfR with polypropylene fibers and fed Rialto groundwater, a $\text{NO}_3^- + \text{O}_2$ flux of $0.18 \text{ g H}_2/\text{m}^2\text{-day}$ could stop SO_4^{2-} reduction, even though SRB were present.
 - c. For comparison, a $\text{NO}_3^- + \text{O}_2$ fluxes $\geq 0.1 \text{ g H}_2/\text{m}^2\text{-day}$ slowed SO_4^{2-} reduction in the pilot lag MBfR, while $> 0.3 \text{ g H}_2/\text{m}^2\text{-day}$ stopped SO_4^{2-} reduction in the pilot lead MBfR.
 3. Bench-scale results suggest that SO_4^{2-} reduction by itself did not necessarily slow ClO_4^- reduction, although the pilot results gave the best ClO_4^- flux with the smallest SO_4^{2-} flux, which was associated with a $\text{NO}_3^- + \text{O}_2$ flux of $\geq 0.17 \text{ g H}_2/\text{m}^2\text{-day}$. Whether or not SO_4^{2-} reduction slows ClO_4^- reduction, it should be suppressed to avoid other water-quality problems, as were observed in the pilot MBfRs (Evans et al., 2013).

Factors relating to the operation of the pilot MBfRs may have affected performance for ClO_4^- reduction. Special modeling runs for the pilot conditions suggested that external mass-transport resistance may have been greater in the pilot MBfRs than in the bench-scale MBfRs. This interpretation may be supported by our observation that a large amount of biomass accumulated between the spacers. The special modeling runs also point to the possibility that the pilot biofilms selected for different and less-efficient PRB.

Another difference between operation of the pilot two-stage MBfRs and the bench-scale two-stage MBfRs is that the lead and lag positions for the pilots were switched regularly, while they were not switched for the bench-scale MBfRs. Consistent with these operating differences is that the biofilm communities were similar between lead and lag MBfR for the pilot, but distinctly different for the bench-scale MBfRs.

Another difference is that the influent of the lag MBfRs was oxygenated in the bench-scale experiments. Oxygenation made it possible to control the $\text{NO}_3^- + \text{O}_2$ surface loading to the lag MBfR, keeping it in the optimal range even though most of the NO_3^- was removed in the lead MBfR. This seems like a good option to build into MBfR systems designed for reducing ClO_4^- and NO_3^- .

One more difference is that the lead and lag MBfRs were switched regularly in the field pilot, while they were maintained as lead or lag for the bench-scale studies and special modeling analysis. The switching definitely caused the biofilm communities to be similar between lead and lag MBfRs. It also may have played a role in accentuating accumulation of SRB by making the biofilm thicker in the lag MBfR.

In summary, the modeling and bench-scale results show no intrinsic roadblock for achieving a very low ClO_4^- concentration when the influent water contains much higher

concentrations of NO_3^- , O_2 , and SO_4^{2-} . One clear key is managing the $\text{NO}_3^- + \text{O}_2$ loading so that it promotes PRB while simultaneously suppressing SO_4^{2-} reduction. The two-stage strategy is well tuned for this goal, and particular attention has to be paid to the $\text{NO}_3^- + \text{O}_2$ loading to the lag MBfR. While the results do not give an exact target value, they suggest that the lag MBfR should have a $\text{NO}_3^- + \text{O}_2$ flux of around $0.18 \text{ g H}_2/\text{m}^2\text{-day}$ to meet the ClO_4^- and SO_4^{2-} goals together.

Besides $\text{NO}_3^- + \text{O}_2$ surface loadings, liquid velocities past the membranes and their corresponding mass-transfer resistances and biofilm-detachment rates probably were different between the bench-scale and pilot-scale setups. Larger external mass-transport resistance in the pilot MBfR could have slowed ClO_4^- removal in the pilot setup (Evans et al., 2013). Less biofilm detachment in the pilot-scale MBfRs may have led to more accumulation of SRB. The impact of detachment is worth mentioning, because other operational conditions that promoted SRB activity (e.g., lower total-acceptor loading and delivery of excess H_2) allowed SRB to outnumber the normally faster-growing DB and PRB (Ontiveros-Valencia et al., 2013b).

Chapter 10. References

- Box, J. D. Investigation on the Folin-Ciocalteu phenol reagent for determination of polyphenolic substances in natural waters. *Water Research* **1983**, *17*, 511-525.
- Blondeau, R. Evolution des acides humiques soumis A l'activite d'une microflore bacterienne heterotrophe. *Sci. Sol.* **1988**, *26*, 17-26.
- Cescutti, P.; Toffanin, R.; Pollesello, P.; Sutherland, I.W. Structural determination of the acidic exopolysaccharide produced by a *Pseudomonas* sp. strain 1.15. *Carbohydrate Res.* **1999**, *315* (1/2), 159-168.
- Coates, J. D.; Chakraborty, R.; Lack, J. G.; O'Connor, S. M.; Cole, K. A.; Bender, K. S.; Achenbach, L. A. Anaerobic benzene oxidation coupled to nitrate reduction in pure culture by two strains of *Dechloromonas*. *Nature* **2001**, *411*, 1039-1043.
- Dubois, M.; Gilies, K.; Hammilton, K. J.; Robers, A. P.; Smith, A. F. A colorimetric method for the determination of sugars related substances. *Analytical Chemistry* **1951**, *28*, 350-356.
- Ellis, B. D.; Butterfield, P.; Jones, W. L.; McFeters, G. A.; Camper, A. K. Effects of Carbon Source, Carbon Concentration, and Chlorination on Growth Related Parameters of Heterotrophic Biofilm Bacteria. *Microbial Ecology* **2000**, *38*, 330-347.
- Evans, P.; Smith, J.; Singh, T.; Hyung, H.; Arucan, C.; Berokoff, D.; Friese, D.; Overstreet, R.; Vigo, R.; Rittmann, B. E.; Ontiveros-Valencia, A.; Zhao, H. P.; Tang, Y.; Kim, B. O.; Van Ginkel, S.; Krajmalnik-Brown, R. Nitrate and Perchlorate Destruction and Potable Water Production Using Membrane Biofilm Reduction. ESTCP Project ER-200541, **2013**.
- Frølund, B.; Palmgren, R.; Keiding, K.; Nielsen, P.H. Extraction of extracellular polymers from activated sludge using a cation exchange resin. *Water Res.* **1996**, *30*, 1749-1758.
- Kaplanbach, J. A.; Saxman, P. R.; Cole, J. R.; Schmidt, T. M. rrndb: The ribosomal RNA operon copy number database. *Nucleic Acids Res.* **2001**, *29*, 181-184.
- Kondo, R.; Nedwell, D. B.; Purdy, K. J.; Quiroz Silva, S. Detection and enumeration of sulphate-reducing bacteria in estuarine sediments by competitive PCR. *J. Geomicrobiology* **2004**, *21*, 145-157.
- Lee, Z. M.-P.; Bussema III, C.; Schmidt, T. M. rrnDB: documenting the number of rRNA and tRNA genes in bacteria and archaea. *Nucleic Acids Res.* **2008**, *37*, D489-D493.
- Liu, H. & Fang, H. F. Extraction of extracellular polymeric substances (EPS) of Sludges. *J. Biotechnol.* **2002**, 249-256.

Masahiro, A.; Ryoichi, H.; Fumihiko, J.; Kenichi, S. The treatment of the humic substance from a domestic wastewater treatment device effluent. Proceedings of Taal 2007: The 12th World Lake Conference, **2008**, pp 941-943.

Muyzer, G.; Stams, A. J. M. The ecology and biotechnology of sulphate-reducing bacteria. *Nat. Rev. Microbiol.* **2008**, *6*, 441-454

Ontiveros-Valencia, A.; Ziv-El, M.; Zhao, H.; Feng, L.; Rittmann, B. E.; Krajmalnik-Brown, R.. Interactions between nitrate-reducing and sulfate-reducing bacteria in a hydrogen-fed biofilm. *Environ. Sci. Technol.* **2012**, *46*: 11289-11298

Ontiveros-Valencia, A.; Ilhan, Z. E.; Kang, D. W.; Rittmann, B. E.; Krajmalnik-Brown, R. Phylogenetic analysis of nitrate- and sulfate-reducing bacteria in a hydrogen-fed biofilm *FEMS Microbial Ecology*, **2013a**, *85*: 158-167.

Ontiveros-Valencia, A.; Tang, Y.; Krajmalnik-Brown, R.; Rittmann, B. E. Perchlorate reduction from a highly contaminated groundwater in the presence of sulfate-reducing bacteria in a hydrogen-fed biofilm. *Biotechnol. Bioeng.*, **2013b**, DOI: 10.1002/bit.24987.

Philippot, L.; Hallin, S.; Schloter, M. Ecology of denitrifying prokaryotes in agricultural soils. *Adv. Agron.* **2007**, *96*, 249-305.

Rittmann, B. E. The membrane biofilm reactor is a versatile platform for water and wastewater treatment'. *Environ. Eng. Res.* **2007**, *12*, 157-175.

Rittmann, B. E. & McCarty, P. L. Environmental Biotechnology: Principles and Applications. New York: McGraw-Hill. **2001**

Sutherland, I.W.; Kennedy, L. Polysaccharide lyases from gellan-producing *Sphingomonas* spp. *Microbiol.* **1996**, *142*, 867-872.

Tang, Y.; Ontiveros-Valencia, A.; Feng, L.; Zhou, C.; Krajmalnik-Brown, R.; Rittmann, B. E. A biofilm model to understand the onset of sulfate reduction in denitrifying membrane biofilm reactors. *Biotechnol. Bioengr.* **2012a**, *100*: 763-772.

Tang, Y.; Zhou, C.; Van Ginkel, S.; Ontiveros, A.; Shin, J.; Rittmann, B. E. Hydrogen-Permeation Coefficients of the Fibers Used in H₂-Based Membrane Biofilm Reactors. *J Membrane Sci.* **2012b**, *407-408*:176-183

Tang, Y.; Zhao, H. P.; Marcus, A. K.; Krajmalnik-Brown, R.; Rittmann, B. E. A steady-state biofilm model for simultaneous reduction of nitrate and perchlorate -- Part 1: model development and numerical solution. *Environ. Sci. Technol.* **2012c**, *46*: 1598 – 1607.

Tang, Y.; Zhao, H. P.; Marcus, A. K.; Krajmalnik-Brown, R.; Rittmann, B. E. A steady-state-biofilm model for simultaneous reduction of nitrate and perchlorate –Part 2: Parameter optimization and results and discussion. *Environ. Sci. Technol.* 2012d, 46, 1608-1615.

Thermo Fisher Scientific Inc. BCA Protein assay reagent (bicinchroninic acid). 2011, Retrieved On October 18, 2012, from PIERCENET:
<http://www.piercenet.com/browse.cfm?fldID=02020101>

Veiga, M.C.; Mahendra, K.J.; Wu, W.M.; Hollingsworth, R.I.; Zeikus, J.G. Composition and role of extracellular polymers in methanogenic granules. *Appl. Environ. Microbiol.* 1997, 63, 403–407

Zhao, H.; Van Ginkel, S.; Tang, Y.; Kang, D.-W.; Rittmann, B. E.; Krajmalnik-Brown, R. Interactions between perchlorate and nitrate reductions in the biofilm of a hydrogen-based membrane biofilm reactor. *Environ. Sci. Technol.* 2011, 45, 10155-10162.

Zhao, H.; Ontiveros-Valencia, A.; Tang, Y.; Kim, B.; Krajmalnik-Brown, R.; Rittmann, B. E. Using a two-stage hydrogen-based membrane biofilm reactor (MBfR) to achieve complete perchlorate reduction in the presence of nitrate and sulfate. *Environ. Sci. Technol.* 2013a, 47, 1565-1572.

Zhao, H.; Ilhan, Z. E., Ontiveros-Valencia, A.; Tang, Y., Rittmann, B. E.; Krajmalnik-Brown, R. Interactions among multiple electron acceptors and their effects on the microbial ecology in a hydrogen-based biofilm. *Environ. Sci. Technol.* 2013b, 47: 7396-4703.